

Micro-particle Streak Velocimetry - Theory, Simulation Methods and Applications

by

Prasun Mahanti

A Dissertation Presented in Partial Fulfillment
of the Requirements for the Degree
Doctor of Philosophy

Approved October 2011 by the
Graduate Supervisory Committee:

Thomas Taylor, Co-Chair
Douglas Cochran, Co-Chair
Mark Hayes
Junshan Zhang

ARIZONA STATE UNIVERSITY

December 2011

© 2011 Prasun Mahanti

All Rights Reserved

ABSTRACT

This dissertation describes a novel, low cost strategy of using particle streak (track) images for accurate micro-channel velocity field mapping. It is shown that 2-dimensional, 2-component fields can be efficiently obtained using the spatial variation of particle track lengths in micro-channels.

The velocity field is a critical performance feature of many microfluidic devices. Since it is often the case that un-modeled micro-scale physics frustrates principled design methodologies, particle based velocity field estimation is an essential design and validation tool. Current technologies that achieve this goal use particle constellation correlation strategies and rely heavily on costly, high-speed imaging hardware. The proposed image/video processing based method achieves comparable accuracy for fraction of the cost.

In the context of micro-channel velocimetry, the usability of particle streaks has been poorly studied so far. Their use has remained restricted mostly to bulk flow measurements and occasional ad-hoc uses in microfluidics. A second look at the usability of particle streak lengths in this work reveals that they can be efficiently used, after approximately 15 years from their first use for micro-channel velocimetry.

Particle tracks in steady, smooth microfluidic flows is mathematically modeled and a framework for using experimentally observed particle track lengths for local velocity field estimation is introduced here, followed by algorithm implementation and quantitative verification. Further, experimental considerations and image processing techniques that can facilitate the proposed methods are also discussed in this dissertation.

Unavailability of benchmarked particle track image data motivated the implementation of a simulation framework with the capability to generate exposure time controlled particle track image sequence for velocity vector fields. This dissertation also describes this work and shows that arbitrary velocity fields designed in computational fluid dynamics software tools can be used to obtain such images. Apart from aiding gold-standard data generation, such images would find use for quick microfluidic flow field visualization and help improve device designs.

Dedicated to my parents

ACKNOWLEDGEMENTS

As I look back at the years spent as a graduate student at Arizona State University, I find myself grateful for all that I have received over these years. I feel privileged to have had the opportunity to work with so many knowledgeable and inspiring individuals. Their guidance and presence at various junctures of my graduate life has certainly shaped me as a person and as a scholar.

My first, and most earnest, acknowledgement goes to my advisors Dr. Thomas Taylor and Dr. Douglas Cochran. I would like to thank Dr. Taylor for being there whenever I needed to discuss my half-baked ideas, for always being supportive, encouraging and for helping me see life and science together. I thank him for leading me into rethinking my ideas without being the least critical – I learned so much from these. I thank Dr. Cochran for being so inspiring and thoughtful. Discussion on and off subject with him were always useful, well directed and often had a touch of humor that made conversations so much more enjoyable. I have often been surprised and grateful by his ability to quickly understand problems I was facing and his eagerness to suggest solutions. I would like to thank both my advisors for encouraging me to trust my intuitions and for inspiring me to be passionate about the pursuit of scientific research.

I was fortunate to have had the opportunity to work with Dr. Mark A. Hayes during my Ph.D. years. His suggestions during our discussions helped me realize practical merits and concerns about the algorithms and methods I was pursuing. I would like to thank him for his support, guidance and for giving me the opportunity to work in his laboratory and conduct data acquisition experiments.

I am grateful for the support I received from Dr. Mark S. Robinson and Dr. Svetlana Roudenko, during my graduate studies. Specifically, I thank Dr. Robinson for giving me the opportunity to work with him as a student and for entrusting me with vital live projects at LROC, ASU. I am thankful to Dr. Roudenko for her guidance and for giving me the opportunity to work with the Department of Mathematics.

I would also like to thank Dr. Steven Neuberg for his support, Dr. Junshan Zhang for offering valuable suggestions to my dissertation as a my Ph.D. committee member, my

cohorts and friends at GWC and Hayes lab for the wonderful memories and to the entire staff at the departments of Electrical Engineering, Mathematics & Statistics, Chemistry & Bio-chemistry and School of Earth and Space Exploration at Arizona State University for being ever so helpful with my paperwork and queries.

Lastly, I would like to thank all my family for all their love, encouragement and sacrifice throughout my life. To my father who nurtured my love of science and encouraged me in all my pursuits without sparing any expenses nor time, to my mother without whose love and sacrifice I would not be what I am today, to my brother who has always been there for me and to my loving, encouraging, and patient wife Runali, whose faithful support during the final stages of this Ph.D. kept me going, Thank you.

TABLE OF CONTENTS

	Page
LIST OF FIGURES	x
CHAPTER	
1 INTRODUCTION	1
2 BACKGROUND	6
2.1 Micro particle image velocimetry and particle tracking velocimetry	6
2.2 Particle streak velocimetry	13
2.3 The proposed μPSV methods	15
3 PARTICLE VELOCITY VECTOR FIELDS, SAMPLING AND ESTIMATION	20
3.1 Eulerian and Lagrangian velocity representations	20
3.1.1 The Lagrangian representation	20
3.1.2 The Eulerian representation and device physics	22
3.1.3 Interconversion between representations	22
3.2 Velocity vector fields	23
3.2.1 Characteristic curves of vector fields	23
3.2.2 Particle track lengths as line-integral sensor outputs	27
3.2.3 Velocity estimation from length samples – the inverse problem	27
3.3 First-order approximation of vector fields	28
3.3.1 Smooth velocity fields in microfluidics	28
3.3.2 First-order approximation	29
3.3.3 Standard results for particle-tracks from first-order approximation	30
3.3.4 Theoretical point-assignment of average velocity for particle-tracks	33
3.3.5 Rule-of-thumb for quick assignment of average velocity	36
3.4 Streak-length distributions and affine transformations	37
3.4.1 Particle position on streamlines as affine transformations	38
3.4.2 Streak-lengths as an affine transformation of random starting points	41
3.4.3 Streak-lengths for uniformly distributed starting points	41
3.5 Spatio-temporal averaging of streak lengths	42

Chapter	Page
3.6	Estimation of first order approximation parameters 44
3.6.1	Estimation by robust regression 44
3.6.2	Estimation based on maximum and minimum values 45
3.7	On the use of second-order approximated local velocity field 46
3.8	Generation of 2D field components 49
4	EXPERIMENTAL CONSIDERATIONS 51
4.1	Microfluidic device design 52
4.1.1	Channel depth and surface uniformity 52
4.2	Experimental setup 53
4.2.1	Illumination and fluorescence imaging 53
4.2.2	Tracer particle features 53
4.2.3	Seeding density 54
4.2.4	Numerical aperture for the optics 55
4.3	Image acquisition setup 55
4.3.1	Exposure time 55
4.3.2	Frame rate 55
4.4	Number of frames 56
4.5	Distortion effects and mitigation strategies 56
4.5.1	Overlap of particle streak images 56
4.5.2	Defocussing of particle streak images 57
5	IMAGE PROCESSING FOR PARTICLE STREAK FEATURE ESTIMATION . . 58
5.1	Formation of the particle streak image and streak features 58
5.2	Image processing of particle streaks 61
5.2.1	Some basic concepts and methods 61
	Bounding box 61
	Local orientation 61
	Local thresholding 62
	Block matching 62

Chapter	Page
5.2.2	The processing algorithm 62
	Algorithm description 63
	Resolving directional ambiguity 66
5.3	Streak feature database and the local length variation table 66
6	PARTICLE TRACK SIMULATION FOR KNOWN VELOCITY FIELDS 70
6.1	Simulated data for microfluidics experiments – importance and difficulty . 70
6.2	Solution for 1-Dimensional vector field 72
6.2.1	The modified Euler method DE solver 74
6.2.2	Newton-Raphson method of finding roots 75
6.2.3	Geometric solution using cumulative integrals (GSCI) method . . 77
6.3	Extending 1-D solutions to 2-D 81
6.3.1	Pathline sampling of vector fields 82
6.3.2	Pixel connectivity using the Bresenham’s algorithm 83
6.4	The streak simulation framework 83
7	RESULTS AND PERFORMANCE EVALUATION 85
7.1	Studies on the first order approximation 86
7.1.1	Positional error associated with first order Taylor series approxima- tion for 1-D fields 86
7.1.2	Qualitative tracking performance for local liner approximation . . 88
7.1.3	Relative error performance and improvements by sliding window . 90
7.2	Performance of position specific assignment of L/T estimate on streak extent 91
7.3	Performance of the particle streak simulation framework 93
7.3.1	Particle streak simulation for 1-D fields 93
	The modified Euler method 93
	The Newton-Raphson method 95
	The GSCI methods 96
	Comparative computation time performance 97
7.3.2	Particle streak simulation for 2-D fields 99

Chapter	Page
7.4 Performance of spatio-temporal averaging	103
7.4.1 Spatio-temporal averaging for 1-D fields	103
7.4.2 Spatio-temporal averaging for 2-D fields	106
7.5 Performance of velocity estimation by local linear approximation	111
7.5.1 Velocity estimation for 1-D fields	112
Qualitative performance in presence of measurement error	114
Estimation error performance in presence of measurement error	116
7.5.2 Velocity estimation for 2-D fields	121
8 MERITS AND LIMITATIONS OF THE PROPOSED METHODS	129
8.1 Merits of the μPSV method	129
8.1.1 The PTV connection	129
8.1.2 Improvisations over PTV	129
8.1.3 Improvised point estimates	130
8.1.4 Quick 2D2C velocity estimation by spatio-temporal averaging	130
8.1.5 The local linear velocity model	131
8.1.6 Implicit visualization of pathlines	131
8.2 Merits of the particle streak simulation framework	131
8.3 Limitations of the μPSV method	132
8.3.1 Performance dependence on data abundance	132
8.3.2 Selecting the right seeding density	133
8.3.3 Resolving directional ambiguity	133
8.3.4 Smooth, time-invariant velocity field constraints	133
8.4 Limitations of the particle streak simulation framework	134
9 APPLICATIONS	135
9.1 Estimation of known velocity fields	135
9.2 Estimation of centerline velocity field in variable geometry channels	137
9.3 Estimation of 2-D velocity field at a capillary junction	141
10 FUTURE WORK	145

Chapter	Page
10.1 Synthesis of PDMS based channels and performance evaluation	145
10.2 Improvements in estimation strategies	145
10.3 Changes in experimental strategies	146
10.4 Future work for particle flow simulation	146
10.5 Applications of the micro-PSV	146
REFERENCES	147

LIST OF FIGURES

Figure	Page
1.1 Quantitative imaging methods for micro-channel velocimetry	2
2.1 The PIV method: Basic idea	8
2.2 The PTV method: Basic idea	11
2.3 Particle association algorithms	12
3.1 Lagrangian and Eulerian velocity fields	21
3.2 Streamlines	25
3.3 Pathlines	25
3.4 Minimum and maximum lengths for local linear approximation	31
3.5 Boundaries of the length fraction for different tolerances and for positive and negative local gradients	35
3.6 Boundaries of the length fraction for 10% tolerance and for $ aT \leq 10$	37
3.7 β values for different experimentally determined ranges of p for $e_r \leq 0.015$	38
3.8 β values for different values of p for $e_r \leq 0.01$	39
3.9 Variation of particle position along a streamline across a velocity field	40
3.10 Spatio-temporal averaging of streak velocity fields.	43
3.11 Spatio-temporal averaging of streak velocity fields.	50
4.1 Particle image cases: ideal tracer, ideal streak, overlapped streaks and defo- cussed, overlapped streaks	52
4.2 Schematic of an inverted microscope (Olympus IX70)	54
5.1 Static particles, particle streaks and their intensity surface plots	59
5.2 An ideal streak with its bounding box	60
5.3 An experimental setup showing schematic, particle streaks and bounding box	63
5.4 The streak image processing algorithm	64
5.5 Obtaining the position and length stacks	65
5.6 Resolving directional ambiguity	67
5.7 Streak feature database	68
5.8 Obtaining the local length variation table	68

Figure	Page
5.9 Velocity estimate from local length variation table	69
6.1 Particle image generation block diagram	73
6.2 Continuous and discrete relations for the GSCI method	78
6.3 Locating the sign change position of the cumulative integral	80
6.4 Velocity field sampling by particle pathline	82
6.5 The streak image simulation framework	84
7.1 1-D velocity fields used for performance analysis.	86
7.2 First order approximation relative error magnitudes for exponential and hyperbolic velocity fields	87
7.3 Tracking performance of spatio-temporal averaging for exponential velocity field	88
7.4 Tracking performance of spatio-temporal averaging for a hyperbolic velocity field	89
7.5 Relative error for different window widths - exponential and hyperbolic velocity fields	90
7.6 Relative error for different sliding window widths - exponential and hyperbolic velocity fields	91
7.7 Shift in the relative error magnitude with variable local gradient and exposure time at the midpoint and exact assignment positions	92
7.8 Relative error of L/T assignment for variable β and variable rate of change of streak length with respect to the starting position	92
7.9 Computation time and relative error performance for streak length calculation for different velocity fields using the modified Euler method	94
7.10 Computation time and relative error performance for streak length calculation for different velocity fields using the Newton-Raphson method	95
7.11 Computation time and relative error performance for streak length calculation for different velocity fields using the GSCI method	97
7.12 Comparative computational time performance for streak length computation for different velocity fields.	98

Figure	Page
7.13 Particle streak simulation for steady Poiseuille flow	100
7.14 Particle streak simulation for steady flow around a cylindrical obstacle	101
7.15 Particle streak simulation for steady flow at the junction of rectangular channels	102
7.16 Minimum and maximum streak length expressions for different velocity fields .	104
7.17 Tracking performance of spatio-temporal averaging for linear and exponential velocity fields.	105
7.18 Performance of spatial averaging with variation of the aT product.	106
7.19 Tracking performance of spatio-temporal averaging for hyperbolic and sig- moidal velocity field	107
7.20 True vector field and component estimation error for Poiseuille flow	108
7.21 True vector field components and estimated components for Poiseuille flow . .	109
7.22 True vector field and component estimation error for steady flow around a cylin- drical obstacle	110
7.23 True vector field components and estimated components for steady flow around a cylindrical obstacle	111
7.24 True vector field and component estimation error for steady flow at the junction of two rectangular channels	112
7.25 True vector field components and estimated components for steady flow at the junction of two rectangular channels	113
7.26 Velocity tracking performance in the absence of measurement error	114
7.27 Velocity tracking performance in the presence of a measurement error of 0.125 microns	115
7.28 Velocity tracking performance in the presence of a measurement error of 0.25 microns	116
7.29 Velocity tracking performance in the presence of a measurement error of 0.5 microns	117
7.30 Relative error performance in the absence of measurement error	118

7.31	Relative error performance in the presence of a measurement error of 0.125 microns	119
7.32	Relative error performance in the presence of a measurement error of 0.25 microns	120
7.33	Relative error performance in the presence of a measurement error of 0.5 microns	121
7.34	True vector field and component estimation error for Poiseuille flow	122
7.35	True vector field components and estimated components for Poiseuille flow	123
7.36	True vector field and component estimation error for steady flow around a cylindrical obstacle	124
7.37	True vector field components and estimated components for steady flow around a cylindrical obstacle	125
7.38	True vector field and component estimation error for steady flow at the junction of two rectangular channels	126
7.39	True vector field components and estimated components for steady flow at the junction of two rectangular channels	127
8.1	Merits and demerits of the proposed method	132
9.1	Tangential and normal velocity components on a particle in a PDMS channel under the effects of electro-osmotic and electrophoretic fields	137
9.2	The two different PDMS channels used for an electro-kinetic experiment where μPSV is used for velocity estimation	139
9.3	Results for velocity estimation in PDMS channels	140
9.4	A glass-sandwiched-capillary microfluidic device	142
9.5	2-D velocity field results for a glass-sandwiched-capillary device design	143

CHAPTER 1

INTRODUCTION

The advancement of micro-electromechanical system (MEMS) technologies such as bio-analysis systems, flow sensors, micro-valves and micro-propulsion systems has helped in the development of microfluidic devices in the last decade. With more advanced and complex microfluidic devices, there has been an increasing requirement for detailed study of fluid and particle-fluid velocity fields at small scales. Information from the velocity fields gives qualitative and quantitative insight into the physics of the device. Micro-channel velocimetry has been applied to understand fluid flows near container walls and in estimating shapes and pressure. It has been instrumental in understanding the effects of particle migration and particle motion in presence of electric fields. Micro-channel velocimetry is also used for detecting biological particles and estimating biological flows, both inside and outside living tissue. Analysis of mixing in microfluidic devices and thermometry from Brownian motion are other applications of micro-channel velocimetry.

The flow channels of microfluidic devices have dimensions in the order of 1-100 μm . For such devices, the use of conventional flow measurement techniques is either impractical due to the small dimensions or inadvisable due to the potential interference with device functioning. Imaging methods are non-intrusive and a microscope with image acquisition and recording capabilities is used to image fluid flow and acquire velocimetry data. Accordingly, micro-devices are often constructed to be transparent to enable image data collection. A wide range of diagnostic techniques based on image analysis have been developed for micron resolution velocimetry and some of the more important ones are shown in Fig. 1.1 with corresponding representative works [1].

Non-intrusive velocimetry methods based on particle flow imaging have been particularly popular in the last decade and, of these, micro particle image velocimetry (μPIV) [2] has often been used for micro-channel velocity estimation. In this method the flow is seeded with tracer particles and cross-correlation between consecutive images of particle constellations at identical spatial locations is used for flow diagnosis. Laser-based illumination, an inverted microscope and a high speed camera are typically used in μPIV to

capture sharp particle images [3]. Other related approaches include particle tracking velocimetry (PTV), which works by following tracer particles over a temporal sequence of images and particle streak velocimetry (PSV), which uses the length of streaks created by tracer particles during the exposure time. PSV and PTV are more intuitive and older historically, while micro-PIV adapts from macro-scale PIV and has improved as a technique over the last decade, owing to the algorithmic efforts of several researchers and also the advancement of high-speed imaging technology.

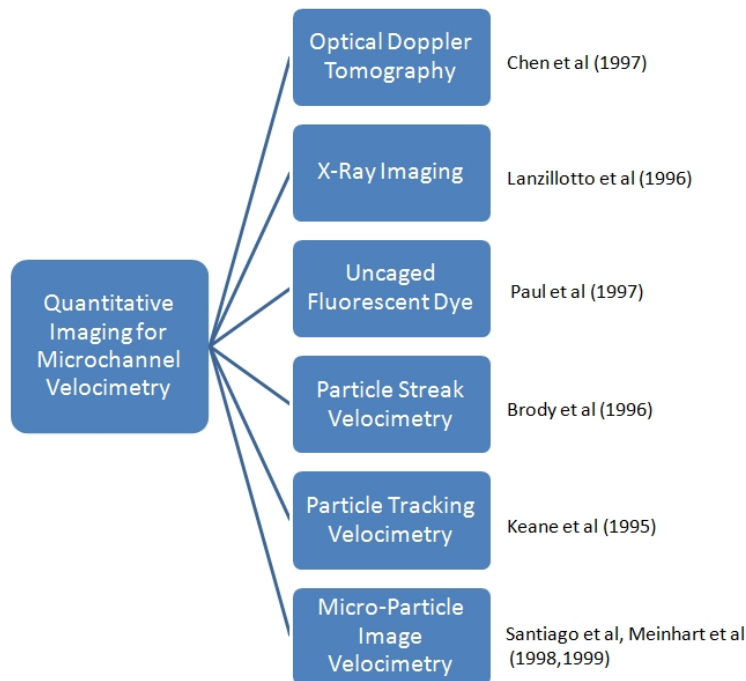


Fig. 1.1: Quantitative imaging methods for micro-channel velocimetry

While studies on μPIV have shown it to be effective, its image acquisition requirements are stringent, costly and entail difficult set up. In addition to their high cost, laser-based μPIV illumination systems need cautious handling and suffer from interference problems [3]. Also, high-speed flows require costlier and more complex image acquisition hardware. As an alternative method that is cheap, quick and yet effective, an innovative use of particle streaks is developed in this dissertation. In contrast to PIV based

methods, which impose quality requirements on the camera to prevent signal decorrelation due to particle motion blurs (streaks), the information conveyed by the streaks is exploited, thus implicitly relaxing the hardware requirements. The mathematical modelling of particle streak lengths in the micro-channel context and the associated computer vision and image analysis methods that aid this velocity estimation procedure are the foundational themes in this dissertation.

The rest of the document is outlined as follows. Micro-particle Image velocimetry is one of the most popular methods and shares some common experimental aspects with the proposed method. Accordingly, Chapter 2 in this dissertation provides some background on μPIV and discusses relevant theoretical results. In addition to introducing the main concepts and experimental limitations and control parameters of this widely used method, this chapter also illustrates how the method set forth in this work is different. Following the discussion of μPIV , μPTV is also described before introducing the proposed method. The acronym PTV has occasionally been used for particle streak based velocimetry in standard literature. This chapter explains the reasons for such use and also defines and demarcates these methods.

Chapter 3, discusses the proposed mathematical modelling in detail. The relevant connection of particle tracks to Lagrangian and Eulerian velocity fields is explored and the approximations and assumptions made in the realm of microfluidics measurements are explained. Some mathematical relations are also derived in this chapter. Some of these are specific to a generic mathematical model while some are more specific to particular experimental schematics. The main purpose of parametric mathematical modelling of streaks is to solve the inverse problem; i.e., to estimate the velocity field by estimating the model parameters of an approximation from experimental observations. Statistical methods used to estimate the model parameters and the applicability of the mathematical model to velocity fields in microfluidics are also discussed in this chapter.

One of the main motivations for this work was to make micro-channel velocimetry simpler and cheaper for routine experiments. Chapter 4 discusses common problems asso-

ciated with tracer based quantitative imaging (QI) techniques. Experimental considerations are also reported, based on knowledge acquired from the analysis of real experimental data and simulations. Velocimetry issues relating to depth, occlusion and defocussing are discussed to some detail in this chapter and some required corrective strategies are elaborated in this and the next chapter. Further, important factors controlling image acquisition that lead to improved image analysis performance are also discussed.

Chapter 5 specifically deals with image processing algorithms that are used for extracting features from streaks. The formation of streaks is discussed briefly to set the background and this is followed by discussion of the the methods used for determining the end points of streaks in images. Image processing and statistical methods leading to correction of occlusion and defocussing issues are described. For a solitary particle track on an image frame with no tagged temporal information, a directional ambiguity is evident. A simple technique based on local orientation used to mitigate this problem is presented in this chapter.

Obtaining gold standard experimental data for analysis presented a substantial challenge during the course of the dissertation work. For data sets generated in real experiments, it is often impossible to find the true velocity fields. Finding publicly available benchmark particle streak data for known velocity fields was even more difficult. Instead of using a another method for comparative measure (e.g., μPIV) gold standard particle-track image data was generated by simulation. This particular effort led to the design of a novel framework which generates exposure time controlled particle flow image sequences for arbitrary user generated velocity fields. Chapter 6 describes the problems in implementing such a framework and then delineates methods to solve these problems.

In Chapter 7, the performance of the proposed methods for 1-D and 2-D velocity estimation and the improvements suggested in Chapter 3 for the point assignment of average Lagrangian velocity on the particle track extent are discussed. Computation time performance of the particle track image simulation methods for 1-D velocity fields and qualitative performance for the simulation of 2-D particle track images are also discussed

in this chapter. Following this, Chapter 8 takes a look at the advantages of the proposed methods and points out some of their intrinsic and correctable limitations.

Chapter 9 describes some examples of the application of the proposed methods in the context of micro-channel velocity estimation for electrokinetic and hydrodynamic studies in polymer and glass based channels. Finally, Chapter 10 describes some avenues for future investigation.

CHAPTER 2

BACKGROUND

The work in this dissertation originated from an attempt to estimate a 1-dimensional spatial velocity field for an electrophoretic capture experiment conducted in the micro-regime. Subsequent literature survey in the use of tracer images for velocimetry led us to PIV and its micro-domain counterpart, μPIV . Literature survey on μPIV and the difficulty in procuring a high-speed imaging setup motivated the search for a cost-efficient method, ultimately leading to this work. While a detailed discussion on μPIV and PTV is outside the scope of this dissertation, some of the important and most directly relevant concepts for these methods are discussed next for completeness.

2.1 MICRO PARTICLE IMAGE VELOCIMETRY AND PARTICLE TRACKING VELOCIMETRY

The measurement principle for μPIV was introduced in 1998 by Santiago et al [2] and is fundamentally based on PIV for large scale applications. Macro-scale PIV was developed as early as 1984 by Adrian[4] and Pickering[5] and other co-workers and has been reviewed extensively by Adrian [6, 7], Grant [8] and Raffel [9]. Digital particle image velocimetry (DPIV) is the present form of macro PIV that is used and a fundamental study on DPIV was performed by Westerweel [10].

For large scale applications, the technique uses conventional microscopy and digital imaging methods for the quantitative determination of two-component velocity data in a two-dimensional measurement plane. A transparent working medium is used and optical access is provided to the area of investigation. The flow is seeded with tracer particles for observing the fluid motion. In the case of μPIV , similar set up is used but in micron resolution. Macroscopic PIV uses a sheet of light for defining the measurement plane. In μPIV volume illumination is used in which the entire depth of the test section is illuminated and the measurement plane is defined by the depth-of-field of the recording lens. These measurement planes are sharply defined, allowing quick transition of particles from being in-focus to out-of-focus.

During image acquisition all tracer particles emit light, but only the light originating from tracer particles in the focus plane of the microscope objective (and of those slightly out of focus) is collected by the optics and the position of those tracers is captured on a digital camera at one instant of time t_1 . After a short time interval Δt the tracer particles are illuminated again and their position is recorded on a second digital image at time t_2 . Typically a pulsed light source that is synchronized with the digital camera is used. The synchronization is done in such a way that the time interval Δt is independent of the camera frame rate, but defined by the time interval between the two synchronized light pulses and is adjusted to the flow conditions.

In the presence of fluid motion, there would exist a difference in the positions of the tracer particles in the two consecutive recordings. The tracer particles with velocity ' v ' have shifted by a displacement Δs such that

$$v = \frac{\Delta s}{\Delta t} = \frac{\Delta s}{t_2 - t_1} \quad (2.1)$$

where ' v ' is the velocity in the focal plane. The two digital images are sent to a computer, where they are stored together with the time information. In a successive evaluation step the particle displacement Δs is digitally evaluated from the image pair mainly by correlation approaches. Fig. 2.1 shows the basic idea of μPIV . For the simplest cross-correlation based image processing algorithm, the two images from successive pulses are subdivided into non-overlapping interrogation regions (sub-windows). The 2-D cross-correlation function is normally evaluated in the spectral domain and can be written as

$$R(s, t) = F^{-1} [F^* \{f_{I,J}(i, j)\} F \{g_{I,J}(i + s, j + t)\}]$$

Here, f and g are the two images, F and F^{-1} are the Fourier operators and i, j is the pixel position in the I, J sub-window. The location of the peak in the R plane gives the displacement of the particles within the interrogation region.

Excellent reviews on μPIV can be found in the works of Wereley et al. [11], Williams et al. [12], Lindken et al. [3] and Meinhart et al. [1]. The development of μPIV

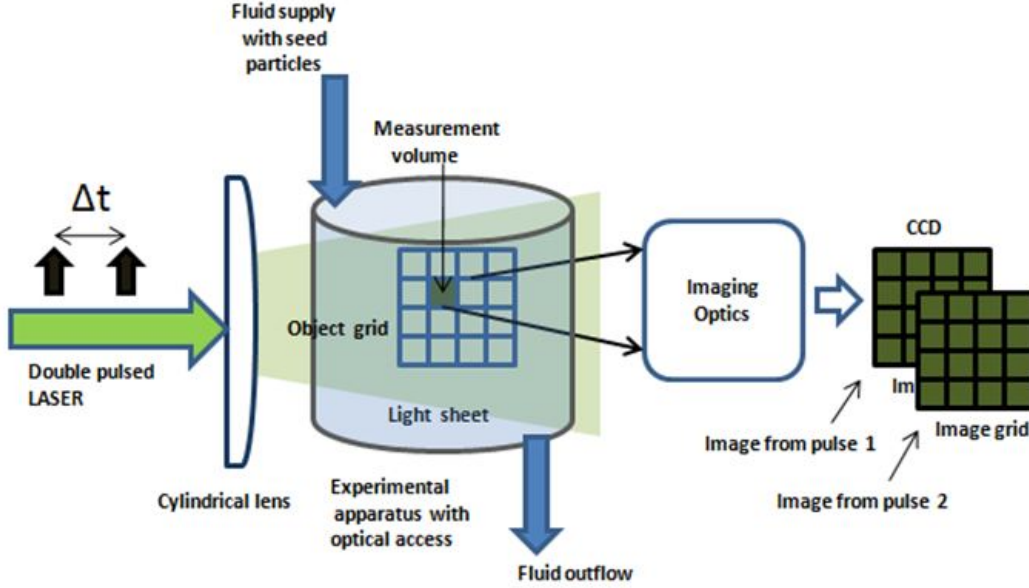


Fig. 2.1: The PIV method: Basic idea

further motivated research on macro-scale PIV, leading to important findings on PIV control parameters. One of these is the expression for thickness of the measurement volume and is expressed in terms of the depth of correlation over which the particles contribute significantly to the correlation peak position and height. It is commonly accepted to use the following expression derived by Olsen and Adrian [13] and Bourdon et al. [14]:

$$\delta_{DOC} = 2 \left[\frac{(1 - \sqrt{\varepsilon})}{\sqrt{\varepsilon}} \left(\frac{n_0^2 d_p^2}{4NA^2} + \frac{5.95(M+1)^2 \lambda^2 n_0^4}{16NA^4} \right) \right]$$

In this expression d_p is the image diameter, λ is the light wavelength, M is the image magnification, n_0 is the refractive index of the lens immersion liquid, NA the numerical aperture of the lens and ε is the relative threshold of defocussed particle contribution (which is normally set at 0.01).

Another important consideration is the limitation on the particle size set by Brownian motion. The error due to Brownian motion relative to the mean in-plane displacement is given by [2] as

$$e_{BM} = \frac{\langle s^2 \rangle^{1/2}}{\Delta x} = \frac{1}{u} \sqrt{\frac{2D}{\Delta t}} = \sqrt{\frac{2}{\Delta t} \frac{k_B T}{3\pi\mu d_p}}$$

Here, D and k_B are the diffusion coefficient and Boltzmann constants respectively, T is the temperature in Kelvin, μ is the dynamic viscosity, $\langle s^2 \rangle^{1/2}$ is the RMS of the typical fluctuations due to Brownian motion.

The μPIV technique has several advantages such as being a two-frame method, flexible to design, and using the FFT for computation speed-up. However it also suffers seriously from the effects of Brownian motion, which constrain the use of larger particles that show higher scattering. Optical diffraction limits the minimum achievable resolution of a μPIV system. This is observed from the expression of particle image diameter [13] given by

$$d_e = \left[M^2 d_p^2 + 5.95(M+1)^2 \lambda^2 \left(\frac{n_0}{2NA} \right)^2 \right]^{\frac{1}{2}}$$

where the diffraction term is independent of the particle diameter d_p and becomes dominant if the particle diameter is small. From Raffel et al. [9], the particle diameter image on the sensor (d_e) should be in the order of 2-3 pixels. It may be noted that particle intensity also decreases with decreasing particle diameter [6] but, on the other hand, particle size must be sufficiently small compared to the length scale of the flow [15]. The random error amplitude in the measured displacement depends on the diameter d_D of the displacement correlation peak as

$$\sigma_{\Delta x} \approx c \frac{d_D}{\sqrt{2}}$$

where c is an experimental constant.

A carefully selected seeding density is also very important for optimal performance of μPIV [3]. While high density seeding is apparently beneficial in a spatial correlation based method, this increases background noise and causes particle agglomerations. A preferred alternative is to increase the particle count virtually by correlation averaging [16]. High speed synchronised imaging is a necessity for μPIV which sets a higher standard for the hardware and attempts to completely avoid velocity smears. The μPIV method targets the mean velocity for a group of particles which inherently does a low pass filtering of the velocity field.

The performance of μPIV deteriorates in the presence of large velocity field gradients due to spatial stretching of the tracer constellation. The presence of shear gradients increases the random error due to a broadening of the correlation peak diameter [17, 6]. Discussion of this problem can be found in the works of Westerweel [18] and Meunier [19]. Lastly, most μPIV implementations require the removal of spurious velocity vectors in the post processing stage which makes it eventually a multi-frame method as well as reliant on temporal (and spatial) statistics. Examples of correction methods and discussions on improving the local field effects and problems arising due to the size of the interrogation region can be found in the work of Nogueira et al. [20, 21], Takehara [22], Wereley [23] and Hart [24].

Despite the above mentioned problems, μPIV remains one of the most accepted standard procedures of quantitative imaging in microfluidics. Turnkey systems are presently commercially available from TSI (www.tsi.com), LaVision (www.lavision.de) and Dantec Dynamics (www.dantecdynamics.com).

The principle of PTV is much more intuitive in comparison to PIV and differs from PIV in the tracking of actual tracer particles across frames and not a group of particles. The basic PTV approach to velocity estimation is to measure individual particle displacement, located at an arbitrary point in space and time. The velocity is calculated as:

$$u(x, y, t) = \frac{\Delta \xi(x, y, t)}{\Delta t}$$

It is easy to observe that in the limit $\Delta t \rightarrow 0$, we arrive at the fundamental definition of velocity. Accordingly it is no surprise that PTV preceded PIV as a quantitative imaging technique [25]. In general PTV refers to a group of techniques for which the tracer density is sufficiently low that an image captures non-overlapping and non-interfering tracer particle images which may be tracked across multiple frames to obtain velocity estimates. PTV is also known as Lagrangian particle tracking (LPT) due to the implicit following of the Lagrangian time-path for a particle for velocity estimation. The basic idea behind PTV is illustrated in Fig. 2.2.

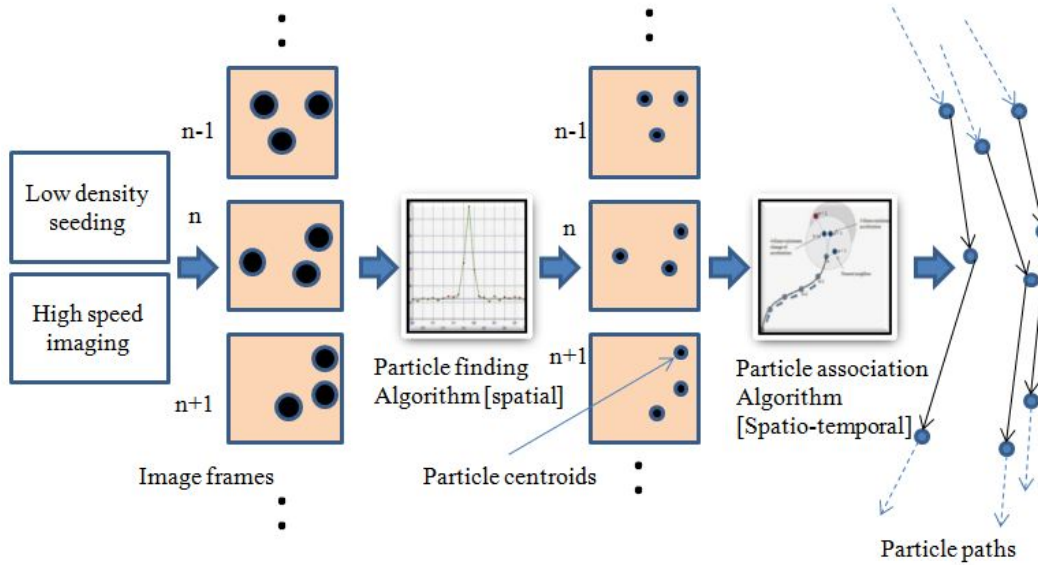


Fig. 2.2: The PTV method: Basic idea

While PIV is more systematic, the performance of PTV strongly depends on the analysis algorithms. Detailed reviews on various algorithms for PTV can be found in the works of Cheezum et al. [26], Carter et al. [27], Ohmi et al. [28] and Ouellette et al. [29]. The construction of particle tracks over space and time is the final goal of PTV. This essentially leads to the determination of the pathline for a velocity vector field and can be used to directly determine the approximate the Lagrangian velocity. The problem of constructing the particle track can be subdivided into the problems of particle centroid localization and the problem of following the particle centroid in time. In order to determine particle centers, the processing algorithm must have sub-pixel accuracy and be able to handle missing particles as well as overlaps. Moreover, the algorithm needs to have a robust noise performance. The most common methods used for particle finding are weighted averaging and Gaussian fitting [25].

Tracking a large number of particles over many frames is a multidimensional assignment problem which is NP hard. Thus, tracking algorithms often reduce the complexity by using a limited number of frames at a time to get an optimal solution over that set, in-

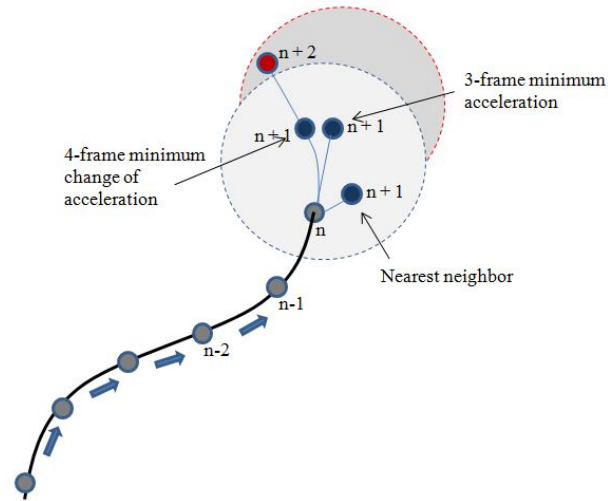


Fig. 2.3: Particle association algorithms

stead of using all the frames to construct all the tracks for all the particles. One of the common heuristics used for particle tracking is the nearest neighbour criterion, where the nearest particle in the next frame is chosen as the next sample point. Another is the 3-frame minimum acceleration method, where the position of the particle in the $n - 1$ st frame as well as the n th frame is used to find the particle position in the $n + 1$ st frame. The 4-frame minimum change in acceleration method is yet another method where the position of the particle in the $n + 1$ st frame is found as in the 3-frame method but the particle position is also found for the $n + 2$ nd frame and this is used to select that particle within the search region for which the change in acceleration is smallest between the $n + 1$ st and $n + 2$ nd frames. Fig. 2.3 shows the different methods of particle association for PTV. Various improvements in performance and the analysis of PTV can be found in the literature [30, 31, 32, 33, 34], and a few of these, where the PTV algorithm uses images of particle streaks will be discussed later. Common factors in most proposed PTV improvements and comparative reviews are either strategies for improving particle association, particle centroid localization or correction of particle loss (or gain) errors.

In comparison to the standard PIV, PTV has two main advantages. The first is that the velocity can be localized within the extent of the particle track while for PIV, the

mean group velocity is targeted. The other distinct advantage of PTV is that, for a single particle, tracking over 3-dimensional space can be achieved by the use of multiple acquisition systems [28]. For PIV this becomes a much more complicated problem involving pairwise cross correlation for the three axes. The major drawback of PTV stems from the basic assumption of traceability of individual tracers across consecutive frames [25, 35]. The usual assumption that the concentration of particles is low enough such that the maximum displacement of a tracer in some time Δt will always be less than the average spacing between nearest neighbors (particles), often breaks down during actual experiments. Moreover, tracer particles have extremely similar features (within manufacturing deviation margins) meaning one particle is hard to distinguish from others in a group. Hence there is typically an association problem to be solved while tracking particles across image frames, the difficulty increasing with particle density. Apart from this there are errors arising from sampling of the Lagrangian path and the interpolation techniques used for interpolating over an arbitrary velocity field. Image segmentation and classification of streaks are also important problems and a discussion on this can be found in the work of Rosenstiel [36].

2.2 PARTICLE STREAK VELOCIMETRY

Particle streak velocimetry is actually a subset of particle tracking velocimetry. Particle streaks are formed when higher exposure times are used for imaging and the motion of the particle gets imaged as connected pixels in the image plane. Hence streaks are essentially particle tracks and the endpoints may be used as particle positions within a frame and the curve joining them is the track formed during the exposure time. While connecting particles across consecutive frames however, the similar association problem is encountered. Particle streaks are not fit for use in the standard PIV methods as the nature of their spatial extent causes decorrelation and loss of accuracy in peak detection for the PIV procedure. However, PSV shares the same advantages of PTV and is implicitly a more accurate method than PIV, since in the ideal situation it can obtain much more resolved Lagrangian velocity values than the mean group Eulerian estimates obtained from PIV. The problem of association in

PTV can affect PSV if the streaks need to be connected prior to determination of the local velocities. The problems of occlusion and overlap are also present for the use of streaks, and perhaps in larger measure owing to the increase in the probability of overlap due to the increase in the spatial extent. Hence successful use of PSV demands low seeding density and sharp imaging of particle streaks.

Owing to its inherent simplicity, the use of particle streaks for velocimetry is perhaps the oldest, in conjunction with PTV [37, 38, 39, 40]. The use of streaks can be traced back to streak-photography where the images were manually analyzed. The method of the analysis was to estimate the length of the streak and divide it by the time of exposure to get average velocity values and the statistics of this method of was discussed as early as 1991 by Altman [41]. While being closely related, some PSV methods do not involve tracking and use the streak length directly to get the local velocity vector [37, 38, 39, 42, 43, 44, 45], while for many others tracking is the goal [46, 47, 48]. The consideration of tracking implies that the endpoints of the streaks need to be connected to other streaks in the previous and subsequent frames, the time difference being the inverse of the frame rate. As one would expect, the latter method is more involved (often requiring extensive algorithms for solving the association problem) but can eventually produce better results. For reasons of clarity, in this dissertation we choose to call the latter methods PTV and the former one PSV where the streaks are made use of by themselves and not for tracking.

We observe that there have been many instances where particle streak lengths have been used, but their use has often been limited to macro-scale velocimetry and for estimation of 1-dimensional velocity fields (1D1C), and often as point or bulk estimates. However, the work done by Bergthorson et al. [49, 50, 51] and Hering [52] for macro-scale flow deserves special mention as the former uses the particle track length for velocity correction and the latter attempts to model the streak's gray value in an image for velocity estimation. Another interesting observation can be made on the development of PIV, PTV and PSV. PSV is the oldest method and its use can be found as early as 1934 [35]. As digital imaging and high speed computations became possible, particle tracking became feasible and PTV

dominated. With the advancement of high speed imaging techniques and lasers and even better computing power, μPIV has now become the more used method.

While other factors may have contributed towards the restricted use of particle streaks by themselves, the problems of overlapping and occlusion, the extended spatial uncertainty of the position of the particle and the implicit idea that particle streaks are imperfections and velocity blurs were the more significant reasons. However, if particle streaks could be efficiently utilized, one sees at once that hardware requirements immediately become simpler and the directional nature of the particle streaks can be exploited to our advantage. Surprisingly to the best of our knowledge, there has not been a dedicated study on the sole use of particle streak length or on what could be achieved from the analysis of streak-length. This observation is even more prominent in the nascent domain of microfluidic research in the current decade, and this is where micron resolution PIV is the default standard.

2.3 THE PROPOSED μPSV METHODS

A novel method of using particle streaks for micro-domain 2D2C velocimetry is proposed in this work. We propose to use particle lengths within a model-framework that assumes a locally-linear velocity field. As will be explained in the chapters to follow, the local linear assumption helps use the streak lengths efficiently without directly confronting the association problem. We call the proposed method μPSV as the method relies on velocity field smoothness which works best in the micro-domain and we essentially use streaks (length) by themselves and not for the purpose of tracking. The final goal for the proposed method is to obtain accurate estimates of the local Eulerian velocity on the spatial extent of the particle streak. It may be noted that the smoothness assumption restricts the applicability of the proposed method to micro-domains only.

Similar to any other image based velocimetry method, we start with the acquisition of tracer particle images. Low particle density is preferred as higher particle densities increases overlap between streaks. A stack of frames with particle streaks covering the region

of interest (ROI) is thus the input. The images are firstly processed to minimize the noise and imaging artefacts. Blurred and non-ellipsoidal objects are removed by morphological image processing. Streaks are then segmented by local adaptive thresholding and fitted in a bounding box. The width W and the height H of the box represent the exposure time-weighted local horizontal and vertical velocity components respectively. Further details of the image processing part are discussed in Chapter 5 but at the end of the image processing step, the component values are stacked separately, for each spatial location. Hence we get two tables (for two components) with the observed streak descriptors corresponding to spatial locations. Note that target for the image processing is to just get the streak descriptors and the image processing methodology is not unique. Any alternate method that leads to a similar intermediate streak descriptor table would serve the purpose.

The histogram of the temporal data at a spatial position is analyzed and outlier data points are eliminated based on the local mean, median and standard deviations from the spatio-temporal stack. In our processing, streaks with lengths more than 2 standard deviations over the mean were eliminated. At this point 3 different directions are possible leading to the estimation of local velocity vectors. Firstly, there is the basic $\frac{L}{T}$ approach and this value is usually assigned to the center of the streak. This is the classical method of PSV which is actually PTV neglecting the tracking. However, this method of assignment does not work well for gradient fields and this is discussed in detail in Chapter 3 where strategies of improving the efficiency of this point-assignment method are also described. Note that the streak has a much bigger extent marking the particle path during exposure, thus making the single-point-assignment (estimation) of velocity somewhat inefficient.

Another direction is to perform temporal averaging of the length components 'observed' at a particular point in space and then divide the result by time. The basic idea is that streak lengths occur as a cumulative growth, with the local Eulerian velocity at each point in space being responsible for additively contributing to the total length. Thus when lengths at a point are averaged temporally (across multiple frames), it is actually a weighted average. The local Eulerian velocities are the weights biasing the average towards the correct veloc-

ity estimate. Such a method can estimate a piecewise-uniform approximated velocity field quite accurately and this is discussed in Chapter 3. Further, we also show that this method performs well for smooth velocity fields with small local gradients. By processing both the length components, we obtain the 2D2C velocity field estimates. With a large number of streaks observed at a point the mean statistic would also be reliable. It may be noted that we were unable to find the use of spatial averaging of particle streaks for velocimetry in the micro-particle velocimetry literature to the best of our efforts.

While temporal averaging of spatial streak information performs well, its velocity estimates are typically higher than or below the actual velocities due to the bias introduced, unless the velocity field is uniform or at least piecewise uniform. To obtain a better estimate, a local linear model of the Eulerian velocity is used. With this assumption of a local linear velocity field, it is possible to derive closed form expressions for the streak lengths themselves and then use this expression and the available streak descriptors to calculate the local velocity field parameters. Using the local velocity field parameters, we can then obtain much better estimates of the local velocity field. In chapter 3, the first-order approximation is introduced and the methods for obtaining velocity estimates using this approximation are discussed. The development of the theoretical expressions and results for a first-order approximated velocity vector field form a considerable part of this dissertation. To the best of our knowledge, this method has not been used earlier for micro-channel velocimetry.

Thus, in effect, three methods are proposed based on the particle streak descriptors. The first one is a corrective strategy while the other two are novel methods of using the particle streaks by themselves, for velocity estimation. As one might observe, the proposed μPSV method (which includes all the three methods originating from the same information table) varies in a number of ways from μPIV and PTV. These are summarized as follows.

1. The proposed μPSV method is completely based on individual particle streak descriptors (length and starting point), μPIV is based on particle groups and PTV is based on tracking the position change of individual particles.

2. The proposed μPSV method is not dependant on fast imaging for accuracy or traceability unlike both μPIV and PTV.
3. The proposed μPSV method depends strongly on seeding density. A low seeding density is preferred. Similar is the case with PTV but for μPIV , a higher seeding density is desirable.
4. The proposed μPSV method uses exposure time as a sampling control parameter. For μPIV the spatial sampling is controlled by setting a grid-size for cross-correlation while for PTV, the frame-rate is used for sampling the Lagrangian pathline.
5. The proposed μPSV method depends more on sharpness of streak end-points than tracer image intensity, unlike μPIV where the cross-correlation peak sharpness directly depends on the intensity.
6. The dataset for proposed μPSV method implicitly conveys directional information by a single frame. This is not so for either μPIV or PTV.
7. The proposed μPSV method directly yields well resolved Eulerian velocity estimates over the entire streak length while μPIV leads to the estimation of average Eulerian velocity and for PTV we obtain discretely sampled Lagrangian velocities along the particle path.
8. The proposed μPSV method explicitly uses a local linear approximation of the velocity field. In the case of μPIV or PTV, this is assumed implicitly used indirectly.

Details of the proposed analysis methods are covered in the chapters that follow. Quantitative verification of the methods proposed are obtained by simulation with the aid of CFD tools. The generation of baseline or gold-standard data is explained in Chapter 6, where we propose some methods for reducing the simulation time. The simulated baseline data generation method sharply contrasts the standard Monte-Carlo schemes used in literature for quantitative PIV verification. The difference arises from the fact that generation of a finite time particle tracks on a single frame is different than the generation of two frames with point particles with a simple shift between them. The latter is a good approximation to

particle displacement only under the assumption of high speed imaging and this is impossible for the former case. However a method that allows for the variability of both exposure time and frame rate is more realistic and can be used to simulate high speed imaging. The basic problem that needs to be solved for this is the generation of finite time particle tracks from discrete Eulerian data. This means we would have to work with 2-D samples of an arbitrary velocity field which naturally leads to the use of computational methods. Some novel schemes are proposed in this dissertation to reduce the computation time with minimal reduction in accuracy. Further the direct usage of CFD data from tools that allow a user to design a microfluidic schematic makes the method extremely useful for designing trial experiments.

CHAPTER 3

PARTICLE VELOCITY VECTOR FIELDS, SAMPLING AND ESTIMATION

Flow visualization and flow estimation of velocity fields are two well known problems in the field of fluid dynamics. The problem representations as well as their solutions both stem from the definition and approximation of velocity vector fields. We begin this section with an introduction to two representations of fluid and particle-fluid motions.

3.1 EULERIAN AND LAGRANGIAN VELOCITY REPRESENTATIONS

Fluid and particle-fluid flows may be observed by tracking small, distinguishable fluid material volumes that are carried with the flow, the Lagrangian method, or by observing the fluid velocity at fixed spatial locations, the Eulerian method. Conservation laws are inherently Lagrangian because they pertain to fluid volumes and not to spatially fixed locations in the domain of the flow. While Lagrangian laws are the natural choice for many observational techniques and for stating fundamental conservation theorems, the theoretical development of fluid mechanics has been mostly Eulerian [53]. The notion of Eulerian velocity field becomes even more prominent for describing particle flows in a liquid medium where the hydrodynamic forces are small compared to the electrical forces. The velocity expressions arising from force balance procedures often lead to spatial velocity descriptions, so we can express the velocity at all the points in space for a traversing particle but the Lagrangian representation will need to be invoked when we deal with space-time descriptions.

In Fig. 3.1, the relationship between the two forms of velocity representations is shown. The Lagrangian form is concerned with the motion of the blue fluid volumes along the black trajectory while the flow sensors obtain a snapshot of the Eulerian velocity.

3.1.1 *The Lagrangian representation*

In the Lagrangian representation we track specific volumes of a scalar quantity. In order to do this, we tag this material volume (parcel) by its initial position, and its inherent properties change with time. The parcel trajectory is called the pathline. We define the pathline as

$$\xi = \xi(x_0, t) \tag{3.1}$$

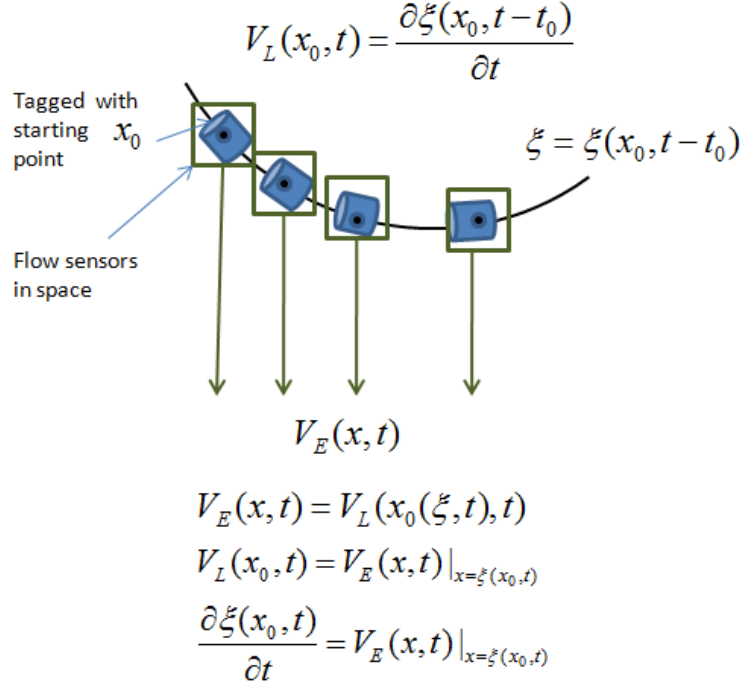


Fig. 3.1: Lagrangian and Eulerian velocity fields

The derivative of the pathline gives the Lagrangian velocity, where the initial position x_0 is kept fixed

$$V_L(x_0, t) = \frac{\partial \xi(x_0, t)}{\partial t} \quad (3.2)$$

It is assumed in the representation that the mapping from x_0 to ξ is continuous and unique in that adjacent particles will never be split apart and one parcel will not be forced to occupy the position of another parcel as they have been tagged with different x_0 values. So particle trajectories starting from different spatial positions are unique to that instantaneous observation. In the context of particle streaks, this means that under ideal conditions of focal plane imaging, no two streaks can start at exactly the same place. In some sense this is also physically not possible as it would mean two particles in the exact same position in the focal plane, but both of them are in focus.

Under the assumption of unique mapping, the pathline equation is invertible, which means that x_0 can be expressed as a function of the trajectory ξ . This means that Eulerian

and Lagrangian representations can be interchanged, at least in principle. The Lagrangian representation presumes knowledge of the starting position x_0 and treats it as an independent variable based on which the subsequent position ξ is known. In the Eulerian representation, the instantaneous position $\xi(t)$ is the independent variable and x_0 responsible for this position is the dependant variable.

3.1.2 *The Eulerian representation and device physics*

Another method to observe the fluid velocity is by means of transducers that we could place at fixed positions, x . The transducers would essentially sample the velocity field at fixed positions. The velocity so obtained is termed the Eulerian velocity, V_E , and is intended to be the velocity of the fluid parcel that is present, instantaneously, within the fixed control volume sampled by the transducer. In the case of particle motion under electric field in fluid medium, the particle's instantaneous spatial velocity is dependent on the spatial variation of the electric field. The velocity field so obtained depends only on the position and hence is an Eulerian velocity field. In microchannel velocimetry, the spatial representation of the velocity field is the more sought after.

3.1.3 *Interconversion between representations*

Assuming that the particle trajectories can be inverted to yield $x_0(\xi, t)$, we can write the expression for V_L as a composite function $V_L(x_0(\xi, t), t)$ whose dependant variables are ξ and t . This can now be written as a function of x and t alone as

$$V_E(x, t) = V_L(x_0(\xi, t), t) \quad (3.3)$$

Thus a spatial sampling of the Lagrangian velocity field leads to a knowledge of the Eulerian velocity field. This is the central idea on which tracer based velocimetry works. For example, all PIV methods inherently measure the Lagrangian velocity of particles [6]. The basic analysis procedure of such methods involves the generation of the Eulerian velocity field from Lagrangian data by interpolating or mapping irregularly sampled Lagrangian data onto a spatial grid. To know where to assign the velocity, knowledge of the position is required.

Similar to the earlier conversion, $V_L(x, t)$ can be written as

$$V_L(x_0, t) = V_E(x, t)|_{x=\xi(x_0, t)} \quad (3.4)$$

However in this case there is no direct sampling but the velocities are linked by the path equation. If the Eulerian velocity is known, we can first get the path equation by solving the differential equation

$$\frac{\partial \xi(x_0, t)}{\partial t} = V_E(x, t)|_{x=\xi(x_0, t)} \quad (3.5)$$

and then the Lagrangian velocity may be obtained by differentiating the path equation.

3.2 VELOCITY VECTOR FIELDS

A vector field f is a map $f : \mathbb{R}^n \rightarrow \mathbb{R}^n$ assigning to each point x in n dimensions a n -component vector $f(x)$. For our purposes, the velocity vector field is a 2-dimensional, 2-component (2D2C) velocity vector field in a microfluidic system. Further, we make a comment on fluid and particle velocity fields as follows. Microfluidics is concerned with the motion of fluids and particles in fluids. When the former is of greater concern, the particles play the role of tracers which follow and represent the fluid flow. In the latter case, the flow of particles themselves is more important and the fluid merely plays the role of a medium. An important point to consider is that in the former case, if we were to track the particles, then there always exists some degree of error about the inferred fluid motion from the particle motion. However in the latter case, as in the case of experiments involving particle motion in microchannels due to electric fields, the associated velocity estimation errors are not due to propagation or inference, but directly related to the velocity estimation process. Accordingly, there are lesser worries about how faithfully the tracer particles are representing the flow.

3.2.1 Characteristic curves of vector fields

For an n -dimensional Euclidean space \mathbb{R}^n , a differentiable curve is called a tangent curve of a n -dimensional vector field $V(x)$ if the tangent vector at any point along the curve

is parallel to the vector field at that point. The tangent vector curves are solutions for the ordinary differential equation (ODE) system

$$\frac{d}{d\tau} (x(\tau)) = v(x(\tau)); x(0) = x_0 \quad (3.6)$$

Distinct tangent curves are non-intersecting and do not join each other. They are characteristic of the vector field such that for all points $x \in E^n$ where the velocity is not a null vector, there is an unique tangent curve through it and this curve uniquely depicts the directional information [54, 55]. In a time-dependent vector field $V(x, t)$ four types of characteristic curves exist. These are streamlines, streaklines, pathlines and timelines. We limit our following discussion to the first three.

Streamlines are a family of curves that are everywhere parallel to the velocity and show the direction of the velocity field at a given instant. They are defined (for a fixed observation time $t = t_f$) as

$$\frac{d}{ds} (X(s)) = v(t_f, X) \quad (3.7)$$

where s is a dummy variable representing the parametrization of the vector field and could be regarded as time. Streamlines are therefore ‘snapshots’ of the lines traced parallel to the vector field. Examples of streamlines are shown in Fig. 3.2.

Pathlines are trajectories of massless particles in time-dependent vector fields, the trajectory being defined by the streamlines. They can be expressed as

$$\frac{d}{dt} (X(t)) = v(X(t), t) \quad (3.8)$$

Pathlines are shown in Fig. 3.3.

A Streakline is the instantaneous locus of all particles that pass a given point and can be observed by steadily injecting dye into the fluid at a fixed point. They are defined as

$$\frac{d}{ds} (X(s)) = v(X(s), s) \quad (3.9)$$

Also note that the term ‘streaklines’ has a fluid dynamics origin and the particle tracks, which we loosely refer as ‘streaks’ as more of a visual inference origin (velocity blur image of a moving object).

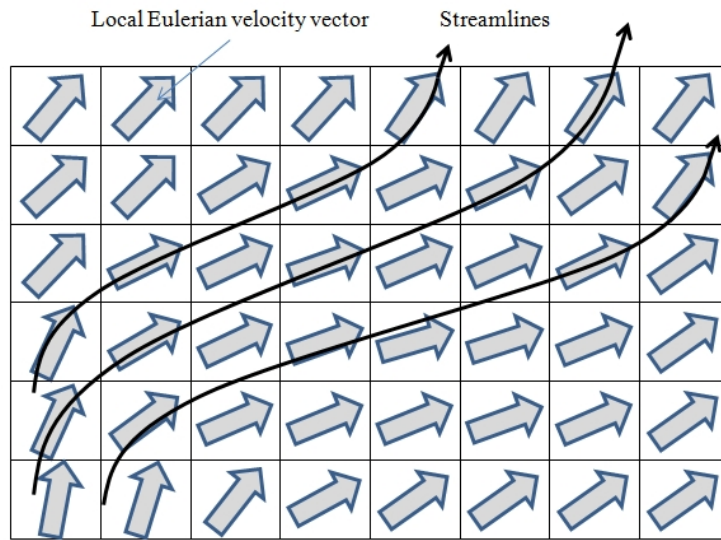


Fig. 3.2: Streamlines

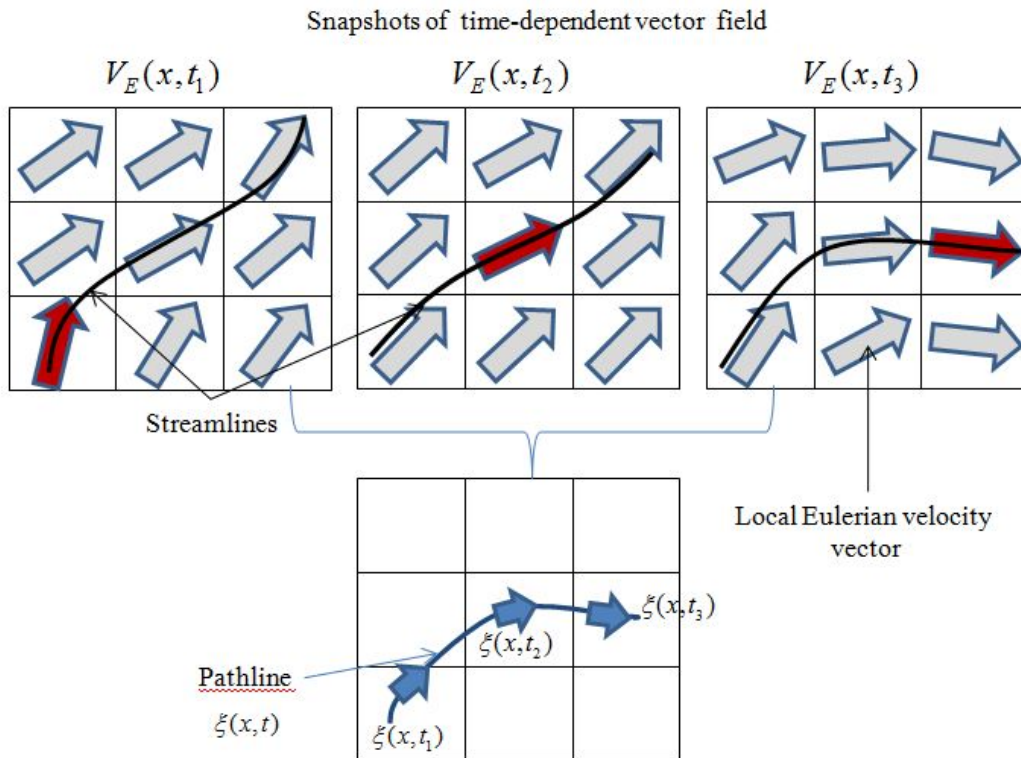


Fig. 3.3: Pathlines

The above space-time formulations for the tangent curves help us in the spatio-temporal analysis of time-dependent vector fields. In this dissertation, however we limit our scope to time-independent (or quasi time-dependent) vector fields only. In this case, streamlines, pathlines and streaklines coincide, since every ‘snapshot’ gives the same vector field; i.e.,

$$v(x, t) = v(x, t_0)$$

So, a streamline can be obtained by solving the ODE

$$\frac{d}{d\tau}(x(\tau)) = v(x(\tau), t_0); x(0) = x_0 \quad (3.10)$$

and a pathline by solving the ODE

$$\frac{d}{dt}(x(t)) = v(x(t), t); x(t_0) = x_0 \quad (3.11)$$

In the above definitions, note that the streamline definition has more to do with space (Eulerian) while the pathline equations are more time-defined (Lagrangian). If we have a finite time interval, say T in which a particle traces a curve of length L then this arc-length is given by the Eulerian description as

$$\int_{x_0}^{x_0+L} \frac{d(x(\tau))}{v(x(\tau), t_0)} = \int_{t_0}^{t_0+T} d\tau \quad (3.12)$$

and by the Lagrangian description as

$$\int_{x_0}^{x_0+L} d(x(t)) = \int_{t_0}^{t_0+T} v(x(t), t) dt \quad (3.13)$$

Note that both sides of the integral are positive. Moreover, it can be immediately observed that a time-limited segment of the tangent curve also encodes the magnitude of the vector field by its arc-length. With this information, we can formally define ‘particle-streaks’ and associate them with the local vector field.

Definition 1. *Given a time-independent n -dimensional vector field $V(x)$, a ‘particle-streak’ is defined as the image of an exposure-time-limited segment (arc) of a tracer particle pathline unique to the vector field and the starting point x_0 .*

The exposure time limit T and the image domain spatial resolution are set by the optics (microscope) and the image acquisition system (camera). The length of the particle-streak can thus be expressed as

$$L = f(x_0, V_E(x), T) \quad (3.14)$$

where $f(\cdot)$ is some parametric function.

3.2.2 Particle track lengths as line-integral sensor outputs

The finite-time particle track length can be written as a Riemann sum as

$$L = \lim_{\Delta t \rightarrow 0} \sum_{i=1}^n 1 \cdot \Delta s_i; \Delta s_i = |v_i| \Delta t$$

where Δs_i represents the finite and length intervals which make the total track length. For each of these length intervals, the time interval is fixed and a distinct velocity v_i is assigned to the particle. It may be noted as Δt tends to zero, the number of intervals ‘ n ’ become infinite. Hence the above form represents a line-integral where the function value is unity. From the image plane perspective, if each ‘ON’ pixel to ‘ON’ pixel connection for a highly resolved optical system is considered a sensor output with a value dependant on the pixel-distance between these ‘ON’ pixels, then the contiguous ‘ON’ pixels constitute an image plane representation of the particle-streak. Moreover, the image domain length is actually a linear combination of ‘ON’ sensors that are connected adjacently and the total ‘ON’ sensors that are connected diagonally. The important point to note are that the particle-track length encodes the velocity field that the particle traverses through and that the length can be expressed as a linear combination of binary sensor outputs.

3.2.3 Velocity estimation from length samples – the inverse problem

Now that we know that the length samples describe the local velocity field, (measure of the total effect of a given field along a given curve), we intend to recover the velocity field from its time-limited cumulative effect viz. the length. We immediately observe that this is an inverse problem and since the parametric function expressing L is not necessarily a linear mapping, direct inversion becomes intractable as the flow field deviates from uniform

flow. We resort to parametric modelling of the local velocity field from which expressions of streak length can be computed and these expressions and their derivatives can be fitted with the observable data (i.e., x_0 , T and L) so as to estimate the parameters of the local velocity field.

3.3 FIRST-ORDER APPROXIMATION OF VECTOR FIELDS

In section 3.2 the velocity vector field is introduced by its generic definition and later we specify the consequences of time-invariance; i.e., steady velocity vector fields. Another approximation is introduced in this section, originating from the local smoothness of velocity field property of most microfluidic systems. This particular assumption leads to a simpler approximation of the flow field and eventually aids in its estimation from experimental observables.

3.3.1 *Smooth velocity fields in microfluidics*

Flows in microfluidic devices typically are laminar and have low Reynolds number owing to the extraordinarily small area of cross-section the flow encounters. Laminar flow implies that the fluid flows in parallel layers without any disorder. The Reynolds number is defined as

$$\text{Re} = \frac{Ul}{\nu}$$

where U is the characteristic velocity of the fluid across spatial scale l and ν is the kinematic viscosity. In microfluidic systems the typical flow velocities do not exceed a centimeter per second and channel widths are on the order of tens of micrometers. Accordingly, Reynolds numbers for microfluidic systems do not normally exceed a value of 1. However, for some recent applications like the handling of cells, larger velocities are used corresponding to Reynolds numbers in the range from 1 to 20 [56, 57]. At extremely small Reynolds numbers (< 0.5), creeping (Stokes) flow is observed and viscous forces are stronger than advective inertial forces. Considering now the velocity field, it can be assumed that local velocity gradients are small as larger gradients would lead to local turbulence which is ruled out by the low Reynolds number condition, since typically a Reynolds number of 2000 is required

for turbulence [56]. Flow-field smoothness is dependant on local field gradient magnitudes and smooth flow-fields is a good approximation in at microfluidic scales [58, 59, 1].

3.3.2 First-order approximation

Consider a Taylor series expansion of the velocity vector field around a point $x = x_p$

$$V_E(x) = V_E(x_p) + V'_E(x_p)(x - x_p) + H.O.T. \quad (3.15)$$

where the higher order terms are indicated by H.O.T. With the assumption of local smoothness the higher order terms can be ignored with small error (contribution to the particle streak length) to get the first-order approximated velocity field as

$$V_E(x) = V_E(x_p) + a(x - x_p) \quad (3.16)$$

where a is the local velocity gradient. The above equation can be written more explicitly as

$$V_E(x) = V_E(x_p) + J(x - x_p) \quad (3.17)$$

where

$$J = \nabla V_E(x) = \begin{bmatrix} \frac{\partial u_x}{\partial x} & \frac{\partial u_y}{\partial y} \\ \frac{\partial v_x}{\partial x} & \frac{\partial v_y}{\partial y} \end{bmatrix} \quad (3.18)$$

The first-order approximation is rearranged to include the starting point of a particle streak (i.e., x_0) as it can be measured from experimental images. We obtain

$$V_E(x) = V_E(x_0) + a(x - x_0) \quad (3.19)$$

Collecting now the constant terms together into a variable b we get

$$V_E(x) = ax + b; \quad b = V_E(x_0) - ax_0 \quad (3.20)$$

The above equation is fundamental towards the remaining part of this dissertation. It describes the local Eulerian velocity field under the assumptions of time-invariance and smoothness. Limiting our discussion in the microfluidic regime, the above assumptions are strongly valid and the results from the first-order approximations can be applied to standard experiments in microfluidics, which is the target application area of this work.

3.3.3 Standard results for particle-tracks from first-order approximation

Some standard results are now derived for the first-order approximation. We start with the ODE expression for the pathline

$$\frac{d}{dt}(x(t)) = v(x(t), t)$$

Substituting for the velocity field we set up the following integral

$$\int_{x_0}^{\xi(t)} \frac{dx(t)}{ax(t) + b} = \int_0^t dt \quad (3.21)$$

where the path is indicated by $\xi(t)$. Solving, we get,

$$\xi(x, t) = e^{at} \left(x_0 + \frac{b}{a} \right) - \frac{b}{a} \quad (3.22)$$

$$\xi(t) = x_0 + V_E(x_0) \left(\frac{e^{at} - 1}{a} \right) \quad (3.23)$$

Note that the above equation represents both the streamline and the pathline within the spatial extent where the local linear assumption is valid.

The Lagrangian velocity field was defined earlier as the time derivative of the path equation. Hence we have

$$V_L(t) = \frac{d}{dt} [\xi(t)] \quad (3.24)$$

which gives the following expressions for the Lagrangian velocity:

$$V_L(t) = a \left(x_0 + \frac{b}{a} \right) e^{at} \quad (3.25)$$

$$V_L(t) = V_E(x_0) e^{at} \quad (3.26)$$

The path length for a finite time interval is obtained from the path equation as

$$L = \xi(T) - \xi(0) \quad (3.27)$$

which gives

$$L = \left(x_0 + \frac{b}{a} \right) (e^{aT} - 1) \quad (3.28)$$

$$L = V_E(x_0) \left(\frac{e^{aT} - 1}{a} \right) \quad (3.29)$$

The above equation expresses the particle-streak length in terms of the starting spatial point x_0 , the exposure time T and the local linear field parameters a and b . It may be noted that of these parameters, a and b are unknown while the others can be immediately obtained from an experimental image of a particle-streak.

The expression for length also helps us in obtaining the theoretical expressions for the longest and the shortest streak lengths that can be observed at a particular point. It can be seen in Fig. 3.4 that, depending on the sign of the local gradient, we have two different trends in the change of streak length when x_0 changes. For a observation point x_p the maximum length in case of positive local gradient would be for that streak which starts at x_p . Its length is given by the expression

$$L_{\max} = \left(x_p + \frac{b}{a}\right)(e^{aT} - 1) \quad (3.30)$$

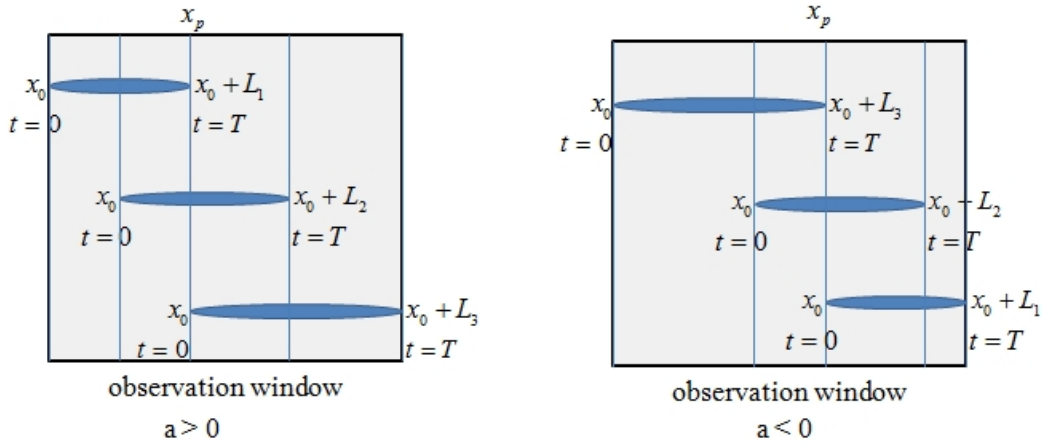


Fig. 3.4: Minimum and maximum lengths for local linear approximation

The starting point for the minimum length is given by $x_p - L_{\min}$ so that for minimum length we have

$$L_{\min} = \left(x_p - L_{\min} + \frac{b}{a}\right)(e^{aT} - 1) \quad (3.31)$$

which gives

$$L_{\min} = \left(x_p + \frac{b}{a}\right)(1 - e^{-aT}) \quad (3.32)$$

Stokes drift is an important consideration when particle tracers do not faithfully follow the fluid flow. It is defined as the difference between the average Lagrangian and Eulerian velocities. In the definition of the Lagrangian velocity, if we fix the time, then the velocity is also the local Eulerian velocity. Hence using the expression of the Lagrangian velocity obtained earlier, the minimum Eulerian velocity for a particle would occur at $t = 0$ and the maximum at $t = T$ for the local linear assumption. Hence the average Eulerian velocity is given by

$$\langle V_E \rangle = \frac{V_E(x_0) + V_E(x_0)e^{aT}}{2} \quad (3.33)$$

The average Lagrangian velocity is given by the ratio of the total distance by total time; i.e.,

$$\langle V_L \rangle = \frac{L}{T} = V_E(x_0) \left(\frac{e^{aT} - 1}{aT} \right) \quad (3.34)$$

The difference between these is the average Stokes drift

$$\langle V_S \rangle = \langle V_L \rangle - \langle V_E \rangle$$

This is expressed using the earlier equations as

$$\langle V_S \rangle = V_E(x_0) \left\{ \frac{e^{aT} - 1}{aT} - \frac{1 + e^{aT}}{2} \right\} \quad (3.35)$$

Expanding the above expression by infinite series we have

$$\langle V_S \rangle = V_E(x_0) \left[\frac{1}{aT} \left(-1 + \sum_{k=0}^{\infty} \frac{(aT)^k}{k!} \right) - \frac{1}{2} \left(1 + \sum_{k=0}^{\infty} \frac{(aT)^k}{k!} \right) \right] \quad (3.36)$$

which on simplification gives

$$\langle V_S \rangle = V_E(x_0) \left[\sum_{k=2}^{\infty} \frac{(aT)^k}{k!} \left(\frac{1}{k+1} - \frac{1}{2} \right) \right] \quad (3.37)$$

From the last expression we find that the Stoke's drift is dependent only on the product of the local gradient and the exposure time. If this product is extremely small, so is the drift such that

$$\lim_{aT \rightarrow 0} \langle V_S \rangle = 0 \quad (3.38)$$

Hence, if either T is extremely small, which implies that the particle streak is in fact a point or if the local gradient is close to zero; i.e., a uniform velocity condition, there is no difference between the average Eulerian and Lagrangian velocities over the particle track under the local linear approximation.

3.3.4 Theoretical point-assignment of average velocity for particle-tracks

Computing the average Lagrangian velocity is essentially simple as the only information we need is the streak length L and the exposure time T . However, as observed in the previous discussion, the average Lagrangian velocity is not necessarily the average Eulerian velocity and hence this velocity cannot be assigned to the center of the streak without causing an error. (With the local linear approximation of the velocity field, the average Eulerian velocity would be located at the center of the particle-streak.) Since the average Lagrangian velocity would be equal to the Eulerian velocity at some point on the streak, if we could assign the value of L/T to this exact point, then the assignment error would be zero. We have also seen that the difference in the average velocities depends only on the dimensionless product aT . We find that the location where the assignment error is zero also depends on this product.

Proposition 3.3.1. *The average Lagrangian velocity of a tracer particle forming a particle-streak of length L , equals the first-order approximated Eulerian velocity at a point completely defined by the product of the local gradient and the path time (exposure time).*

Proof. Let the velocity on the streak be $V(x)$. Then with the first-order approximation we have

$$V_E(x) = ax + b$$

We define x_p , an arbitrary point on the streak as a function of the streak length by

$$x_p = x_0 + \alpha L; \alpha \in (0, 1) \tag{3.39}$$

If the Eulerian velocity at this point equals the average Lagrangian velocity, then we have

$$V_E(x_p(\alpha)) = \langle V_L \rangle = \frac{L}{T} \tag{3.40}$$

which gives

$$a(x_0 + \alpha L) + b = \frac{L}{T} \quad (3.41)$$

$$\alpha = \frac{1}{aT} - \frac{(ax_0 + b)}{aL} \quad (3.42)$$

Now, substituting the value of $ax_0 + b$ from the expression for L , we get

$$\alpha = \frac{1}{aT} - \frac{1}{(e^{aT} - 1)} \quad (3.43)$$

The result follows.

Proposition 3.3.2. *For small values of the aT product, the $\frac{L}{T}$ ratio can be assigned to the midpoint with minimal error.*

Proof. The length fraction α where the $\frac{L}{T}$ ratio can be accurately assigned is given by

$$\alpha(aT) = \frac{1}{aT} - \frac{1}{(e^{aT} - 1)}$$

where α is written as a function of the aT product. Now taking the limit we have

$$\lim_{aT \rightarrow 0} \alpha(aT) = \lim_{aT \rightarrow 0} \left\{ \frac{1}{aT} - \frac{1}{(e^{aT} - 1)} \right\} \quad (3.44)$$

Or,

$$\lim_{aT \rightarrow 0} \alpha(aT) = \lim_{aT \rightarrow 0} \left\{ \frac{e^{aT} - 1 - aT}{aT e^{aT} - aT} \right\} = \lim_{aT \rightarrow 0} \left\{ \frac{\frac{d}{d(aT)} (e^{aT} - 1 - aT)}{\frac{d}{d(aT)} (aT e^{aT} - aT)} \right\} \quad (3.45)$$

where the last part is obtained by the application of the l'Hôpital's rule. This gives

$$\lim_{aT \rightarrow 0} \alpha(aT) = \lim_{aT \rightarrow 0} \left\{ \frac{e^{aT}}{e^{aT} + aT e^{aT} + e^{aT}} \right\} \quad (3.46)$$

Finally, applying the limits we have

$$\lim_{aT \rightarrow 0} \alpha(aT) = \frac{1}{2} \quad (3.47)$$

The result follows.

The velocity error of incorrect assignment can be quantified by the relative velocity error. An advantage of using the relative error is that it is dimensionless and easily comparable. In order to get the absolute error, we simply multiply by the actual velocity value. We define the relative error as below.

$$e_r = \frac{V_{\text{true}} - V_{\text{assigned}}}{V_{\text{true}}} \quad (3.48)$$

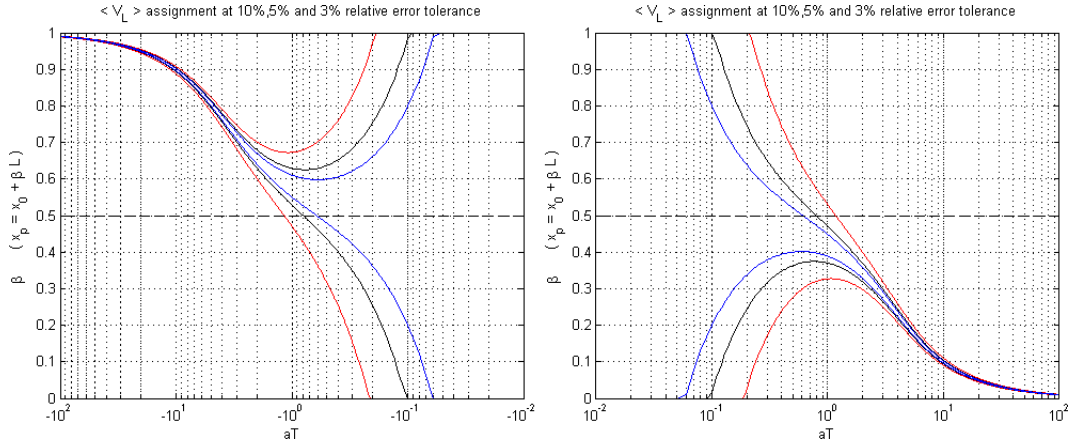


Fig. 3.5: Boundaries of the length fraction for different tolerances and for positive and negative local gradients

Proposition 3.3.3. *If the point of assignment of the $\frac{L}{T}$ ratio on the particle streak is $x_p = x_0 + \beta L$, then for $P\%$ relative error β is bounded by*

$$\frac{1}{\left(1 + \frac{P}{100}\right) aT} - \frac{1}{e^{aT} - 1} \leq \beta \leq \frac{1}{\left(1 - \frac{P}{100}\right) aT} - \frac{1}{e^{aT} - 1}$$

Proof. The relative velocity error for incorrect assignment is a function of the length fraction β and the aT product given by

$$e_r(\beta, aT) = \frac{V_E(x_p) - V_{\text{assigned}}}{V_E(x_p)} \quad (3.49)$$

The above expression can be simplified further as

$$e_r(\beta, aT) = \frac{a(x_0 + \beta L) + b - \frac{L}{T}}{a(x_0 + \beta L) + b} \quad (3.50)$$

$$e_r(\beta, aT) = \frac{(ax_0 + b) + a\beta L - \frac{L}{T}}{(ax_0 + b) + a\beta L} \quad (3.51)$$

Now using the expression for length we have $(ax_0 + b) = \frac{aL}{e^{aT}-1}$. So,

$$e_r(\beta, aT) = 1 - \frac{\frac{1}{aT}}{\beta + \frac{1}{e^{aT}-1}} \quad (3.52)$$

Since the relative error is bound by $P\%$, we have $|e_r| \leq \frac{P}{100}$. Then using the expression obtained for relative error we have

$$-\frac{P}{100} \leq 1 - \frac{\frac{1}{aT}}{\beta + \frac{1}{e^{aT}-1}} \leq \frac{P}{100}$$

which gives

$$\beta \leq \frac{1}{\left(1 - \frac{P}{100}\right) aT} - \frac{1}{e^{aT} - 1} \quad (3.53)$$

and

$$\beta \geq \frac{1}{\left(1 + \frac{P}{100}\right) aT} - \frac{1}{e^{aT} - 1} \quad (3.54)$$

From the last two inequalities, the result follows.

The boundaries between which the average Lagrangian velocity may be assigned over the length fraction (varying from 0 to 1) for different tolerances is shown in Fig. 3.5 for both positive and negative local velocity gradients. The span of possible assignment changes from all over the streak at near-zero gradient to an extremely well defined curve as the gradient increases. Fig. 3.6 gives a more magnified view showing the variation at smaller gradients.

3.3.5 Rule-of-thumb for quick assignment of average velocity

While accurate estimation of the aT product would lead to a precise assignment of the $\frac{L}{T}$ ratio, local estimation of $\frac{dL}{dx_0}$ (the variation of streak length with starting position) is more tractable during an actual experiment. Multiple experimental trials would lead to a range

$$p \in [P_1, P_2]; p = \frac{dL}{dx_0}$$

Now since $L = \left(x_0 + \frac{b}{a}\right)(e^{aT} - 1)$, we have

$$p = \frac{dL}{dx_0} = e^{aT} - 1 \quad (3.55)$$

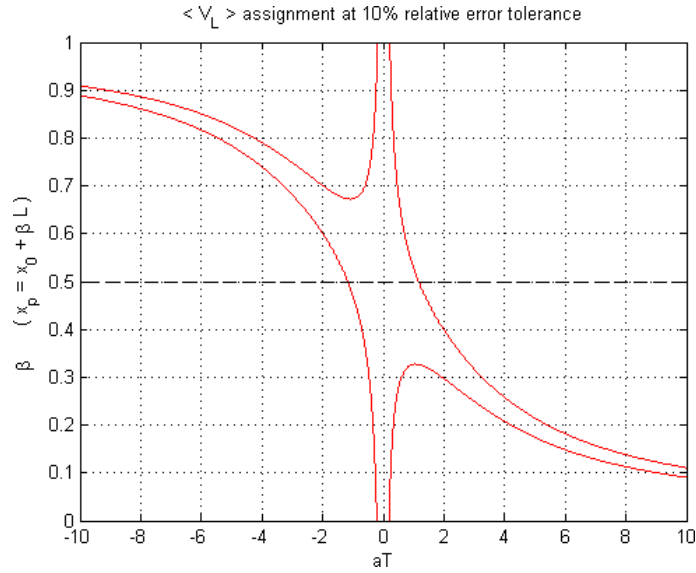


Fig. 3.6: Boundaries of the length fraction for 10% tolerance and for $|aT| \leq 10$

which gives

$$\hat{\alpha} = \frac{1}{\log(1+p)} - \frac{1}{p} \quad (3.56)$$

The values for β for different discrete intervals of the $\frac{dL}{dx_0}$ leading to an $e_r \leq 0.015$ are shown in Fig. 3.7 and in Fig. 3.8 a more continuous variation of β is sought after. The yellow highlighted region in the graph shows the assignment curve. Note that close to $p = 0$, the assignment region is the entire y -axis of the plot; i.e., anywhere on the streak.

Using (3.56) and different ranges of p across different values of the point of assignment β , we have the following equation that gives $e_r(\beta_p, aT) \leq 0.01$

$$\beta_p = -0.0002p^3 + 0.0041p^2 - 0.0403p + 0.4768 \quad (3.57)$$

3.4 STREAK-LENGTH DISTRIBUTIONS AND AFFINE TRANSFORMATIONS

The observed experimental variables have been treated as deterministic variables so far. In this section, we discuss the implication of random starting points. It may be noted that in an actual experiment, the starting point for the particle tracers cannot be assigned at exact

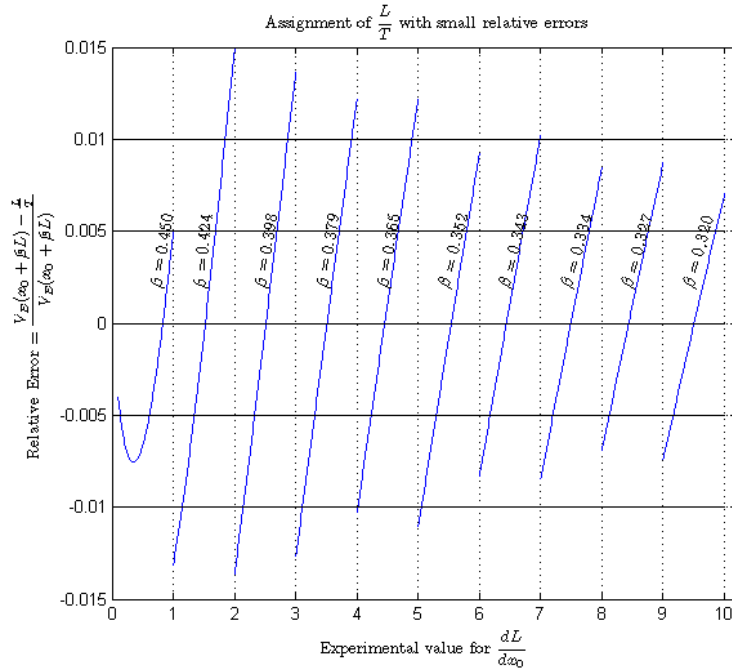


Fig. 3.7: β values for different experimentally determined ranges of p for $e_r \leq 0.015$

spatial locations. In most cases a bolus of tracers is released into the fluid stream. At the point of release, the particles are distributed in the microfluidic volume and their nature of their exact spatial distribution is unknown.

3.4.1 Particle position on streamlines as affine transformations

Consider now a tracer particle that has entered a microfluidic channel. From our earlier discussion on the characteristic curves in a velocity vector field, the particle immediately follows a streamline from the starting point to a final destination (after which we are not concerned). This streamline spans across the spatial Eulerian velocity field and the local velocity gradient keeps on changing as the particle position changes over the streamline. Fig. 3.9 shows this and divides the variable local gradient into short and distinct strips over which the local gradient is constant. This essentially is the local linear assumption.

Proposition 3.4.1. *For a first-order approximated time-invariant velocity vector field, the position of a particle (moving on a streamline) can always be expressed as an affine trans-*

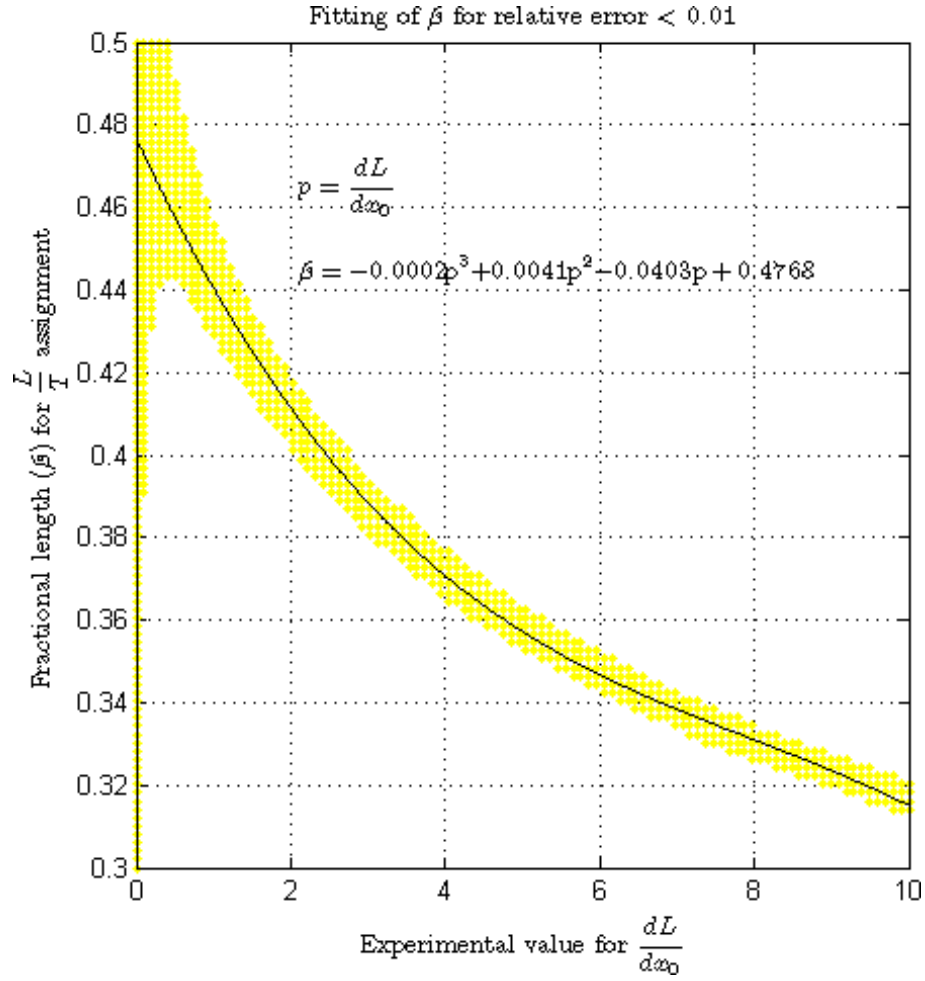


Fig. 3.8: β values for different values of p for $e_r \leq 0.01$

formation of the starting position and the constants of the transformation are functions of the local gradient (represented by 'a') and local offset velocities (represented by 'b').

Proof. From Fig. 3.9 and previously derived results, we have the following relationship for the first part of the complete path between the first start-point x_{i1} and the first end-point x_{f1} .

$$x_{f1} = x_{i1}e^{a_1T} + \frac{b_1}{a_1}(e^{a_1T} - 1) \quad (3.58)$$

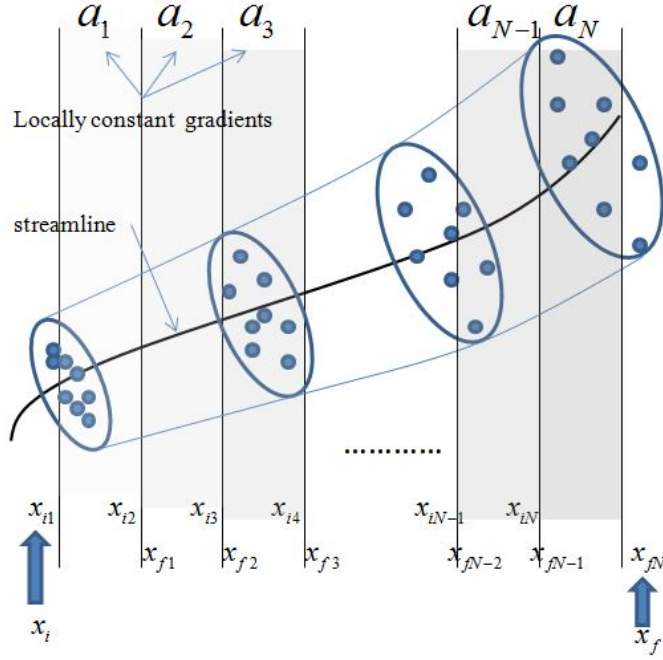


Fig. 3.9: Variation of particle position along a streamline across a velocity field

Similarly for the second start-point (first end-point) and the second end-point we have

$$\begin{aligned}
 x_{f2} &= x_{f1}e^{a_2T} + \frac{b_2}{a_2}(e^{a_2T} - 1); x_{f1} = x_{i2} \\
 x_{f2} &= \left[x_{i1}e^{a_1T} + \frac{b_1}{a_1}(e^{a_1T} - 1) \right] e^{a_2T} + \frac{b_2}{a_2}(e^{a_2T} - 1) \\
 x_{f2} &= x_{i1}e^{(a_1+a_2)T} + \frac{b_1}{a_1}(e^{a_1T} - 1)e^{a_2T} + \frac{b_2}{a_2}(e^{a_2T} - 1) \quad (3.59)
 \end{aligned}$$

The third part of the full path is then given by

$$x_{f3} = x_{i1}e^{(a_1+a_2+a_3)T} + \frac{b_1}{a_1}(e^{a_1T} - 1)e^{(a_2+a_3)T} + \frac{b_2}{a_2}(e^{a_2T} - 1)e^{a_3T} + \frac{b_3}{a_3}(e^{a_3T} - 1) \quad (3.60)$$

Generalizing, we have the following affine transformation

$$x_f = x_i \prod_{t=1}^N e^{a_t T} + \sum_{k=1}^N \frac{b_k}{a_k} (e^{a_k T} - 1) \prod_{j=k+1}^N e^{a_j T} \quad (3.61)$$

Or,

$$x_f = x_i P + Q; \left\{ \begin{array}{l} P = \prod_{t=1}^N e^{a_t T} \\ Q = \sum_{k=1}^N \frac{b_k}{a_k} (e^{a_k T} - 1) \prod_{j=k+1}^N e^{a_j T} \end{array} \right\} \quad (3.62)$$

The result follows.

3.4.2 Streak-lengths as an affine transformation of random starting points

From our previous discussion, we observe that the end-point of the particle streak is an affine transformation of the starting point. Now since the length is actually a difference between the end-point and start-point, the expression for the streak length L can also be expanded as an affine transformation of x_0 , the starting point. Now if the starting point x_0 is a random variable, then the length is also a random variable and is expressed as follows

$$L = Mx_0 + N; \left[\begin{array}{l} M = (e^{aT} - 1) \\ N = \frac{b}{a}(e^{aT} - 1) \end{array} \right] \quad (3.63)$$

For this particular case of a linear function of a random variable, the probability density function is given by

$$f_L(L) = \frac{1}{|M|} f_{x_0}(x_0) \left(\frac{L - N}{M} \right) \quad (3.64)$$

The expectation is given by

$$E[L] = ME[x_0] + N \quad (3.65)$$

and the variance is given by

$$Var[L] = M^2 Var[x_0] \quad (3.66)$$

It may be noted that the above expressions do not impose a constraint on the nature of the random variable.

3.4.3 Streak-lengths for uniformly distributed starting points

Generally the empirical distribution of all starting points of streaks does not well approximate a uniform distribution. However with sufficient data the starting point of streaks may

be resampled to obtain a uniform distribution; the pay off is an analytically tractable expression for streak length statistics. In such a case the starting point can be represented as

$$\tilde{x}_0 \sim U(x_p - L_{\min}, x_p) \quad (3.67)$$

An affine transformation for the uniform random variable then gives

$$\tilde{L} \sim U(M(x_p - L_{\min}) + N, Mx_p + N) \quad (3.68)$$

where the last equation is obtained using the previous expressions for M and N . We have then from the properties of the uniform distribution

$$E[\tilde{L}] = \frac{L_{\min} + L_{\max}}{2} = \left(x_p + \frac{b}{a}\right) \left(\frac{e^{aT} - e^{-aT}}{2}\right) = \left(x_p + \frac{b}{a}\right) \sinh(aT) \quad (3.69)$$

Similarly, for the variance of streak length we have

$$Var[\tilde{L}] = \frac{1}{3} \left(x_p + \frac{b}{a}\right)^2 [\cosh(aT) - 1]^2 \quad (3.70)$$

3.5 SPATIO-TEMPORAL AVERAGING OF STREAK LENGTHS

Spatio-temporal averaging involves the use of the average velocity obtained by dividing the streak length data with exposure time. This average velocity L/T is allocated to all the candidate pixels within the corresponding streaks spatial extent followed by a spatio-temporal averaging over each pixel through the entire stack of acquired frames. The working principle is illustrated in Fig. 3.10 below. Two frames are shown with streaks in overlapping spatial positions. The streak lengths are allocated to the spatial regions initially but then spatial averaging is done for the two frames which are part of a temporal sequence.

The actual averaging is done for multiple frames leading to a smooth transition at changes in the spatial velocity. While prior work using particle streak have used the local average Lagrangian velocity (L/T), the use of spatial averaging was not found in the context of microfluidic velocity estimation studies. Our analysis showed excellent tracking of the local velocity for small values of the aT product while for higher aT products, this leads to



Fig. 3.10: Spatio-temporal averaging of streak velocity fields.

over-estimation errors. To better understand the spatial averaging the following theoretical analysis was performed

Let us assume that x_0 is a continuous variable and L is a continuous function of this variable. The usual definition for the average value of a function within an interval (in this case spatial) gives us for an observation point x_p

$$V(x_p) = \frac{1}{T} \frac{\int_{x_p-L_{\min}}^{x_p} (x + \frac{b}{a})(e^{aT} - 1)dx}{\int_{x_p-L_{\min}}^{x_p} dx} \quad (3.71)$$

The above integral is solved as below

$$V(x_p) = \frac{1}{TL_{\min}} \int_{x_p-L_{\min}}^{x_p} (x + \frac{b}{a})(e^{aT} - 1)dx \quad (3.72)$$

to finally give

$$V(x_p) = (ax_p + b) \frac{(e^{aT} - e^{-aT})}{2aT} \quad (3.73)$$

In the previous equation the first term in brackets in the previous equation is $V(x_p)$ by definition of the first-order approximated velocity field. Hence we get

$$V(x_p) = V(x_p) \frac{(e^{aT} - e^{-aT})}{2aT} \quad (3.74)$$

As observed earlier, for small values the exponential-difference term reduces to $2aT$, otherwise it is a number more than $2aT$ and hence the over-estimation error.

3.6 ESTIMATION OF FIRST ORDER APPROXIMATION PARAMETERS

Estimation of the constants in the expressions relating the streak length L , the starting point x_0 and the exposure time T for a streak can be done statistically. Inherently this implies that the estimation procedure is dependent on the number of samples, and works better with more samples.

3.6.1 Estimation by robust regression

The expression for length can be expanded and written as

$$L = (e^{aT} - 1)x_0 + (e^{aT} - 1)\frac{b}{a}$$

If we let $M = e^{aT} - 1$ and $N = (e^{aT} - 1)\frac{b}{a}$ then multiple observations of (L, x_0, T) can be written as

$$\bar{L} = M\bar{x}_0 + N; \left[\begin{array}{l} M = (e^{aT} - 1) \\ N = \frac{b}{a}(e^{aT} - 1) \end{array} \right] \quad (3.75)$$

which can be solved robustly by the method of least-squares to yield

$$\hat{a} = \frac{1}{T} \log(1 + \widehat{M}); \quad b = \frac{\hat{a} \cdot \widehat{N}}{\widehat{M}} \quad (3.76)$$

Limiting solutions can be obtained for cases when the ‘ aT ’ product is small. For example for aT smaller than 0.1482 the relative error is less than 0.01. Also,

$$\bar{L} = M\bar{x}_0 + N; \left[\begin{array}{l} M = aT \\ N = bT \end{array} \right] \quad (3.77)$$

which gives

$$\hat{a} = \frac{\widehat{M}}{T}; \quad b = \frac{\widehat{N}}{T} \quad (3.78)$$

Finally, for uniform velocity ($a = 0$) we get

$$\bar{L} = bT \quad (3.79)$$

and hence

$$\hat{a} = 0; \quad b = \frac{L}{T} \quad (3.80)$$

3.6.2 Estimation based on maximum and minimum values

The maximum and minimum lengths of streaks under the first-order velocity field approximations can be used effectively to estimate the local gradient. For an actual experimental scenario with large number of observations it is very likely that the empirical maximum and minimum streak lengths approximate very well the corresponding true values at a particular position. From our previous results for the maximum and minimum values, we have,

$$\frac{L_{\max}}{L_{\min}} = \frac{(x_p + \frac{b}{a})(e^{aT} - 1)}{(x_p + \frac{b}{a})(1 - e^{-aT})} = e^{aT} \quad (3.81)$$

which gives

$$\hat{a} = \frac{1}{T} \log \left[\frac{L_{\max}}{L_{\min}} \right] \quad (3.82)$$

Using this value of a, b can be estimated as

$$\hat{b} = \frac{1}{T} \left(\frac{L_{\max} L_{\min}}{L_{\max} - L_{\min}} \right) \log \left[\frac{L_{\max}}{L_{\min}} \right] \quad (3.83)$$

While for a large number of experiments, the maximum and minimum values can be approximated by the sample array maximum and minimum values, for lesser number of experiments the following uniformly minimum-variance unbiased estimator or minimum-variance unbiased estimator (UMVUE or MVUE) can be used under the assumption of an uniform distribution of the streak-lengths. For large values of N , the estimates tend to their maximum-likelihood estimate.

$$\hat{L}_{\max} = \max[L] + \frac{1}{N} \max[L] \quad (3.84)$$

and

$$\hat{L}_{\min} = \min [L] - \frac{1}{N} \max [L] \quad (3.85)$$

Alternatively, we can also use the moment-based estimators for the maximum and minimum lengths, again with the assumption of the streak-length samples being uniformly distributed.

$$\hat{L}_{\max} = E [L] + \sqrt{3 \text{Var}[L]} \quad (3.86)$$

$$\hat{L}_{\min} = E [L] - \sqrt{3 \text{Var}[L]} \quad (3.87)$$

As in the case of robust estimation, it can be seen that large number of ‘observed’ streaks at a point would make the parameter estimation more accurate.

3.7 ON THE USE OF SECOND-ORDER APPROXIMATED LOCAL VELOCITY FIELD

In general second order approximation of a function provides higher fidelity than first-order approximation. However in the realm of microfluidics, the magnitude of the second order derivative of the local Eulerian velocity field is considered extremely small and has usually been neglected [60, 61], while deriving theoretical results as well as in practical settings for velocimetry purposes. Nevertheless, some treatment directed towards the computation of relative error between first and second order approximation is included here for completeness. Moreover, for the use of length-based particle streak velocimetry as proposed, we show that second order approximation leads to solving of an indeterminate system of non-linear equations.

An ideal scenario is considered where both first-order and second-order approximations are used, for comparison purposes. Then for the velocity around a point $x = x_p$ for a window of observation of width h , the first-order approximation gives

$$V_E(x_p + h) = V_E(x_p) + Jh; \quad J = \nabla V_E(x) \quad (3.88)$$

and second order approximation gives

$$V_E(x_p + h) = V_E(x_p) + Jh + H \frac{h^2}{2}; \quad H = \nabla^2 V_E(x) \quad (3.89)$$

where J and H are the first and second order derivatives respectively. While considering all the 3 components together, these would be the Jacobian and the Hessian matrices for the velocity field. From the above two expressions, for the case of ideal parameter estimation, the relative error for the first-order approximation would be given by

$$e_r = \frac{H \frac{h^2}{2}}{V_E(x_p) + Jh + H \frac{h^2}{2}} = \frac{1}{1 + \frac{2}{h^2} \left[\frac{V_E(x_p)}{H} \right] + \frac{2}{h} \left[\frac{J}{H} \right]} \quad (3.90)$$

In the above expression the relative error increases with increase with the width of the observation window which in turn is dependent on the length of the streaks observed for an exposure time T . The values of H and J are fixed for the position of observation $x = x_p$ and the velocity field. Hence the relative error is bounded by the maximum size of the window as

$$e_r < \frac{1}{1 + \frac{2}{h_{\max}^2} \left[\frac{V_E(x_p)}{H} \right] + \frac{2}{h_{\max}} \left[\frac{J}{H} \right]} \quad (3.91)$$

where h_{\max} is the maximum width of the observation window possible at $x = x_p$. Now from Fig. 3.11, we observe that the maximum width of the observation window is equal to the length of the shortest and the longest streak that is possible. Now using the maximum velocity of the streak in this observation window, we get,

$$h_{\max} < \max [V_E(x)]_w 2T \quad (3.92)$$

Hence, for an arbitrary velocity field, the relative error in considering a first-order approximation and not a second-order approximation is bounded by

$$e_r(x_p) < \frac{1}{1 + \frac{2}{h_{\max}^2} \left[\frac{V_E(x_p)}{H} \right] + \frac{2}{h_{\max}} \left[\frac{J}{H} \right]}; h_{\max} = \max [V_E(x)]_w 2T \quad (3.93)$$

It may be noted however, that the maximum window width has only been approximated above; for a known velocity field, more accurate expressions can be obtained. The case of a 1-D velocity field that is exponential and has the form $V_E(x) = be^{ax}$ for the local Eulerian velocity, is considered as an example. By solving the ODE from the velocity expression, we can obtain the length of the streaks by the same procedure as earlier. The expressions

for the minimum and maximum streak lengths are shown in Fig. 7.16. in Chapter 7 of this dissertation. The maximum width for the observation window is $h_{\max} < L_{\min} + L_{\max}$, which gives

$$h_{\max} < \frac{1}{a} \log \left[\frac{1 + abTe^{ax_p}}{1 - abTe^{ax_p}} \right] \quad (3.94)$$

Moreover, the values of J and H in the relative error expression are

$$J = V'_E(x_p) = abe^{ax_p} = aV_E(x_p)$$

and

$$H = V''_E(x_p) = a^2be^{ax_p} = a^2V_E(x_p)$$

respectively. From these values, the bound on the relative error can be accurately expressed in terms of the parameters of the known Eulerian velocity field.

The actual use of a second-order velocity field is now considered. The local Eulerian velocity, can be expressed as $V_E(x) = cx^2 + ax + b$ The differential equation that needs to be solved for the path equation is thus

$$\frac{dx}{dt} = cx^2 + ax + b$$

Now taking integrals on both sides with the usual limits

$$\int_{x_0}^{x_0+L} \frac{dx}{cx^2 + ax + b} = \int_0^T dt \quad (3.95)$$

The solution to the similar indefinite integral is

$$\int \frac{1}{cx^2 + ax + b} dx = \begin{cases} \frac{2}{\sqrt{4bc-a^2}} \arctan \frac{2cx+a}{\sqrt{4bc-a^2}} + C; 4bc - a^2 > 0 \\ \frac{1}{\sqrt{a^2-4bc}} \ln \left| \frac{2cx+a-\sqrt{a^2-4bc}}{2cx+a+\sqrt{a^2-4bc}} \right| + C; 4bc - a^2 < 0 \\ -\frac{2}{2cx+a} + C; 4bc - a^2 = 0 \end{cases} \quad (3.96)$$

If it is assumed that the magnitude of c is extremely small for microfluidics, such that $4bc - a^2 < 0$, then we have

$$\left[\frac{1}{\sqrt{a^2-4bc}} \ln \left| \frac{2cx+a-\sqrt{a^2-4bc}}{2cx+a+\sqrt{a^2-4bc}} \right| \right]_{x_0}^{x_0+L} = T$$

which can be solved to obtain

$$L = \frac{e^{\sqrt{a^2-4bc}T}}{2c \left\{ \frac{1}{2cx_0+a+\sqrt{a^2-4bc}} - \frac{1}{2cx_0+a-\sqrt{a^2-4bc}} e^{\sqrt{a^2-4bc}T} \right\}} \quad (3.97)$$

As can be observed, L is some function of x_0, T, a, b, c where only the particle streak length L and the starting point x_0 can be measured. The measurement is to be done at a point of observation in the spatial extent of the microfluidics device. However there are 3 unknown variables which need to be estimated. Note that the exposure time T cannot be considered a variable since it cannot be changed multiple times at every spatial location, due to hardware constraints. Consequently, the second order approximation would lead to an indeterminate system of non-linear equations with respect to the different measurements that we can practically obtain.

3.8 GENERATION OF 2D FIELD COMPONENTS

In the previous section the first-order approximation of the parameters were obtained. If it is assumed that a group of streaks $x_0 \in [x_{01}, x_{02}]$, $L \in [L_1, L_2]$ is analyzed then the spatial extent of validity for \hat{a}, \hat{b} is $x \in [x_{01}, x_{02} + L_2]$ and we assign

$$V(x) = \hat{a}(x - x_{01}) + \hat{b} : x \in [x_{01}, x_{02} + L_2]$$

Note that for a position x , $V(x)$ can be obtained from multiple instantiations of x_p ; i.e.,

$$V(x) = \hat{a}(x_p)(x - x_i) + \hat{b}(x_p)$$

All the values of $V(x)$ thus obtained are averaged for that particular spatial position and thus the final velocity estimate is obtained as a spatio-temporal statistic. The method is further explained with Fig 3.11. Consider the velocity for the pixel in the center. It would observe 3 categories of streaks; ones that start, ones that end and ones that just pass over. These streaks can now be used to obtain a velocity estimate for this pixel in the center and nearby pixels within the window of analysis. Note that while getting the estimate we would resolve and find the estimates separately for the horizontal and vertical components. Now consider the very next adjacent (horizontal direction) pixel. While considering this

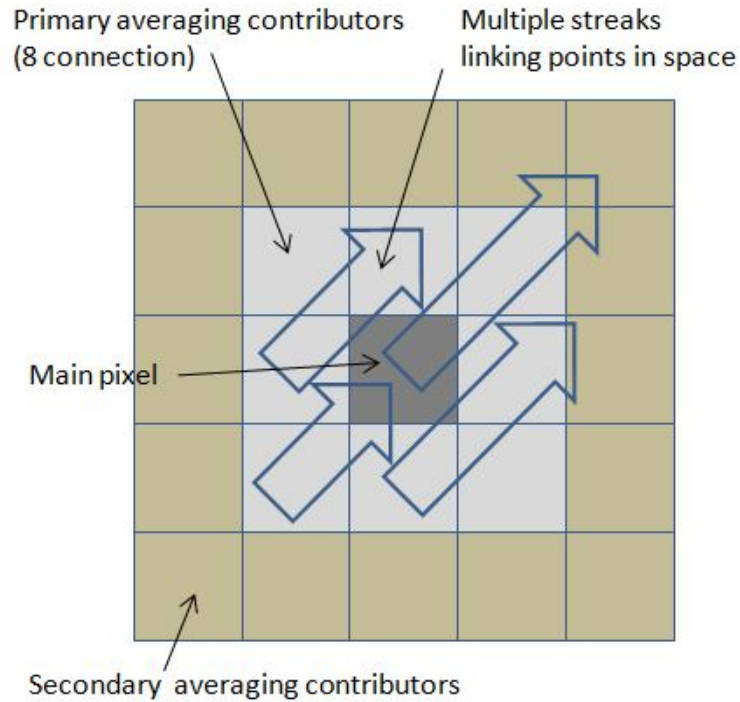


Fig. 3.11: Spatio-temporal averaging of streak velocity fields.

pixel and the streaks it observes, and finding the velocity estimates, the previous pixel also falls into the window of analysis and the velocity parameter estimates are utilized to obtain velocity for both these pixels again. All these velocity estimates are averaged in the end, resulting in a smooth 2-D field (from the 2 components). Indirectly, the averaging gets us closer to a second order correct spatial velocity estimation.

The performance of this method was found to be excellent for large numbers of contributing streaks. Smoothness of the velocity surface so obtained can be further improved and missing-data problems corrected, by surface fitting and other interpolation methods. Details for these methods and their performance will be studied in future and not covered in this dissertation.

CHAPTER 4

EXPERIMENTAL CONSIDERATIONS

The μPSV analysis methods described in Chapter 3 are targeted towards everyday laboratory velocimetry requirements. The hardware relaxation enables the user to obtain experimental data with minimum cost and effort. While the actual data acquisition steps are quite similar to μPIV , some adjustments need to be made and some points need to be kept in mind to ensure high quality streak data. Note that a high quality μPIV setup would definitely give high quality streak data (provided the exposure time can be controlled) but this expense is not mandatory and this was one of the stronger motivations for this work. As mentioned earlier, the analysis methods developed in this work use a data table which contains streak descriptors (start and end points) for multiple streaks at the same spatial locations, the data being obtained from multiple frames. Hence experimental considerations that lead to accurate streak descriptors are important.

We first delineate the expectations for an ideal streak image and what are the standard deviations. To visually elaborate, Fig. 4.1 shows the common possibilities that the image processing algorithm might encounter in order to construct the spatio-temporal streak descriptor table. The first is the image of a tracer particle, ideally this should be a circular pattern and can be obtained in a region where the tracer particle is static and does not experience any resultant force. The second image is that of an ideal streak, with the end parts resembling semicircles and having a width equal to the static particle image diameter. The next few images show different possibilities of obtaining images with overlap and defocussing errors. As can be seen, in the overlapping errors, the streaks would have to be extremely close in the vertical axis of imaging. Only then would their imaged sizes would be similar enough to cause confusion. In the case of defocussing errors (shown last), the overlapping streaks would vary considerably in size. It may be noted that since the proposed method depends entirely on the streak length and the starting position, the ultimate goal of the experimental data acquisition is to obtain clear, distinct streaks with discernible boundaries.







Single particle image	
Single particle streak	
Streak overlap type 1 – unidirectional	
More general streak overlap – both horizontal and vertical directions	
Defocused particle in background	
Defocused streak in background	

Fig. 4.1: Particle image cases: ideal tracer, ideal streak, overlapped streaks and defocused, overlapped streaks

4.1 MICROFLUIDIC DEVICE DESIGN

Device design plays a big role in the acquisition of experimental data. A poorly constructed device is almost certain to generate poor quality data, leading to a huge requirement on the preprocessing of images and often resulting in poor velocimetry estimates. Note that this is a consideration that cannot be altered once the experiment has started.

4.1.1 Channel depth and surface uniformity

The channel depth of a microfluidic channel is an important factor. A classic concern would be the case when the channel depth is not sufficient for the tracer particles to pass freely, leading to erroneous inferences from the captured image data. As a principle, the channel depth (or diameter) should be at least an order of magnitude larger than the particle size so that no size effects occur. Another important concern is the nature of the walls of the channel. For best results, the inner surfaces of the channels should be as uniform as possible and preferably coated with a substance that reduces the surface adsorption and adhesion

of tracer particles. Alternatively, tracer particles can be coated, thus reducing adhesion. An example of this would be the use of particles coated with polyethylene glycol (PEG). Channels that can be reused (e.g., glass channels) should be rinsed and cleaned after every experiment. An ultrasound bath can be used to remove tracers attached to the walls.

4.2 EXPERIMENTAL SETUP

Experimental setup is another consideration that cannot be altered during the image capture process. Hence the following points need to be carefully planned to reduce experimental re-runs. The inverted microscope forms the main component for our experimental setup and a schematic of the microscope model that was used is shown in Fig. 4.2.

4.2.1 *Illumination and fluorescence imaging*

Volume illumination was used for our experiment using the lamp attached to the microscope. A pulsed light source is not required as we do not need high-speed synchronised imaging. However, the use of a pulsed source can help reduce the directional ambiguity as suggested by Adrian [6]. The light source intensity should be controllable to easily optimize the image intensity below the saturation level. While our analysis is not directly dependent on the intensity of the streak images, increasing the light intensity or the gain beyond the CCD maximum bit levels increases the background noise and in the bleaching of the fluorescent dye which eventually reduces the SNR, leading to erroneous velocity estimation.

Fluorescence imaging was used for our experiments and is strongly suggested for the use of μPSV . This is because light from the fluorescent tracer particle is the main source of the image that is formed on the camera sensor and a large volume of illumination originating from the walls and other non-fluorescence disturbances is blocked by the optical filter tuned to the fluorescence emission wavelength.

4.2.2 *Tracer particle features*

Ideal tracers are identical spherical volumes with no inertial drag, surface adhesion, temperature effects and chemical effects. In practice this is not possible. So we need to select

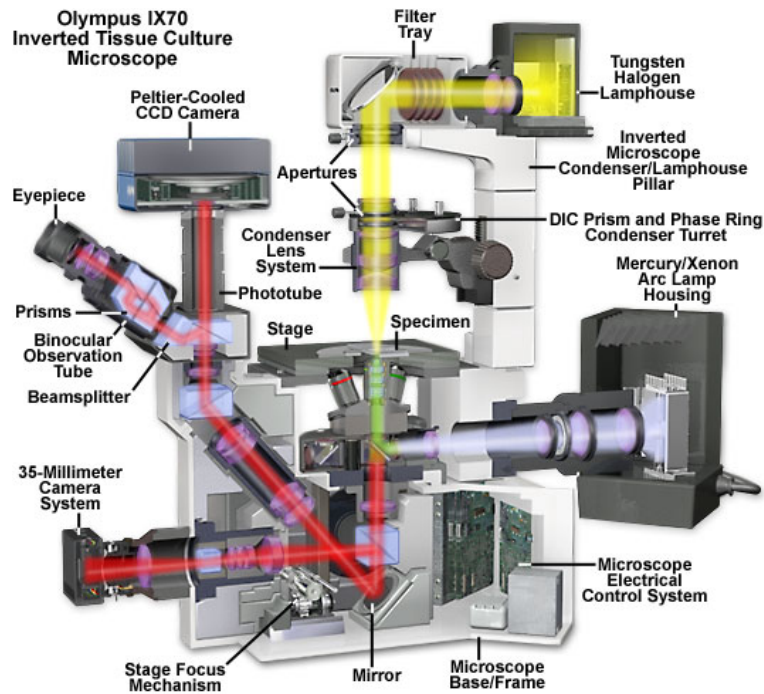


Fig. 4.2: Schematic of an inverted microscope (Olympus IX70)

tracer particles that are uniform in size (minimal deviation in diameter), mono-disperse, and have an optimal particle image diameter. Particle sizes between 500 to 1500 nm usually offer a good compromise between visibility and flow fidelity [3]. Colored tracers can be very useful, especially when the region of observation can be distinctly segregated into different velocity zones. Intelligent choice of surface charge and particle size can then get excellent estimation results; e.g., for electrophoresis and di-electrophoresis studies. Another way by which tracers of multiple colors can be useful is in the correction of overlap errors. For example an unidirectional overlap of three streaks of identical particle size but different colors can be easily resolved by filtering the image into different color components.

4.2.3 Seeding density

There is a distinct need to avoid high seeding density to reduce streak overlaps. Moreover, a high seeding density would bring undesired problems of higher background noise and particle clustering. The preferred alternative is to increase the particle count virtually by

using more images, similar to the correlation averaging technique [16].

4.2.4 Numerical aperture for the optics

Lenses with high NA and planar correction should be used for the objective. High quality objectives turn out to be the most cost-efficient way for improved image quality. The final (static) particle image diameter should span at least 3 pixels. This is necessary so that sub-pixel accuracy can be achieved. Since recommended particle size varies between 0.5 to 1.5 μm [3], the effective image pixel size should be less than 2 μm . Note that in this streak based method the accuracy is strongly dependent on the pixel resolution and smaller image pixel size delivers more accurate estimates.

4.3 IMAGE ACQUISITION SETUP

The image acquisition setup is usually coupled to the microscope system and can be controlled in real-time using dedicated software. For some image capture devices, it may even be possible to automatically change certain parameters by the use of programs.

4.3.1 Exposure time

The usefulness of the exposure time control has been discussed earlier. The minimum exposure time should be such that it creates a well resolved particle streak at the region of lowest local velocity in the microfluidic device. The upper limit of the exposure time is set by the amount of overlapping that might occur or by the amount a particle streak gets cut-off at the boundaries of the ROI being imaged. Note that a very large exposure time would reduce the frame rate considerably, resulting in longer image acquisition times.

4.3.2 Frame rate

Frame rate and exposure time are related and is shown in the following simplified expression:

$$r_f = \frac{1}{t_{\text{acq}} + t_{\text{read}}} = \frac{1}{t_{\text{CCD}} + t_{\text{shutter}} + t_{\text{exp}}}$$

Setting a large frame rate makes the image acquisition process short. Moreover for a fixed exposure time, an increase in frame rate implies that streaks from the same particle in consecutive images are closer together. Often this helps with more sophisticated velocimetry

that requires inter-frame streak association. Note that for the proposed streak based method, the upper bound on the frame rate is set by the smallest exposure time that can be used and still lead to a well resolved streak. This in turn gets decided by the image resolution and the local velocity in the experimental setup.

4.4 NUMBER OF FRAMES

Our proposed method is statistical one and strongly relies on a large number of streak images being observed at each point in the ROI. Note that there is no constraint on the starting points of streaks, although a uniform distribution of starting points (obtained over time) would make the statistical strength of the estimation process uniform across the ROI. For estimation of steady state particle velocity, we do not need to restrict ourselves to only a small number of images. Consequently, a large number of images acquired for a steady flow would greatly help the velocity estimation process.

4.5 DISTORTION EFFECTS AND MITIGATION STRATEGIES

The problem of defocussing cannot be eliminated without the use of laser-sheet based illumination and (or) confocal microscopy, so as to constrain the depth of focus. Overlap of streaks, on the other hand cannot be eliminated unless the seeding density is drastically reduced. However, statistical and image processing methods in conjunction with some knowledge of the velocity field can successfully mitigate these problems.

4.5.1 Overlap of particle streak images

Streaks in different layers can also get sharply imaged together, particularly when the channel depth is small. In this case, erroneous lengths (longer) can bias the local length distribution (due to the mixing of lengths at different depths). But with a large dataset, the mean, median and standard deviation can be used to eliminate most outliers. It may also be noted that unless there is a considerable velocity gradient among immediately adjacent depth layers, the variance of the distribution of streak-length-error introduced at a particular focal plane would be small. This is typically true if the functional properties of the microfluidic channel are somewhat uniform across the depth.

4.5.2 Defocussing of particle streak images

Unlike μPIV , our method is based on shape and not cluster pattern and intensity. Accordingly, the defocusing problems are different than the known depth-of-correlation problem encountered in μPIV [13]. For deeper channels, defocussed streaks over and below the focal plane often get imaged. These are eliminated during morphological processing which is based on the image diameter of a static tracer particle (recorded separately) in focus. Streaks which are much “thicker” get eliminated. This is only possible since streaks have a shape and a thickness determined by the particle image diameter. Moreover, the intensity loss due to defocusing is used effectively in the local adaptive thresholding (selecting the highest intensity streak to choose in-focus streaks and eliminate out-of-focus streaks).

CHAPTER 5

IMAGE PROCESSING FOR PARTICLE STREAK FEATURE ESTIMATION

In Chapter 3, it was shown that it is possible in theory, to obtain the parameters of the velocity field under a local linear approximation with the use of the spatial starting points of all the streaks that are observed at a location and the lengths of these streaks. Hence, the image processing algorithm that precedes this stage (of parameter estimation) is expected to generate as output a table with these required values. The image processing required to convert a set of image frames containing particle streaks to data tables that contain the start and end locations of particle streaks is discussed in this chapter. Moreover we also briefly discuss the use of these tables and the errors that are usually encountered.

5.1 FORMATION OF THE PARTICLE STREAK IMAGE AND STREAK FEATURES

Particle streaks are motion blur effects from isolated particles. Due to the extended time of exposure, every tracer particle forms a trajectory within the focal plane. The corresponding image is created in the image plane (e.g., CCD array) and the image formed includes the effects due the optics. The Lagrangian representations are

$$\begin{aligned}\xi &= \xi(x_0, t - t_0) \\ V_L(x_0, t) &= \frac{\partial \xi(x_0, t - t_0)}{\partial t}\end{aligned}\tag{5.1}$$

In the case of uniform motion the motion blur impulse response has a simple closed form expression. For example in the case of an ideal streak caused by a particle moving at constant velocity V with an angle of ϕ with the horizontal axis during an exposure time T is given by

$$h(x, y) = \begin{cases} \frac{1}{VT} & ; 0 \leq |x| \leq L \cos \phi; y = L \sin \phi \\ 0 & ; otherwise \end{cases}$$

Similarly expressions for uniformly time accelerated motion can be derived for case where $\frac{d^2 \xi(x_0, t - t_0)}{dt^2}$ is a constant for the given time interval. However, more often than not the acceleration is non-uniform both in the Lagrangian and Eulerian representations and is unknown. So although simpler descriptors for the streak formation process are possible for an

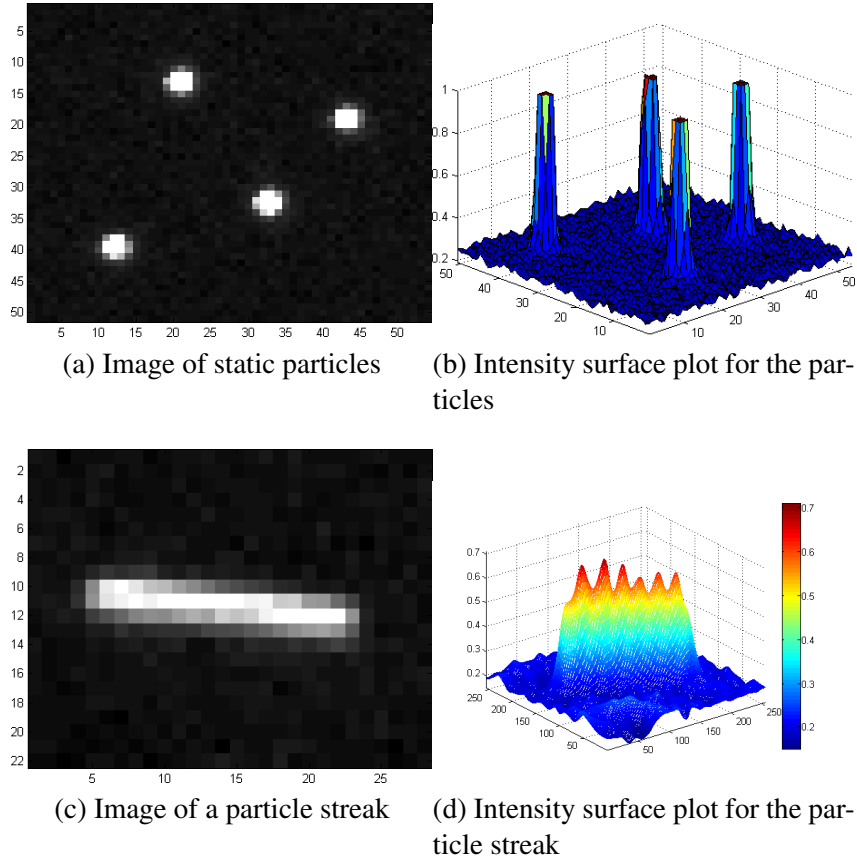


Fig. 5.1: Static particles, particle streaks and their intensity surface plots

ideal point particle undergoing uniform motion, for velocity field estimation in experimental devices, this information cannot be used easily.

Fig. 5.1 shows images of static particles and particle streaks in the image plane and a 3-D representation (surface plot) with the pixel intensity as the third axis. Note that the surface plot of the particles shows clipping due to saturation. An important observation is that in the ideal case of zero defocusing, the motion blur effect creates a particle streak whose width is identical to the diameter of the static tracer particle image. During the experiment, the sharpest images are obtained at the focal plane and objects above or below are defocused. Consequently, such particles and streaks have a higher diameter and width than images obtained in the focal plane. Hence information about the image diameter for static particles is extremely important. In most of our experiments, the static particle image

diameter is around 5 pixels. If we consider carefully the bounding box method, we find that the corners of the streak and the corner of the box touch each other. Assuming that the center of the blob placed at the corner of the same bounding box and the center of the particle forming the streak is at x_0 , a correction needs to be made for the particle diameter extent. This is done in our streak length processing.

For the proposed method, the intensity variation over the spatial extent of the streak is not directly utilized for the final velocity computation. Some particle streak tracking based velocimetry algorithms however use this kind of information and can be found in the works of Rosenstiel [36] and Hering [30]. Hence the most important particle streak feature information required for the proposed method are the end-points of the particle streak. Note that the image analysis algorithm actually does not matter as long as these features are obtained. A streak sketch in 2-dimensions with its descriptors is shown in Fig. 5.2. The streak is isolated by a bounding box and a straight streak is assumed. The starting point and the length are the two most important outputs from the streak detection phase.

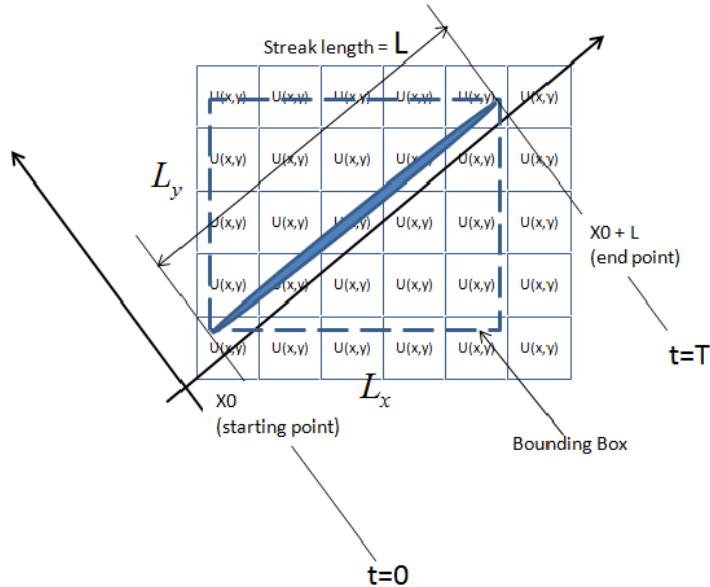


Fig. 5.2: An ideal streak with its bounding box

5.2 IMAGE PROCESSING OF PARTICLE STREAKS

Image processing for the particle streaks uses some basic computer vision procedures employed for object tracking and motion estimation. There are multiple ways in which these procedures could be implemented and no claims of quantitative superiority is made for the standard methods used here.

5.2.1 *Some basic concepts and methods*

The basic methods employed for the processing of particle streaks include local thresholding (for object detection), finding the bounding box and the local orientation (object tracking) and block matching (motion estimation).

Bounding box

The bounding box is an imaginary rectangle that tightly encloses a foreground object in the image plane. The straight lines that make this box are the of the form $y = MINROW$ and $y = MAXROW$ in the vertical direction and $x = MINCOL$ and $x = MAXCOL$, where the constant values on the RHS are the minimum and maximum row and columns for which there exists a pixel that belongs to the particle streak. Hence, the thresholding procedure immediately helps define the bounding box.

Local orientation

Local orientation here refers to finding the direction within the bounding box of the streak in which there is continuous chain of high intensity pixels. So effectively, the spatial extent of the streak is traversed along the longer diagonal of the bounding box. Note that the usual definition of local orientation has been simplified and is obtained for a binary image area and not for a intensity variation. Accordingly, calculation of 2-D image gradients is not required. Detailed description of local orientation methods can be found in the works of Jahne [62] and Nordberg [63]. For our case a Radon transform [64, 65] is sufficient and provides a method to automatically confirm which diagonal of the bounding box rectangle encounters a higher number of 'ON' pixels.

Local thresholding

Local thresholding helps reveal the foreground objects compared to the background image plane. For high quality imaging, global thresholding is sufficient, but local thresholding is more effective in our case where all the particles being imaged may not be in the exact focal plane depth. In such a case, these objects would have a different range of intensity values for their images. It was found that a multilevel thresholding algorithm works best for our purpose. Further details on thresholding can be found in standard image processing textbooks [66, 67] and review articles [68].

Block matching

A block matching algorithm (BMA) locates matching blocks in an image sequence, and between consecutive frames for our purpose. Knowledge of the temporal order and the location of a matching block provides the information of the motion vector in the region of interest. A discussion on the major BMA's can be found in literature [69, 70] but for our purpose a vectorized extensive search was used, since the search neighbourhood selected was quite small.

5.2.2 *The processing algorithm*

The processing algorithm has several image processing stages. All these stages however are well known in image processing literature individually and multiple implementations exist that can perform the requirements for each stage. Hence, in this section we discuss the relevant processing logic with respect to our goal and not the details of each sub-process. The image processing code was written in Matlab (Mathworks, Inc.)

Fig. 5.3 illustrates together an actual experiment, an acquired image from the experiment, a streak from the image and the bounding box around this streak obtained during the image processing. The width W and the height H of the box would naively represent the exposure time-weighted local horizontal and vertical velocity components respectively. The figure also shows the presence of particles stuck to the channel floor. Note that these

particles would create regions of consistent high intensity in the images, by aggregating through the temporal stack.

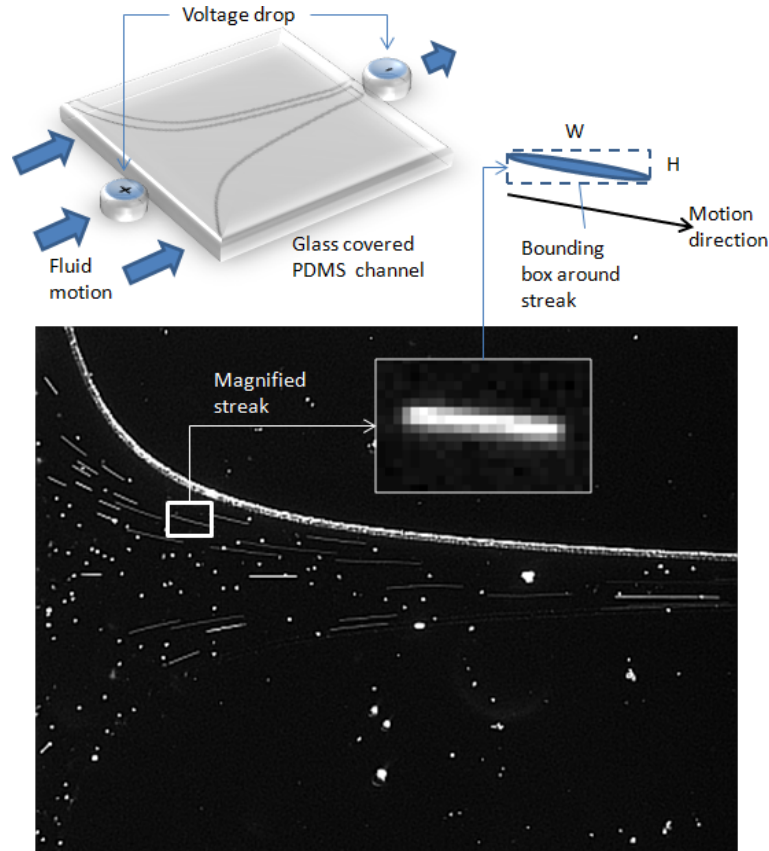


Fig. 5.3: An experimental setup showing schematic, particle streaks and bounding box

Algorithm description

The processing algorithm was made to accommodate both experimentally obtained particle streak images and those obtained by simulation, the only difference being the absence of the preprocessing stage for the simulated images as they are free from background noise, defocussed streaks and images of tracer particles stuck to the channel floor. In contrast, because of these artefacts, the pre-processing stage is very important for actual experimental images, as is the quality of the images themselves. For better performance, the experimental process should incorporate strategies such that the image acquisition process is efficient and this has been discussed in some detail in the Chapter 4. Fig. 5.4 shows the image processing

stages. The main steps are shown connected by arrows and the sub-steps are shown below each of the main steps. The blocks on the extreme RHS are particular techniques that were used and can be replaced by other methods if required.

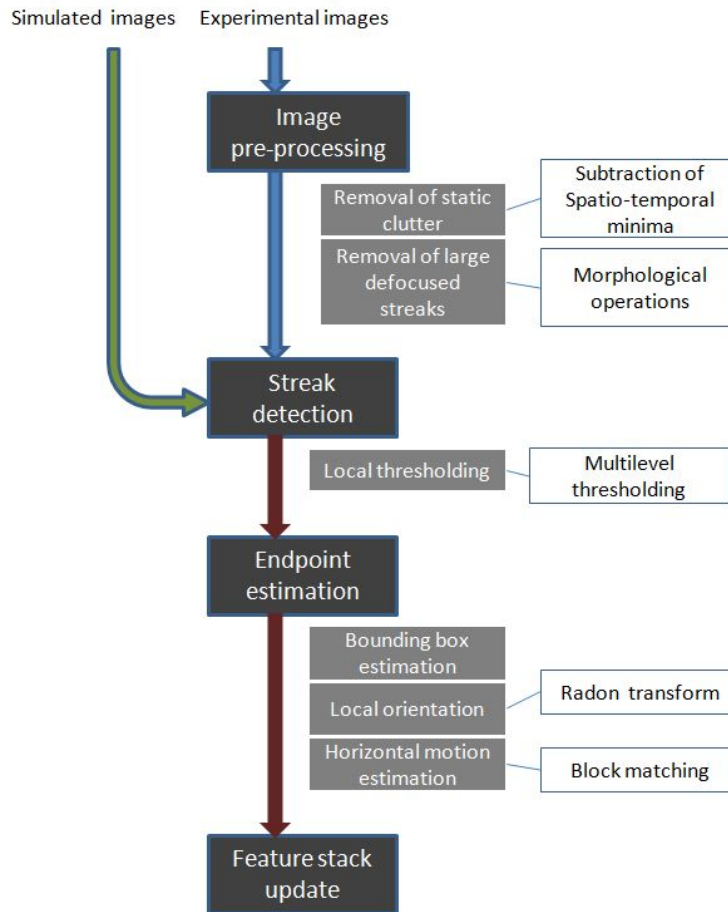


Fig. 5.4: The streak image processing algorithm

The preprocessing stage reduces the noise and eliminates spatially constant distortions. Spatially constant distortions are removed by obtaining temporal statistics (minimum pixel value for each pixel across the image stack). The spatial instrument noise is reduced by 2-D spatial noise reduction algorithms. While obtaining the temporal statistics, the maximum intensity projection (MIP) is also found to identify the spatial coverage and flow pattern. For a large number of image frames, streaks would be found at all places where

the flow occurs and thus the MIP image can be used to obtain a region-of-interest for which particle flow occurs. Also by performing an image sum operation through the stack we obtain the region of coverage as a frequency map describing how often a streak might be observed at a pixel. Regions (and pixels) that have poor coverage and frequency of streaks can be masked to reduce computational expense.

The streaks are detected by thresholding. A simple global thresholding is used for simulated images while an adaptive multilevel thresholding is used for actual experimental images. Defocussed streaks can be removed by a combination of morphological operations and multilevel thresholding, where the multilevel thresholding detects the defocussed image and can be subtracted in the image domain, while a proper selection of structuring element based on the static particle image diameter can be used to retain focussed streaks.

After the streak is detected, the bounding box is first obtained. The corners of the bounding box represent the endpoints of the streak, but prior to that the endpoints are corrected for the diameter of the particle image. Note that there is an ambiguity about which diagonal corner is the starting point and is resolved by the local orientation and the computation of only the horizontal component of the motion vector. This is further discussed later in this section. Once the endpoints are obtained, we know the starting point

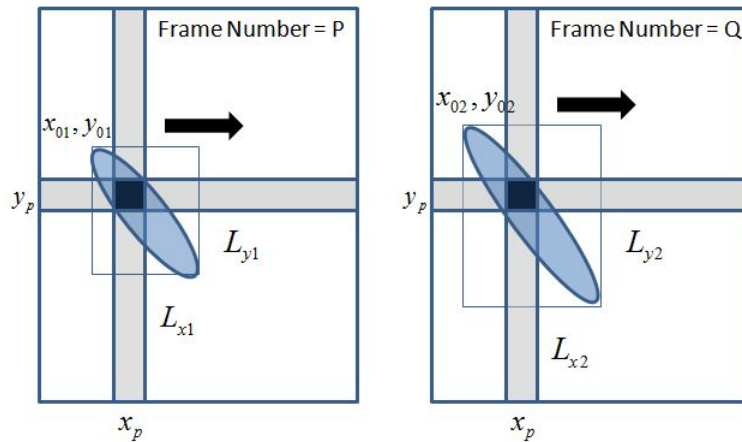


Fig. 5.5: Obtaining the position and length stacks

of the streak and the particle streak length. This is updated in the position and length feature

databases (stacks). The process is further illustrated by Fig. 5.5. The images represent two arbitrary frames in an acquired image sequence where a streak is observed at position x_p, y_p for both the frames P and Q. The corresponding starting points, and bounding box lengths are also shown in the figure. Thus, from these two frames, the position x_p, y_p is updated in four different databases at two positions in the temporal direction. When all the acquired image frames are processed, the generation of the streak feature database is also complete.

Resolving directional ambiguity

The directional ambiguity for streaks can be removed by either using hardware [71, 72] or by the use of image processing based motion estimation techniques. The exact requirement here is to identify the corner in the bounding box where the particle streak originates. For this we first need to identify the diagonal of the rectangle which contains the maximum number of streak image pixels. This is done by finding the local orientation as discussed earlier. Once we know the diagonal, information about the sign of the horizontal component is sufficient to resolve the directional ambiguity. This is done in the following way. An MIP image is generated from about 10 randomly selected image frames from the image stack and another MIP image is generated by taking next immediate frames for each of the frames. Then, a small neighbourhood is selected in the center of the bounding box for the first MIP image and this is searched for the best horizontal block match in the other MIP image. The direction of the best match gives the sign of the horizontal motion vector. Fig. 5.6 shows the use of the orientation and X-component sign information to identify the corner of the bounding box where starting point is located.

5.3 STREAK FEATURE DATABASE AND THE LOCAL LENGTH VARIATION TABLE

The streak feature database is similar to an image stack and in pixel space, occupies the same volume as all the acquired images put in a stack. The order of the frames in the database does not matter after its generation, but during the image processing the time sequence is important for the block matching algorithm. A block diagram of the database is shown in Fig. 5.7. Only the horizontal component is shown here, but the vertical component

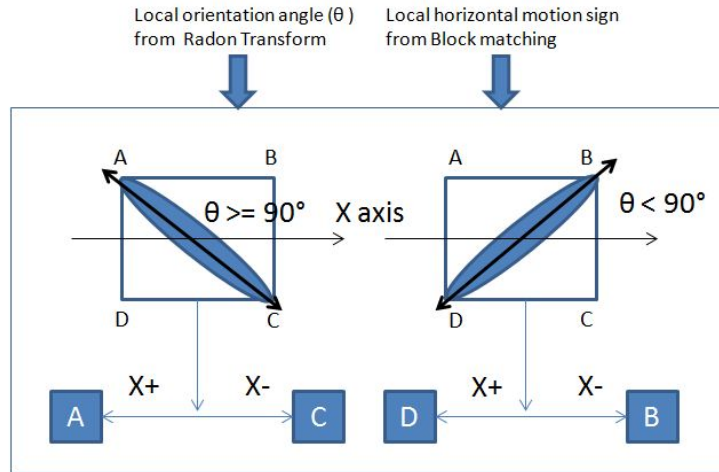


Fig. 5.6: Resolving directional ambiguity

yields similar stacks. Considering again the position x_p, y_p and looking through-the-stack, there would be some frames where that position has a value and many more where the value is zero depending on spatial extent of the streaks in different frames. Considering the collective values as 1-D arrays, four such arrays are obtained, two each for the length and the streak starting positions. Now arranging them side-by-side we get a table of all the lengths and the streak starting positions. This table always has more zeros than non-zero values since the number of streaks seen at a point is much smaller than the total number of frames. Hence the zero valued rows are removed and the table length columns are sorted in ascending order of starting position to get the local length variation table. Note that the lengths are signed and are thus positional displacement vectors. An example of the local length variation table is shown in Fig. 5.8.

The local length variation table can be directly used for estimating the local velocity by either the spatio-temporal averaging method or by the local linear approximation method as shown in Fig. 5.9. The sorting process described earlier actually helps in eliminating large outliers even before the data is used for robust linear fitting. Note that in the ideal case of a smooth field with small spatial gradient, the streak lengths would monotonically increase or decrease when the starting position increases. This is because for this

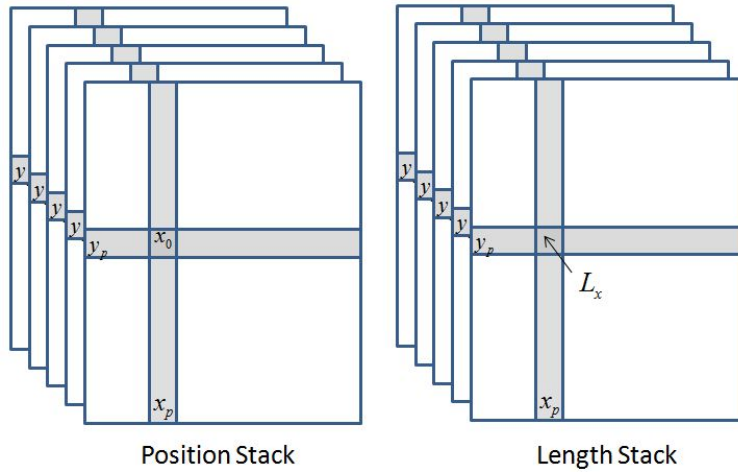


Fig. 5.7: Streak feature database

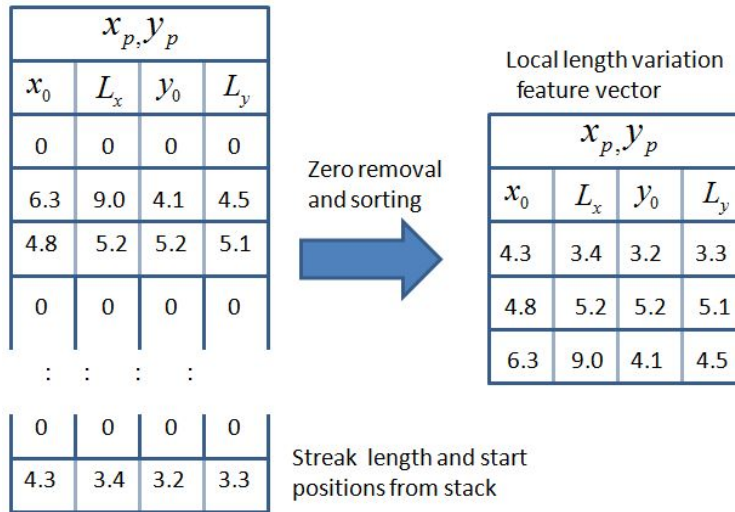


Fig. 5.8: Obtaining the local length variation table

approximation the streak lengths can be written as $L(x_0) = x_0(e^{aT} - 1) + \frac{b}{a}(e^{aT} - 1)$ which implies that $\frac{\partial L}{\partial x_0}$ has the same sign as the local spatial velocity gradient 'a'. Note that in the case of a closed form parametric expression for the Eulerian field, we can directly use the streak lengths to find the parameters by fitting methods.

Instead of using the local length variation table, the streak feature database can be directly used to obtain the spatio-temporal velocity estimate. This is actually a very quick

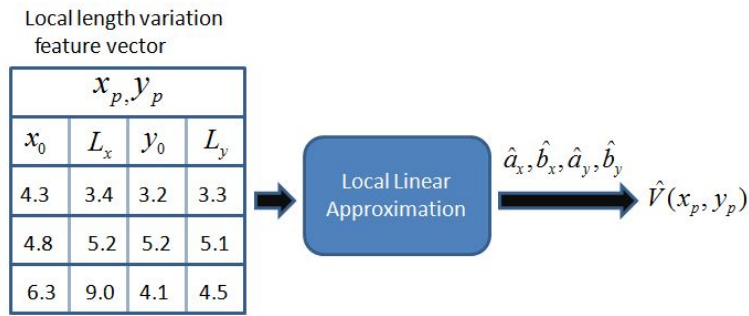


Fig. 5.9: Velocity estimate from local length variation table

method of obtaining the velocity field. The mean is computed for a pixel, through-the-stack. The biasing effect of the zero values can be eliminated by first obtaining a binary indicator stack of same dimension where the presence of a detected streak is indicated by '1'. Then the temporal sum is computed for the length stack and the indicator stack and their ratio gives the unbiased mean at that point (pixel).

CHAPTER 6

PARTICLE TRACK SIMULATION FOR KNOWN VELOCITY FIELDS

Particle velocimetry using image analysis is an effective non-intrusive method used for fluid velocity field estimation in micro-channels. However, the performance of velocity estimation algorithms is usually moderated by factors like particle density and the presence of strong velocity gradients. Consequently, it is necessary to run an experiment multiple times before the actual data collection process in order to determine the effectiveness of the imaging, qualitatively understand the nature of the velocity field and check the performance of an algorithm. Simulation of particle positions across time and space for known velocity fields would thus be extremely useful.

6.1 SIMULATED DATA FOR MICROFLUIDICS EXPERIMENTS – IMPORTANCE AND DIFFICULTY

Simulation of gold-standard data for user-designed microfluidic experiments is an important topic that has not received much attention, even though a vast majority of PIV and μPIV results, both experimental and theoretical are based on computer simulations. As pointed out in the works of Okamoto et al. [73] and Lecordier et al. [74] developers of different PIV and PTV algorithms have analysed the efficiency of their algorithms using their own evaluation procedures; standardized evaluation methods are extremely rare. In most of these simulations a Monte-Carlo approach is used where the consecutive images are generated by either simple shifts based on local averages of a known velocity field, or by a fixed motion model (usually affine). Multiple simulations and consequent processing then lead to required statistical estimations. Examples of such approaches can be found in the mainstream PIV work by Keane and Adrian [75], Raffel et al. [9], Wereley and Meinhart [23], Nogueira et al. [20] and also in PIV application, comparison and improvement methods [22, 76, 77, 78]. Well documented efforts to standardize simulated PIV data are also few and the efforts by Okamoto et al. [73] to create a standard test image library and the synthetic image generator (SIG) tool by Lecordier and Westerweel [74] were the only significant ones we could find, despite extensive literature review. In the standard image

test sequence, the velocity fields were simulated for a 3-D large eddy flow and the particle displacements from their random positions were based on this velocity vector field. The SIG tool was developed for EUROPIV2 (a PIV challenge competition) for generating test images, and it uses velocity vector fields obtained from other tools for flexibility. With the velocity fields, random particle images were used as earlier, but the tool incorporated the simulated optical set up so as to mimic different imaging conditions. Apart from the above mentioned methodology, there is also another class of simulations where the particle positions are found using closed form expressions [79, 80]. The existence (or the derivation) of a closed form expression that completely characterizes a complex system is quite unlikely and eventually the velocity fields used for such simulations are either classical ones for which closed form mathematical expressions exist, or are arbitrary and simple (e.g., linear).

Since our target is to develop an algorithm that can work for different channel geometries, we are more interested in the simulation methods that deal with arbitrary velocity fields, where closed form solutions do not exist for the displacement field. Many of these simulation models use velocity fields from CFD tools and the random particle locations are altered based on the velocity field by simple shifts, where for actual experiments this is certainly not so. An assumption on which such simulations are based is that the inter-frame time is extremely small and so is the exposure time. Hence, only point particles are imaged and consecutive frames are so close to each other in time that the motion of the tracer particles can be well approximated as simple shifts. This assumption breaks down easily for larger exposures or for larger time-lapse between successive images as now the shift between initial and final position is a complex shift which is the result of multiple simple shifts. However, it may be noted that this does not mean that this technique is unsuitable for μPIV studies. This is because μPIV is based on the fundamental requirement of fast imaging. For our purpose of simulating particle tracks, however, such methods will not work as now the finite time increment motion of the particle needs to be simulated based on a velocity field; i.e., all the positions of the particle need to be found and mapped to the image space. The main difficulty in generating such simulated data for arbitrary experi-

ments lies in the generation of particle pathlines for finite time intervals from a system for which the velocity vector fields are not expressible as closed form equations. Apart from this problem, the generation of velocity fields for an arbitrary user-designed device is often difficult.

We propose the use of computational fluid dynamics (CFD) simulation tools to generate velocity fields for micro-channel designs and then calculate progressive changes in particle position for given imaging parameters. This is then used to simulate images which can then be used to verify an algorithm's performance before it is used with real data. Since closed-form 2-D velocity equations are not easily available for most experimental micro-channel designs, this method helps simulate particle movement based on the underlying fluid dynamics equations. Also, it enables us to change experimental factors such as particle density and physical dimensions readily and re-evaluate the algorithm performance, ultimately leading to a more efficient velocity field estimation with real data. In this dissertation, COMSOL Multiphysics [81] was used as the CFD simulation tool, however other similar tools can also be used. The image generation framework established here is targeted to serve two important purpose. The first is to serve as a method by which particle motion can be visualized for arbitrary experiments and arbitrary experimental conditions and the second it to serve as a synthetic image generator which can generate particle images, particle track images and streamlines. Moreover, such a method was essential for this dissertation as, unlike PIV, there are no known repositories or tools for particle track images which have a corresponding known velocity field.

6.2 SOLUTION FOR 1-DIMENSIONAL VECTOR FIELD

Simulation of a particle streak requires particle positions on a finite time track (streak) to be generated from a known Eulerian field. Apparently, this is a direct problem and from our earlier discussions on velocity vector fields, the ODE representing the streamlines can be used. However, there are two practical factors that complicate the above computation. Firstly, the length is a time integral of the Lagrangian velocity which is generally not avail-

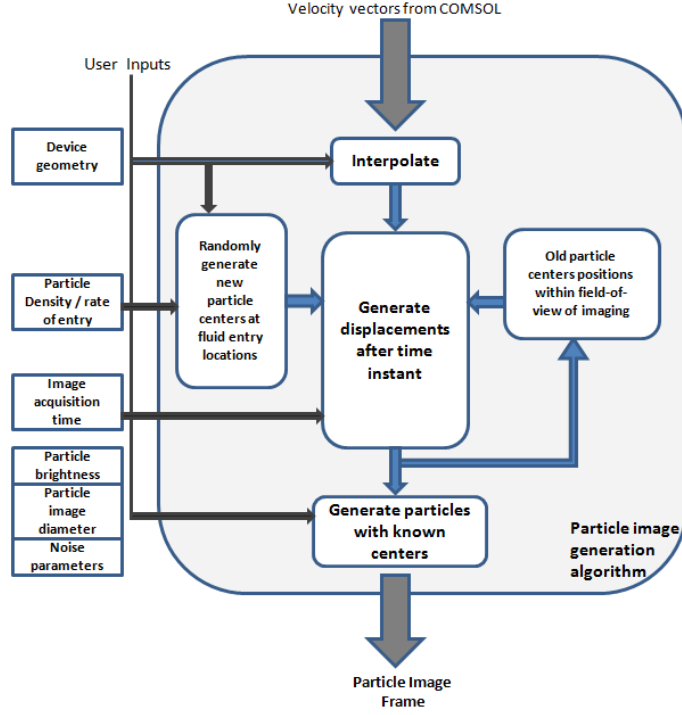


Fig. 6.1: Particle image generation block diagram

able. The Eulerian velocity is available which is related to the Lagrangian velocity as

$$V_L(x_0, t) = V_E(x, t)|_{x=\xi(x_0, t)}$$

where $x = \xi(x_0, t)$ represents the path taken by the particle (position-time instant dependence) which is unknown. Hence, the particle path equation needs to be evaluated first which can then yield the Lagrangian velocity by differentiation.

$$\frac{\partial \xi(x_0, t)}{\partial t} = V_E(x, t)|_{x=\xi(x_0, t)} \rightarrow V_L(x_0, t) = \frac{\partial \xi(x_0, t - t_0)}{\partial t} \rightarrow L = \int_{x_0}^{x_0+L} V_L(x_0, t) dt$$

The second factor is that $V_E(x)$ is generally not available in closed form for experimental systems. Instead, discrete samples of $V_E(x)$ might be available from CFD tools (e.g., COMSOL). Thus the form for $V_L(t)$ cannot be pre-computed. Numerical methods are used to solve for the particle track length. The methods are described for 1-D vector fields. For 2-D fields, the 1-D method can be reused and this is discussed later.

Algorithm 1 Particle track length by Modified Euler method

```
 $\Delta t \leftarrow \frac{T}{N}$   
 $x_f \leftarrow x_i$   
 $x_i \leftarrow 0$   
for  $i = 1$  to  $N$  do  
   $x_i \leftarrow x_f$   
   $x_f \leftarrow x_i + k\Delta t \frac{1}{2} [V_E(x_i) + V_E(x_i + \Delta t V_E(x_i))]$   
end for  
 $L \leftarrow x_f$ 
```

It may be noted that there are other possible methods than the ones described below; e.g., higher order Runge-Kutta methods. But these were the ones that were tested for performance for this dissertation. Computational accuracy and speed were the two main performance metrics and a more accurate and (or) faster method would allow improved replication of the real physics and (or) lead to lesser time in simulation. Another important point is that the streak positions calculated are for the center-of-mass of an ideal, spherical, tracer particle. Images from the particle positions and continuous particle positions (particle streak images) are also ideal. Accordingly, defocussing by depth or optics of the actual image is implemented as a post-track-processing image processing block, which is essentially a convolution process with the defocussing function (point spread function).

6.2.1 *The modified Euler method DE solver*

The modified Euler method is an improvement on the simple explicit Euler method and is a special implementation of the second-order Runge-Kutta method [82]. In terms of the exposure time T , the streak-length L , and the starting point x_0 , the numerical method is implemented using algorithm 1 above.

The advantages of using this method is that the number of steps is fixed at the start. However, there is no indication as to how small the step sizes should be. Extremely small step sizes would avoid larger errors but the computation time would increase. Moreover an extremely small step size may not be a required.

The next two methods work with the next step after the differential equation is

set-up, i.e. the expression for arc-length discussed in the third chapter.

$$\int_{x_0}^{x_0+L} \frac{d(x(\tau))}{V_E(x(\tau), t_0)} = \int_{t_0}^{t_0+T} d\tau$$

Since the velocity field is time-invariant, we have,

$$\int_{x_0}^{x_0+L} \frac{dx}{V_E(x)} = \int_{t_0}^{t_0+T} d\tau \quad (6.1)$$

6.2.2 Newton-Raphson method of finding roots

Here streak lengths are generated using the Newton-Raphson method [83]. If we consider the differential equation that relates the particle path and the Eulerian velocity, then we have

$$\frac{\partial \xi(x_0, t)}{\partial t} = V_E(x, t)|_{x=\xi(x_0, t)}$$

Using this directly to solve for L , we have

$$\int_{x_0}^{x_0+L} \left[\frac{1}{V_E(\xi)} \right] d\xi = \int_0^T dt \quad (6.2)$$

We then denote a function $f(L)$ as

$$f(L) = \int_{x_0}^{x_0+L} \left[\frac{1}{V_E(\xi)} \right] d\xi - T \quad (6.3)$$

where L is the root to the equation $f(L) = 0$. We can iteratively find the value of L by Newton-Raphson method. Consequently we need to find the terms for the root updating step of the Newton-Raphson method which is

$$L(i+1) = L(i) - \frac{f(L(i))}{f'(L(i))} \quad (6.4)$$

Now evaluating the derivative for the function f , we get

$$f'(L) = \frac{d}{dL} \left[\int_{x_0}^{x_0+L} \left[\frac{1}{V_E(\xi)} \right] d\xi - T \right] = \frac{d}{dL} \left[\int_{x_0}^{x_0+L} \left[\frac{1}{V_E(\xi)} \right] d\xi \right] \quad (6.5)$$

The above derivative can be obtained by Leibnitz's integral rule, from which we have

$$\frac{d}{dx} \int_{f_1(x)}^{f_2(x)} g(t) dt = g(f_2(x)) f_2'(x) - g(f_1(x)) f_1'(x)$$

Algorithm 2 Particle track length by Newton-Raphson method

```

 $v \leftarrow V_E(x)$ 
 $T \leftarrow T_{\text{exposure}}$ 
 $\delta L_{\min} \leftarrow 10^{-2}$ 
 $\delta L \leftarrow 1000$ 
 $g \leftarrow \frac{1}{v}$ 
 $L_i \leftarrow 0$ 
while  $\delta L > \delta L_{\min}$  do
   $L_{i+1} \leftarrow L_i - V_E(L_i) [I(L_i) - T]$ 
   $\delta L \leftarrow \left| \frac{L_{i+1} - L_i}{L_i} \right|$ 
end while
 $L \leftarrow L_i$ 

```

for a one-variable function g . Since $f(L)$ is also a monotonic increasing function (length always increases), if we let $g(\xi) = \left[\frac{1}{V_E(\xi)} \right]$, then

$$f'(L) = \frac{d}{dL} \left[\int_{x_0}^{x_0+L} g(\xi) d\xi \right] = g(x_0 + L) \cdot 1 - g(x_0) \cdot 0 \quad (6.6)$$

$$f'(L) = g(x_0 + L) \quad (6.7)$$

Hence the updating step becomes,

$$L(i+1) = L(i) - \frac{\int_{x_0}^{x_0+L(i)} g(\xi) d\xi - T}{g(x_0 + L(i))} \quad (6.8)$$

$$L(i+1) = L(i) - \left[\int_{x_0}^{x_0+L(i)} g(\xi) d\xi - T \right] V_E(x_0 + L(i)) \quad (6.9)$$

Algorithm 2 is used for the implementation of the Newton-Raphson method. Firstly, we let $I(L) = \int_{x_0}^{x_0+L} g(\xi) d\xi$ and $V_E(L) = V_E(x_0 + L)$ which represent a cumulative integral on the inverse of V_E and the value of V_E at a particular value of L distance from the starting point x_0 respectively.

The Newton-Raphson method is quick and does not require fixing the number of intervals, however it does need specifying the interval size in the numerical integration that needs to be performed (to get $I(L)$). It is also dependent on choice of the initial

starting point. For our simulations the initial point was chosen based on a linear assumption on the Eulerian velocity samples, for which the particle track length can be expressed in terms of the starting point, exposure time and linear field parameters a and b . It may be noted however that the method is not independent of the numerical integration. In the next method, we propose the direct use of numerical integration and solve for the root geometrically.

6.2.3 Geometric solution using cumulative integrals (GSCI) method

Let us start with a sampled 1-D Eulerian field as earlier. We assume that the vector field is smooth and non-zero ($V_E(x) \neq 0$). Now considering a function $g(x) = \frac{1}{V_E(x)}$ as earlier, we assume that the continuous function between a particular sample g_n and the immediately next sample value g_{n+1} is linear; i.e,

$$g_\lambda = \lambda g_{n+1} + (1 - \lambda)g_n; \lambda \in [0, 1] \quad (6.10)$$

It may be noted that a similar assumption is made on the function values (joined by a straight line) while applying the trapezoidal rule of numerical integration. With this setting, we proceed with the explanation of the GSCI method for obtaining particle track length. Firstly, we have from the usual pathline ODE

$$\int_{x_0}^{x_0+L} \frac{1}{V_E(x)} dx = T \quad (6.11)$$

Also, we define

$$I_n = \int_{x_0}^{x_n} \frac{1}{V_E(x)} dx \quad (6.12)$$

where n is an arbitrary discrete value index, while x_0 is the usual notation of the starting point. Fig. 6.2 gives a clear idea of the definitions.

From the diagram, we immediately see that

$$I_q = \int_{x_0}^{x_q} \frac{dx}{V_E(x)} = \int_{x_0}^{x_p} \frac{dx}{V_E(x)} + \int_{x_p}^{x_q} \frac{dx}{V_E(x)} \quad (6.13)$$

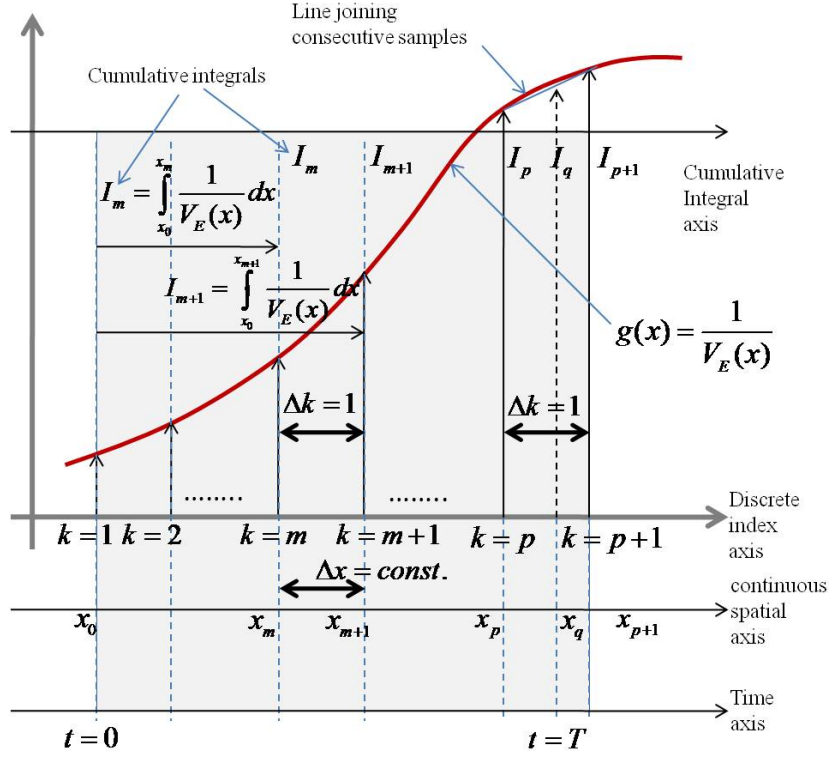


Fig. 6.2: Continuous and discrete relations for the GSCI method

or

$$I_p + \int_{x_p}^{x_q} \frac{dx}{V_E(x)} = I_q \quad (6.14)$$

But $x_q = x_0 + L$, so $I_q = T$, which gives

$$\int_{x_p}^{x_q} \frac{dx}{V_E(x)} = T - I_p \quad (6.15)$$

At this point we use the trapezoidal rule to obtain the value of the integral on the LHS. This gives

$$\frac{1}{2}(x_q - x_p) [g(x_p) + g(x_q)] = T - I_p \quad (6.16)$$

where $g(x)$ has the earlier definition (samples of $g(x)$ are index-wise inverted samples of

$V_E(x)$). We let $y = x_q - x_p$ which gives

$$y = \frac{2(T - I_p)}{g(x_p) + g(x_q)} \quad (6.17)$$

Now denoting $g_k = g(x_k)$ and considering a line joining the function values at p, q and $p + 1$, we have

$$g_q = \frac{g_p(x_{p+1} - x_q) + g_{p+1}(x_q - x_p)}{x_{p+1} - x_p} \quad (6.18)$$

Simplifying and noting that $x_{p+1} - x_p = \Delta x$ which is the unit of separation between samples, we get

$$g_q = y(g_{p+1} - g_p) + g_p \quad (6.19)$$

Equating the two expressions to eliminate g_q which is unknown, we get

$$y = \frac{2(T - I_p)}{y(g_{p+1} - g_p) + 2g_p}$$

$$(g_{p+1} - g_p)y^2 + 2g_p y + 2(I_p - T) = 0 \quad (6.20)$$

The above equation is a quadratic in y . Solving for the positive root, since $x_q > x_p$ we get

$$y(p, T) = \frac{\sqrt{g_p^2 + 2(g_{p+1} - g_p)(T - I_p)} - g_p}{(g_{p+1} - g_p)} \quad (6.21)$$

which gives us the position where the LHS of integral from the pathline ODE equals the exposure time T .

The above discussion is based on the fact that we locate the indices of the available contiguous samples between which the above discussed integral converges to a value T . Consider now the following diagram.

We observe that the function $f(L)$ defined in the earlier section changes sign between these two indices. Let \bar{I}_n be a $N \times 1$ matrix, each element of which is an integral on $g(x)$ as defined earlier. Then $\bar{U} = \bar{I}_n - T$ changes sign from negative at the $(p + 1)^{th}$ known index. Hence this can be obtained easily if we get \bar{I}_n . Now since \bar{I}_n represents a set of cumulative integrals, we can express \bar{I}_n as a product Ag where A is a predefined matrix

Algorithm 3 Particle track length by Geometric Solution using Cumulative Integrals

$$\begin{aligned}
 v &\leftarrow V_E(x) \\
 T &\leftarrow T_{\text{exposure}} \\
 g &\leftarrow \frac{1}{v} \\
 U &\leftarrow Ag - T \\
 [p &\leftarrow \max_p \{p : U(p) < 0\} \\
 L &\leftarrow x_p + y(p, T) - x_0
 \end{aligned}$$

Hence we have for this numerical method of integration

$$\bar{I}_n = A_R g; A_R = \begin{bmatrix} 1 & 0 & : & 0 \\ 1 & 1 & : & 0 \\ : & : & : & : \\ 1 & 1 & .. & 1 \end{bmatrix} \quad (6.23)$$

Similarly we can have a predefined matrix A for the trapezoidal rule or Simpson's rule. Now given the velocity field samples, with the predefined matrix, minimum computation time would be used for the computation of \bar{I}_n and we can quickly locate the sign change in the following expression and find the index (position) of sign change 'p'.

$$\bar{U} = Ag - T \quad (6.24)$$

Algorithm 3 for the GSCI method described uses some the function definitions stated earlier.

6.3 EXTENDING 1-D SOLUTIONS TO 2-D

In the previous section we discussed a some solutions to the streak-length determination problem from discrete Eulerian velocity samples of a 1-D velocity field. While this is also useful in many experimental situations (e.g., centerline particle path simulation for microfluidic channels), extending this to two-dimensions would give far more realistic simulations and help us obtain actual image sequences. There results would then be comparable to the images acquired from an actual particle visualization under the microscope. The added advantage is that the velocity fields responsible for the particle images are generated by a user in a CFD tool for a particular experimental schematic.

6.3.1 Pathline sampling of vector fields

Since we deal with only time-invariant fields here, pathlines are similar to streamlines. We use the given horizontal and vertical velocity fields $U(x, y)$ and $v(x, y)$ to first calculate the streamlines for particular starting points for the particles. While detailed description for streamline computation is not discussed here, given the velocity field components, we can calculate the stream-function which represents the solenoidal part and the stream-potential which represents the irrotational part of the flow. Knowing the stream-function and the stream-potential, we can calculate the streamlines. For the actual simulation this is accomplished by the ‘stream2’ function in Matlab which computes 2-D streamline data.

Once the 2-D streamline data points are known, the velocity field samples, both in X and Y are also known. Hence the distance between successive path points can be projected onto the X -axis and the corresponding net velocity values can be used as Y -axis values to get a 1-D velocity field. The concept is further explained in Fig. 6.4.

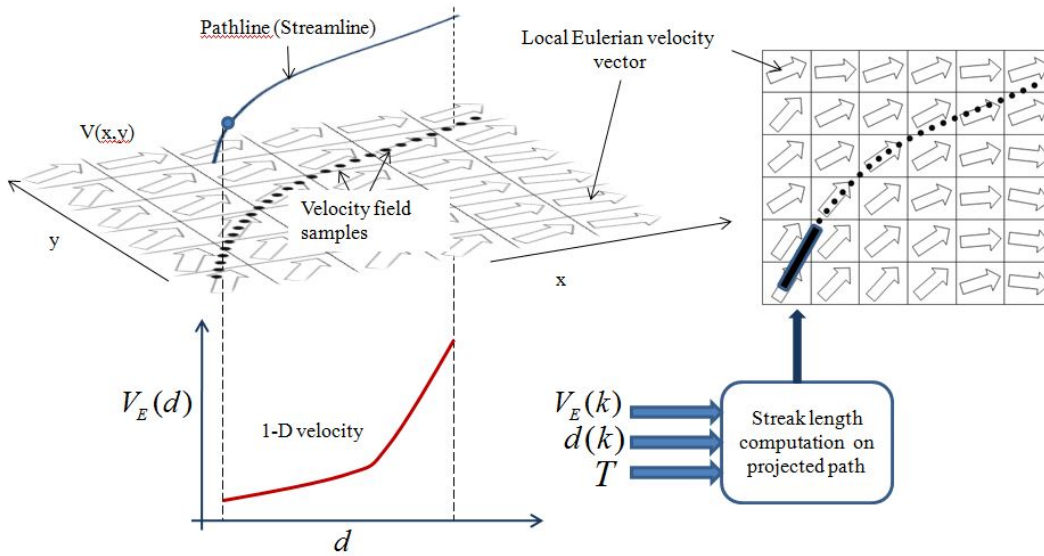


Fig. 6.4: Velocity field sampling by particle pathline

After the 1-D velocity field is obtained, the methods described in the previous section can be used to get the streak-length as well as the intermediate spatial points. With this

information we can either simulate the entire streak (all the pixels corresponding to the spatial points on the streak path are set to 1) or the point particle (either by actually setting the exposure time extremely small or just using the initial and final points, where we assume minimal exposure).

6.3.2 Pixel connectivity using the Bresenham's algorithm

The pathline samples can be far apart depending on the sampling density of the velocity field. This means that the pixels which get selected as contiguous points on the pathline are not actually so in the pixel-domain by the 4-connectivity or 8-connectivity definition. In such cases, these consecutive index pixels will need to be connected. Such a problem is usually encountered in computer graphics and game development and Bresenham's line algorithm [84] is often used for this purpose.

Bresenham's line algorithm determines which points in an n -dimensional raster should be plotted in order to form a close approximation to a straight line between two given points. It uses only integer addition, subtraction and bit shifting, all of which are very cheap operations in standard computer architectures and is one of the earliest algorithms developed in the field of computer graphics. We use this algorithm to get the indices of the pixels which connect disjoint pixels on the streak extent. This provides us with a more realistic simulation of the digitization that would have occurred in the case of an actual experiment.

6.4 THE STREAK SIMULATION FRAMEWORK

A complete streak simulation framework can now be constructed based on our earlier discussions. There is no restriction on the programming language but Matlab 7.1 (Mathworks, Inc.) was used to implement the algorithms. The 2-D velocity field components can be generated from any source but the corresponding import method has to be implemented accordingly. The schematic in Fig. 6.5 shows the interconnections of the different blocks of the framework. The small block in the bottom part of the figure shows the complete framework as a whole with only the input that changes for a particular experiment. Note

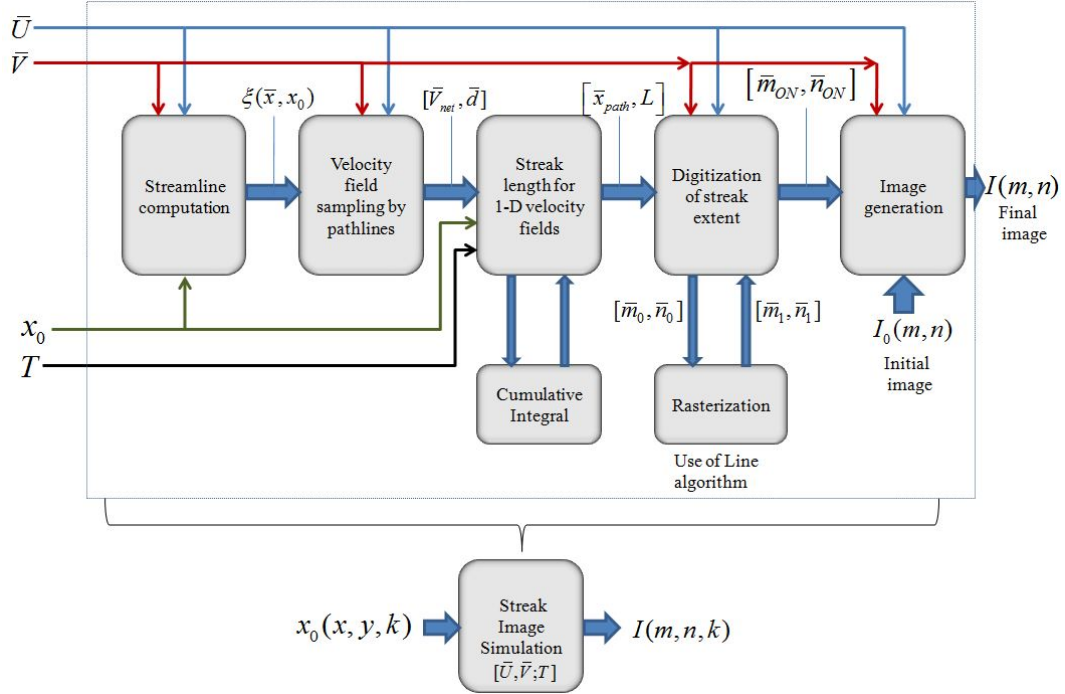


Fig. 6.5: The streak image simulation framework

that the velocity fields are steady (time-invariant) and hence fixed and so is the exposure time T . However, x_0 can change with position on the image frame (note that the coordinates are object coordinates; i.e., not discretized) as well as the index of the frame (k) in a sequence of frames. This block can now be used in a programming structure to generate image sequences. Image frames generated from this framework were used as baseline (gold-standard) images for this work.

CHAPTER 7

RESULTS AND PERFORMANCE EVALUATION

In this section we discuss the results and performances of the various methods of velocity field estimation and particle streak simulation that have been presented in this dissertation. The performance of the proposed methods is studied in an absolute sense against simulated data for which the actual velocity fields (1-D or 2-D) are known. In the section where we study the performance of the simulation method itself, we use velocity fields for which streak lengths are known as mathematical expressions. The distinct advantage of the simulation based performance analysis that is presented here is the elimination of a heavy image pre-processing framework to get high quality streak images for analysis. However this does not simplify the estimation or visualization (by particle streaks) problem since the test velocity fields which are used for data generation are complex and do not result in simple shifts over extended exposure (time) periods.

A considerable emphasis is put on the performance evaluation of 1-D simulation of streaks and 1-D velocity estimation. This is because for the 2-D simulation of streaks, the problem is reduced to a 1-D simulation problem where the particle traverses on the streamline and the length of the streak is determined by the net velocity field along this streamline. Hence the streak generation process is essentially a 1-D process as proposed here. In the case of the velocity estimation the velocity components are treated separately, thus resolving the streak length into X and Y components which are either used in a 1-D local linear approximation based estimation process or averaged spatio-temporally.

For the analysis of 1-D performance, four velocity fields were used. Of these, the linear, exponential and hyperbolic velocity fields have closed form expressions for the computation of streak length which is essential to have a quantitative error measure. Moreover these three velocity fields represent a progression from a field with zero local curvature to high curvature. Since curvature implies variation of local gradient, this set implicitly tests the performance of the local linear assumption. The last velocity field is a sigmoid curve. This was selected because its wide applicability to represent smooth transformation between two fixed states; e.g., the transition from a high velocity zone to a low velocity zone

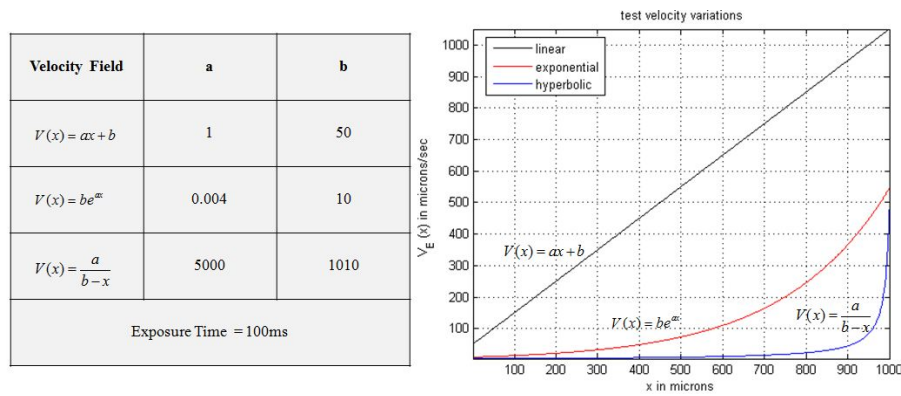


Fig. 7.1: 1-D velocity fields used for performance analysis.

in a microfluidic channel. Fig.7.1 shows the velocity fields used for performance analysis.

7.1 STUDIES ON THE FIRST ORDER APPROXIMATION

The proposed method is based on local first order approximation of smooth velocity fields. The errors for the first order approximation is studied here for the exponential and hyperbolic fields. The fact that the linear field has no error also implies that for practical applications, the local-linear approach for velocity field estimation would be highly effective for spatial regions-of-interest with fields which are constant, linear or piecewise linear.

7.1.1 Positional error associated with first order Taylor series approximation for 1-D fields

If a function (curve) is approximated by its first-order Taylor series approximation at a point, the error in the approximation depends on the local gradient at that point and how it contributes to the missing terms of the series. The relative error for a generic function when first order approximated can be described as follows. The first-order Taylor series approximation around a point x_p by an amount Δx is given as

$$V_E(x_p + \Delta x) \cong V_E(x_p) + \Delta x V'_E(x_p)$$

and the relative error is defined as

$$e_r = \frac{V_{E, \text{true}} - V_{E, \text{est}}}{V_{E, \text{true}}}$$

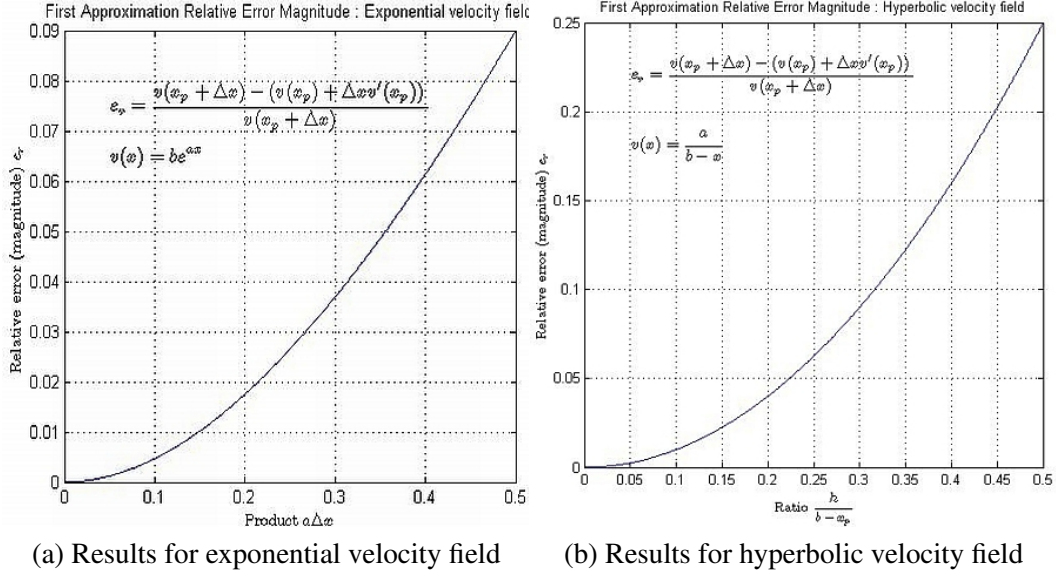


Fig. 7.2: First order approximation relative error magnitudes for exponential and hyperbolic velocity fields

Hence the relative error for the first-order approximation is

$$e_r = \frac{V_E(x_p + \Delta x) - V_E(x_p) + \Delta x V'_E(x_p)}{V_E(x_p + \Delta x)}$$

$$e_r = 1 - \frac{V_E(x_p) + \Delta x V'_E(x_p)}{V_E(x_p + \Delta x)} \quad (7.1)$$

Here we want to show how much the gradient change affects the velocity field estimation at a fixed point. Only fields with variable gradient change are considered. For the exponential field, we have $V(x) = be^{ax}$. Hence, $V'(x_p) = abe^{ax_p}$ which gives

$$e_r = 1 - \frac{be^{ax_p} + \Delta x abe^{ax_p}}{be^{a(x_p + \Delta x)}} = 1 - \frac{1 + \Delta xa}{e^{a\Delta x}}$$

Similarly for the hyperbolic velocity field function we have, $V(x) = \frac{a}{b-x}$. Hence, $V'(x_p) = \frac{a}{(b-x_p)^2}$ which gives

$$e_r = \left(\frac{\Delta x}{b - x_p} \right)^2 \quad (7.2)$$

The relative error of first order approximation at each point is shown in Fig. 7.2. As can be seen the relative error increases exponentially. For these two functions considered the

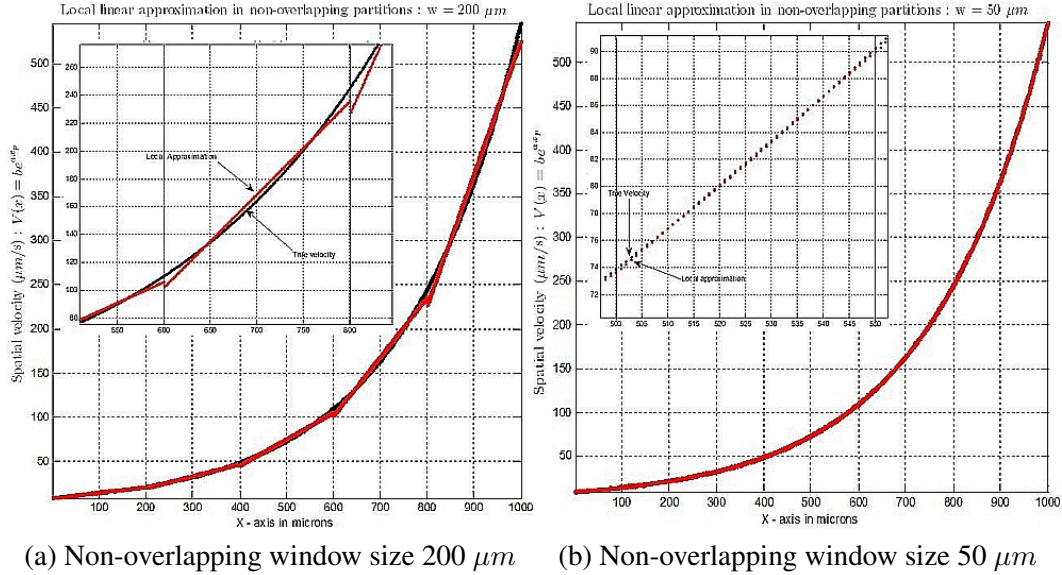


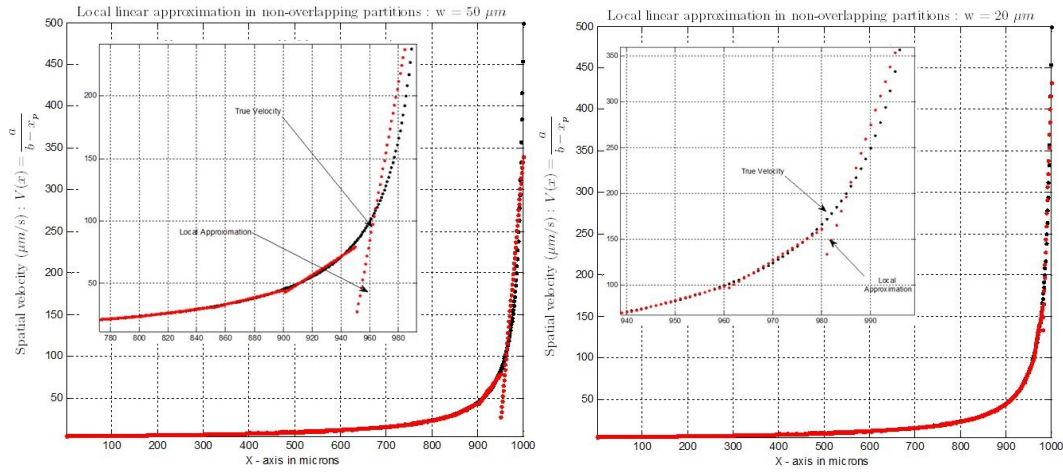
Fig. 7.3: Tracking performance of spatio-temporal averaging for exponential velocity field

relative error is also seen to depend on a pure ratio, $a\Delta x$ for the exponential and $\frac{\Delta x}{(b-x_p)}$ for the hyperbolic function. Note that for each case the increase in the deviation from the point of observation increases the error and this is because of the increase in truncation error for the Taylor series.

7.1.2 Qualitative tracking performance for local liner approximation

Since our approach for velocity field estimation considers all the streaks ‘seen’ at a point in space over time, and then uses the starting positions and lengths of these streaks, the union of the spatial extent of all the streaks being considered is the domain over which the linear approximation is done. Hence, instead of the local approximation at a point and considering the deviation around a point, we check here the error introduced with subdividing the velocity field into discrete regions of fixed width and then fitting the velocity function for each region by a straight line. The following two figures show the approximation performance for regions of different width. As expected the smaller width has lesser error because the piece-wise linear approximation is better.

In Fig. 7.3, the performance for the exponential velocity field is shown for non-



(a) Non-overlapping window size $50 \mu m$ (b) Non-overlapping window size $20 \mu m$

Fig. 7.4: Tracking performance of spatio-temporal averaging for a hyperbolic velocity field

overlapping subdivision widths of $200 \mu m$ and $50 \mu m$. The discontinuities are clearly seen in the case of the $200 \mu m$ width. An important observation is that the width also indicates the maximum particle streak lengths that may be observed and hence the exposure time that could have been used. For example, considering an average velocity of $70 \mu m/s$ for the subdivision between 600 and $800 \mu m$, the time for the interval is about 3 seconds. While the targeted image acquisition system is slow, it would still operate in milliseconds range, which means that particle streaks would be shorter, and hence so would the actual widths.

The performance for the hyperbolic velocity field function is shown in Fig. 7.4. As can be seen, for the parameters selected, the hyperbolic field is far more sensitive and while it is smooth, the local gradient changes from about 0.4 between 800 and $900 \mu m$ to about 6 between 950 and $1000 \mu m$. Similar sharp changes in local velocity gradient is not impossible in microfluidics but is surely less common. However, we use this to show that the $50 \mu m$ is no longer a good width and better results are obtained by its further reduction. While this is achievable by reducing the exposure time, there would exist a trade-off between resolution (longer streaks better) and fidelity of tracking (shorter streaks better).

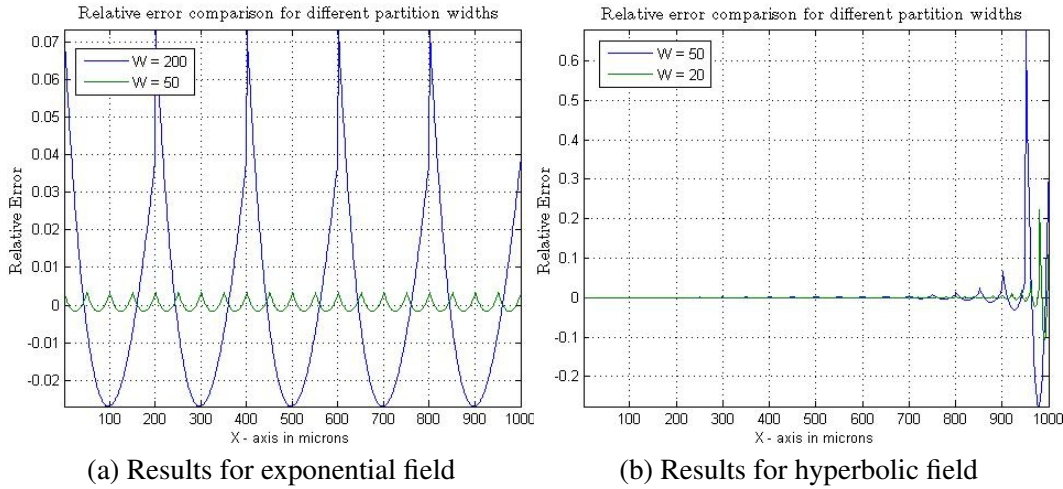


Fig. 7.5: Relative error for different window widths - exponential and hyperbolic velocity fields

7.1.3 Relative error performance and improvements by sliding window

The relative error performance for different widths is shown in Fig. 7.5. For the exponential field the error changes from 7% to about 0.5% by changing the window size. For the hyperbolic field, the error is extremely small in the beginning for both the widths and then becomes as high as 60% for the larger window and 30% for the smaller. Also, the nature of the error variation is fixed for the exponential function and not for the hyperbolic case. This is evident from the difference of their relative error expressions, where the hyperbolic field shows positional dependence.

Apart from considering local function approximations in a window, in the proposed velocimetry method, the window gets actually shifted. This is because every point in the horizontal space is processed successively for the ‘observed’ streaks and toward parameter evaluation. Hence we use a sliding window, estimate the linear approximation and then estimate the velocity for the center of the window using the approximation.

The sliding window reduces the relative error, as can be seen in Fig. 7.6 but for the hyperbolic field, its error is still as high as 10% for the smaller window. Hence for very high changes in local gradients, relative errors would increase for the proposed velocity

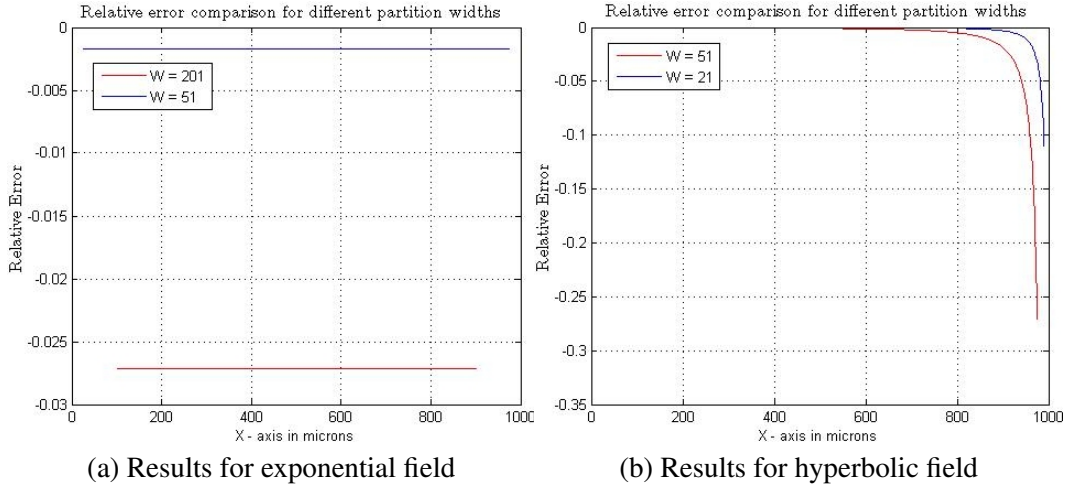


Fig. 7.6: Relative error for different sliding window widths - exponential and hyperbolic velocity fields

estimation. We note this as a limitation to our proposed method but realize that this is a limitation with which all quantitative imaging based velocity estimation methods work. As discussed earlier, such extreme local gradient velocity changes seldom occur for most microfluidic experiments and when present, counter measures can be taken to reduce the velocity gradient. For example, the application of back-pressure (hydrodynamic force) against electrokinetic flows.

7.2 PERFORMANCE OF POSITION SPECIFIC ASSIGNMENT OF L/T ESTIMATE ON STREAK EXTENT

Some interesting results are shown below for the point assignment of estimated average Lagrangian velocity. Fig. 7.7 shows the change in relative error magnitude that can be achieved by assigning the L/T value at the correct position on the streak. An important point to note however, is that the cost of this assignment is a streak while the output is only a single point on the velocity field. Hence, even if the assignment is accurate, the method is not efficient, since it implies that in order to map the complete region-of-interest, a corresponding strategically placed streak would be present. For an actual experimental scenario this condition might be reached asymptotically with time, but for smaller times

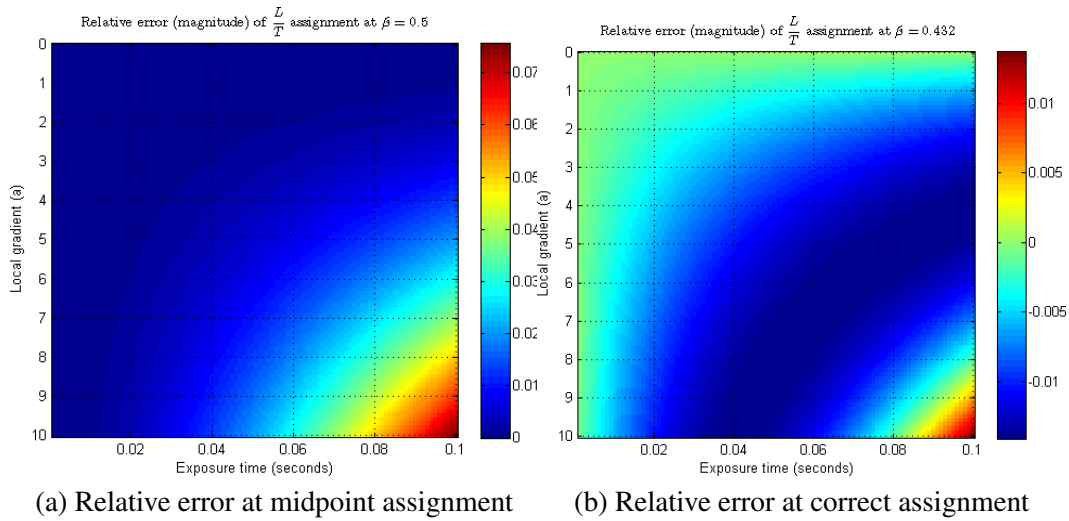


Fig. 7.7: Shift in the relative error magnitude with variable local gradient and exposure time at the midpoint and exact assignment positions

we would have to resort to interpolation schemes involving large spatial grids. Ideally, we would like to assign multiple spatial locations accurately from a smaller set of streaks.

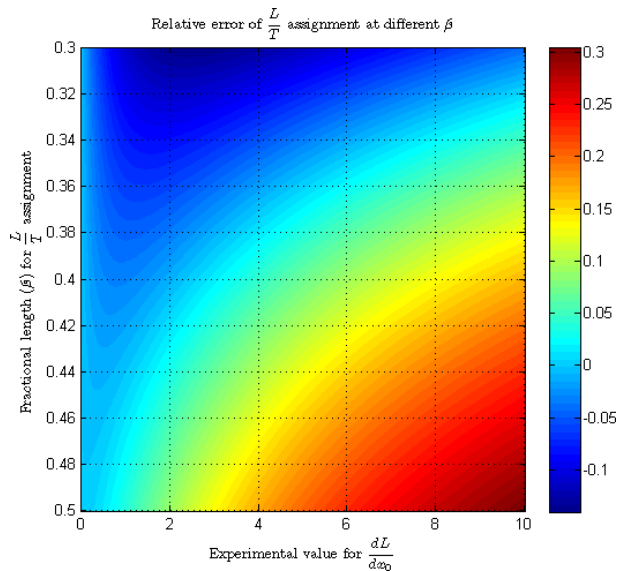


Fig. 7.8: Relative error of L/T assignment for variable β and variable rate of change of streak length with respect to the starting position

Another result is shown in Fig. 7.8 which is obtained by plotting the relative error

surface for $\frac{dL}{dx_0}$ varying between 0 and 10 and β values between 0.3 and 0.5. Note that at smaller gradient values, the L/T value can be assigned anywhere in the range while it becomes very selective as the gradient increases. This figure also shows how the β value should be chosen for a given tolerance. For example if the values of $\frac{dL}{dx_0}$ is around 5, the L/T value can be assigned anywhere between the middle of the streak and the starting one-third for a 20% error tolerance. Accurate knowledge of β can also be obtained for given tolerance and $\frac{dL}{dx_0}$ value and an expression for 1% tolerance was discussed in Chapter 3.

7.3 PERFORMANCE OF THE PARTICLE STREAK SIMULATION FRAMEWORK

Performance for the particle streak simulation methods is discussed in this section. Particle streak simulation requires the particle positions on a finite time track (streak) be generated from known discrete Eulerian field samples. In Chapter 6, different numerical methods are utilized to obtain the particle streak length. These simulation methods are first studied individually and then compared for computation time for a fixed relative error.

7.3.1 Particle streak simulation for 1-D fields

The two most important aspects to consider while comparing simulation strategies are computation-time (T_c) and relative error (e_r). To quantify the relative error, the baseline needs to be set, and this is done by using velocity fields for which the streak-lengths can be pre-determined. The expressions for the streak-length are shown in Fig. 7.16 for the three different velocity fields. For each of the methods, computation time and relative error plots are obtained.

The modified Euler method

The modified Euler method is an improvement on the simple explicit Euler's method and is a special implementation of the second-order Runge-Kutta method [82]. While generating the particle streaks, the discrete samples of the velocity field and the starting point was input to the algorithm and the output was the particle track length. This was done for a spatial extent of 400 microns. Fig. 7.9 shows the time performance in the first row and the

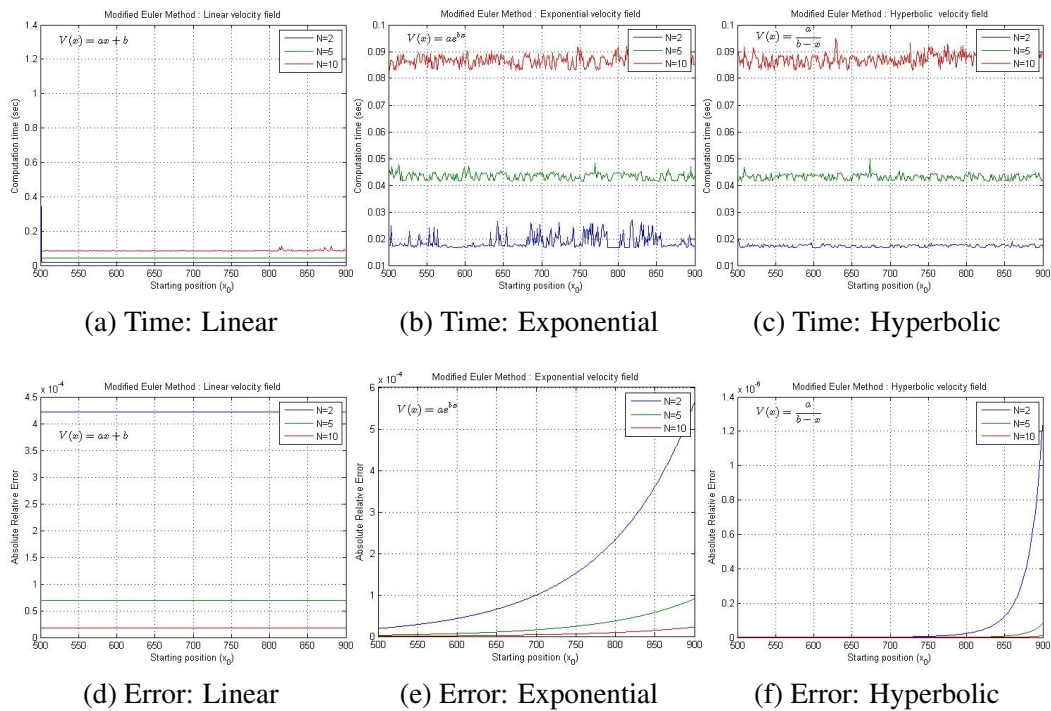


Fig. 7.9: Computation time and relative error performance for streak length calculation for different velocity fields using the modified Euler method

relative error performance in the second row. The first column shows the results for the linear velocity field, followed by the exponential and hyperbolic velocity fields.

The accuracy and the computation time in Euler's method is controlled by the fixed number of intervals by which the exposure time is subdivided. This is the parameter N in the plots. In each of the plots, 3 graphs are drawn for different values of the parameter N . With larger values of N , the relative error reduces but the computation-time increases and this effect is uniform across all the 3 different velocity fields. Also note that the relative error is actually very small for all the values of N and for all the fields. Hence the more important factor is the computation time since a large number of streaks would have to be simulated for visualization and estimation purposes.

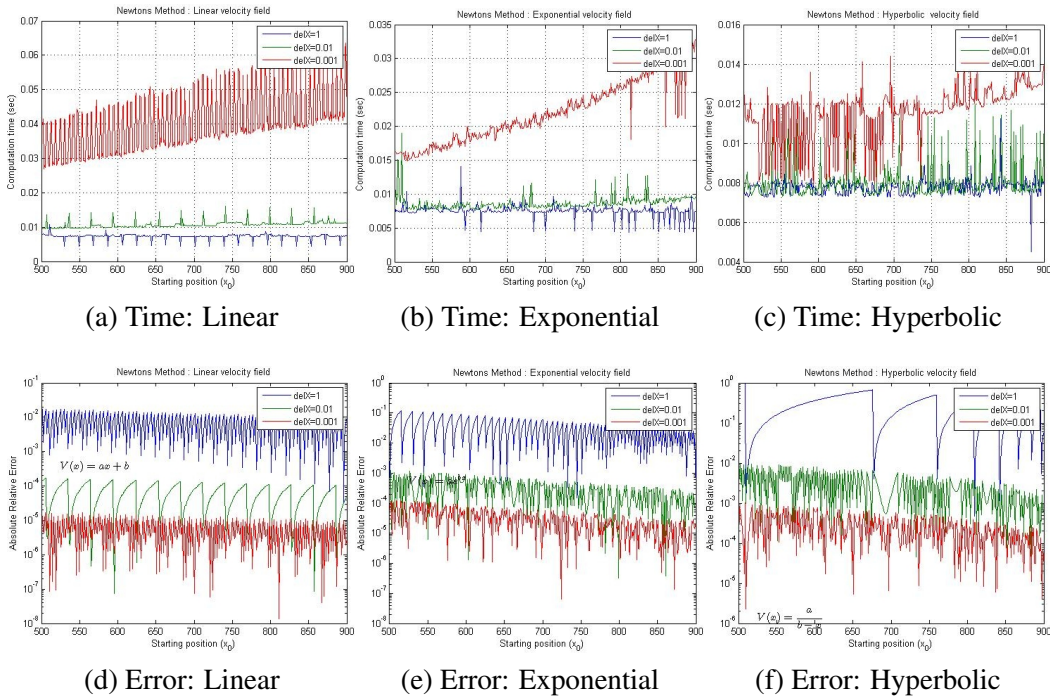


Fig. 7.10: Computation time and relative error performance for streak length calculation for different velocity fields using the Newton-Raphson method

The Newton-Raphson method

In the Newton-Raphson method [83], each successive step obtains a better approximation of the root of an equation. In our case this root is the final position of the particle where the total time elapsed is also the total exposure time. The derivation for the position update step can be found in Chapter 6. Although they cannot be directly compared since the controlling parameters are not same, the Newton-Raphson method on an average is considerably faster than Euler's method for the test velocity fields. This fact is more clearly observed when the methods are compared for fixed relative error.

Results for computation time and relative error are shown in Fig. 7.10. In each of the plots, 3 graphs are drawn for different values of the parameter ΔX which is the fixed increment on the particle position in each step of the iteration, till the total time elapsed equals the exposure time. With smaller values of ΔX , the relative error reduces but the

computation-time increases.

It may be noted that although the computation time and relative error plots are obtained as expected, the magnitude of the computation time is larger for the linear velocity field for the Newton-Raphson method. This can be explained by the fact that the linear velocity field function is actually used as a denominator in the velocity estimation update step. This effectively makes it a hyperbolic function for which the first order approximation at a point gives large variations, unless smaller deviations are chosen around that point. Hence this translates into the requirement of smaller spatial intervals for the Newton-Raphson method, eventually leading to larger computation times.

The GSCI methods

The proposed Geometric Solution using Cumulative Integrals (GSCI) method uses either a trapezoidal rule or a Simpson's rule based integration for the determination of the cumulative integral and the method of obtaining the cumulative integral is discussed in Chapter 6. The results for the computation time and relative error are shown in Fig. 7.11. In each of the plots, 2 graphs are drawn for the two methods of numerical integration that was used. It may be noted that both the methods are inherently the same. It can be seen that the GSCI (trapezoidal) method is slightly less accurate than GSCI (Simpson's) but takes less computation time.

An interesting observation is that the computation time performance is very uniform across the test velocity fields and the computation time magnitude decreases quickly as the spatial extent changes. This is due to the fact that in order to compute the particle track length the cumulative integral needs to be evaluated at each step. As the limits of the spatial extent over which the cumulative integral needs to be evaluated changes (reduces), so does the computation time. For the method used to compute the cumulative integral, the time taken varies as $O(N^2)$ for trapezoidal rule and as $O(2N)^2$ for the Simpson's rule, where N is the number of discrete points over which the cumulative integral would be computed. Accordingly, Simpson's rule has a higher computation time at the same spatial point

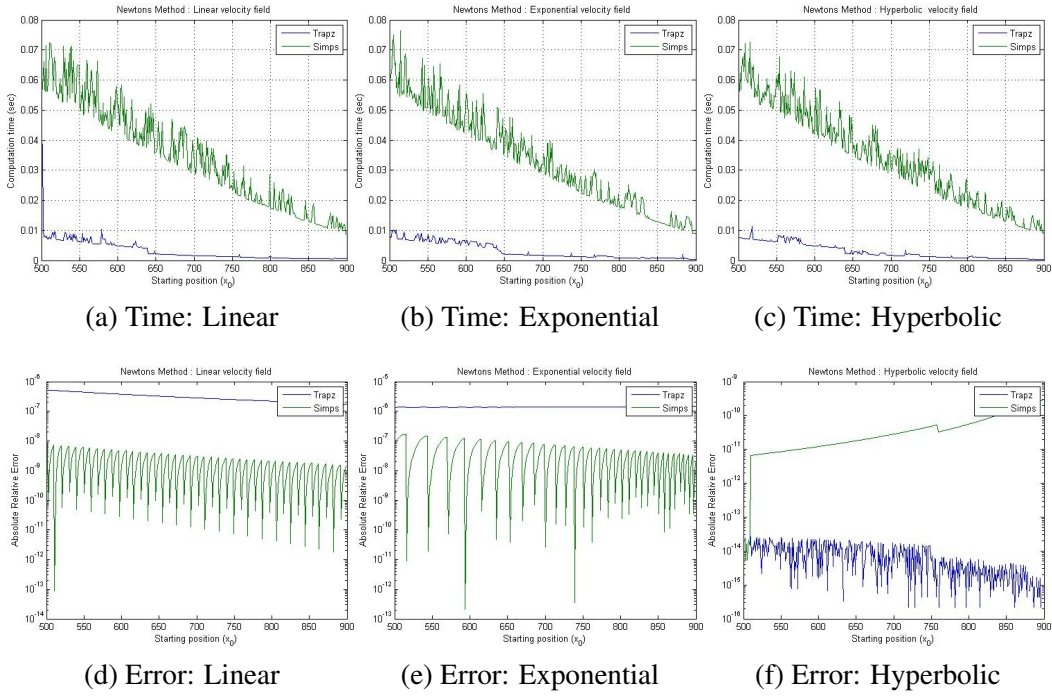


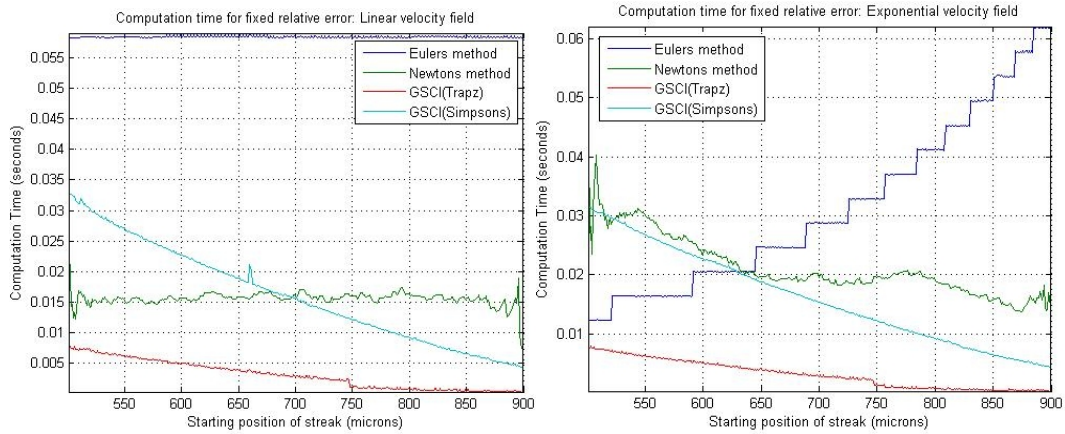
Fig. 7.11: Computation time and relative error performance for streak length calculation for different velocity fields using the GSCI method

compared to the trapezoidal rule and computation time for both decrease as N decreases.

Another important observation is that while the relative error is usually larger for the trapezoidal rule, it is smaller for the hyperbolic field case. This is because, upon inversion, this becomes a linear function over which the numerical integration occurs causing the trapezoidal rule to outperform Simpson's rule.

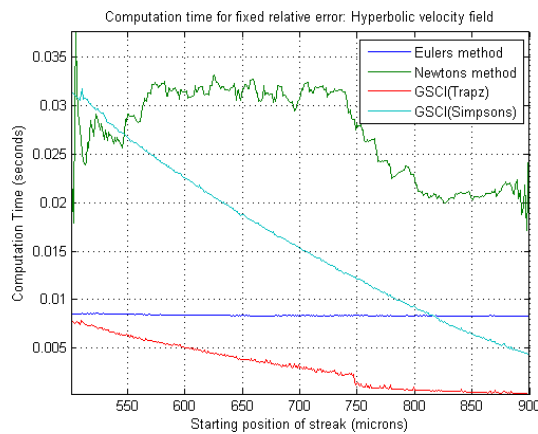
Comparative computation time performance

Comparative performance is studied by fixing the relative error. This means that for each of the methods, the control parameters (e.g., N for the modified Euler method) were changed till the relative error value was less than 10^{-5} . The computation time for that particular control parameter is then selected. The GSCI method does not have a control parameter and the usual performance was seen to be always below the targeted relative error. However for each selection of the computation-time, 100 iterations were performed and the average time



(a) Time performance - Linear field

(b) Time performance - Exponential field



(c) Time performance - Hyperbolic field

Fig. 7.12: Comparative computational time performance for streak length computation for different velocity fields.

was used for comparison. Thus for the curves shown in Fig. 7.12, the computation time for each of the 400 spatial points results from 100 experiments.

For the linear velocity field, the modified Euler’s method takes the maximum time. Moreover, its time performance is consistent over the spatial extent. The GSCI (trapezoidal rule) is seen to perform best followed by Newton’s method. For the exponential velocity field, the modified Euler method takes the maximum time on average again, though at the start (of the spatial extent) it is much faster. Also its time performance is not steady over the spatial extent, unlike the linear case earlier. The GSCI (trapezoidal rule) is seen to perform

the best followed by the Newton's method for the exponential velocity field. The modified Euler method is seen to perform much better for the hyperbolic velocity field and again its time performance is spatially consistent. The GSCI (trapezoidal rule) is again seen to perform best followed by Newton's method.

7.3.2 Particle streak simulation for 2-D fields

Particle streak simulation for 2-D fields is similar to the 1-D case except here the particle pathline information is used to sample the horizontal and vertical velocity field components, to obtain the net velocity field with which the particle moves in the 2-D plane. The net velocity field and the pathline is then used for 1-D particle streak simulation. From the performance study of the 1-D simulation methods done previously, it becomes clear that the GSCI (Trapezoidal) method performs the best in terms of time. Since its accuracy is also very high, this method was selected for simulating streaks for given 2-D velocity fields

The first 2-D velocity field is the pressure-driven, steady Poiseuille flow in a microchannel. This particular flow is of major importance for the basic understanding of liquid handling in microfluidic systems [60]. The velocity field is obtained in COMSOL Multiphysics by designing a simple channel with an inlet and an outlet. The pressure on the inlet was selected to be higher than the outlet pressure. Note that this pressure difference can easily be created by using reservoirs of different height at the two ends of the channel. This results in a steady state velocity field as shown in Fig. 7.13(a). The streamlines for this vector field are shown in Fig. 7.13(b). A frame of simulated streaks and a pathline plot obtained from the streaks is shown in Fig. 7.13 (c) and (d) respectively.

The image frame containing the streaks was obtained for a time interval of 40 milliseconds and the image generation time was around 100 milliseconds per frame in a standard notebook computer with a 2.2 GHz processor and 4GB of RAM. The algorithm implementation was done using Matlab 7.1 (Mathworks Inc.). Note that faster processors and large memory would definitely decrease these numbers. Moreover the choice of the number of particles that are new for each frame depends on the user, and more particles

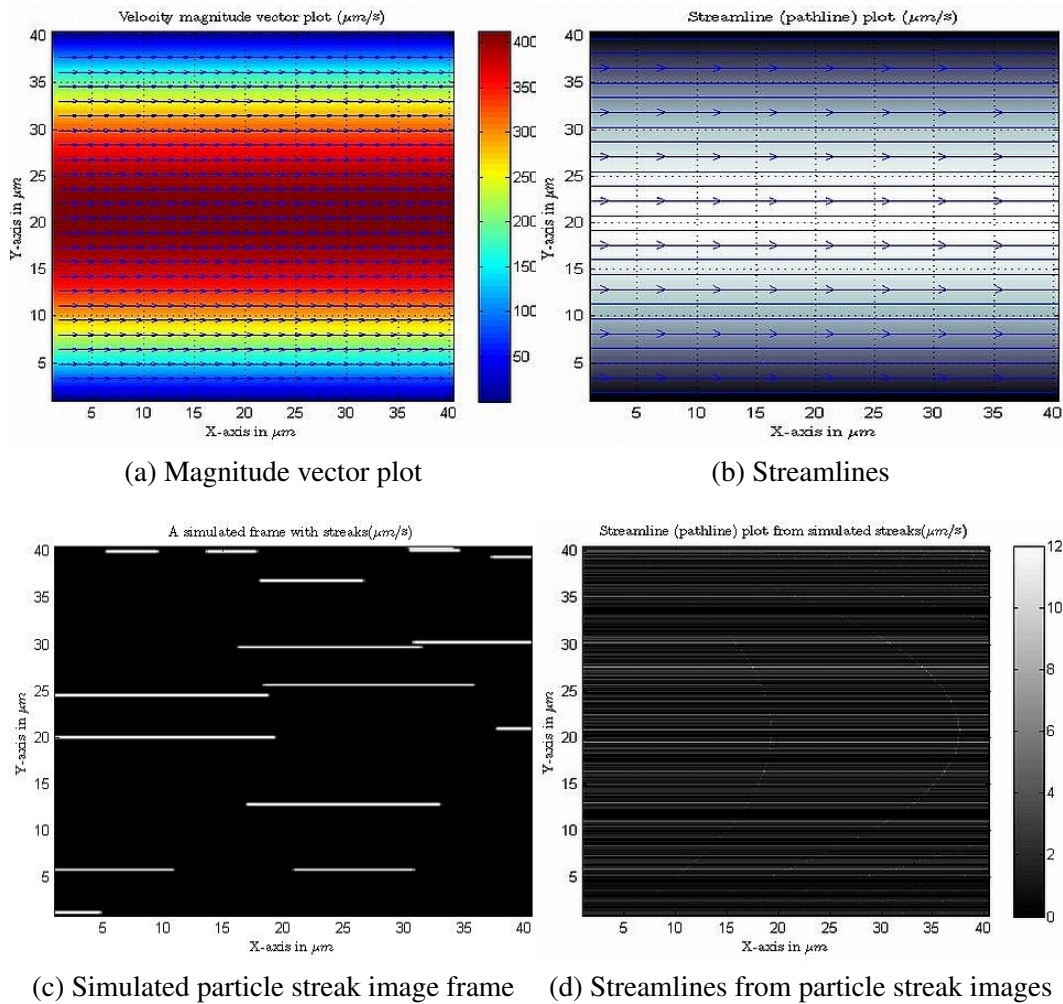


Fig. 7.13: Particle streak simulation for steady Poiseuille flow

mean more time to simulate each frame. In the simulated frame, the change in length in the vertical direction can be clearly seen. The pathline plot can be obtained from a set of streak image frames by either obtaining the maximum-intensity-projection (MIP) for this set or by simply summing them over time. Summing was done in the figure shown and the colorbar on the plot in Fig. 7.13(d) shows the number of times an unique particle streak was observed at a spatial position.

The second velocity field is for the steady flow of an inviscid fluid past a cylinder obstructing the flow. This is a typical example of irrotational flow where the velocity

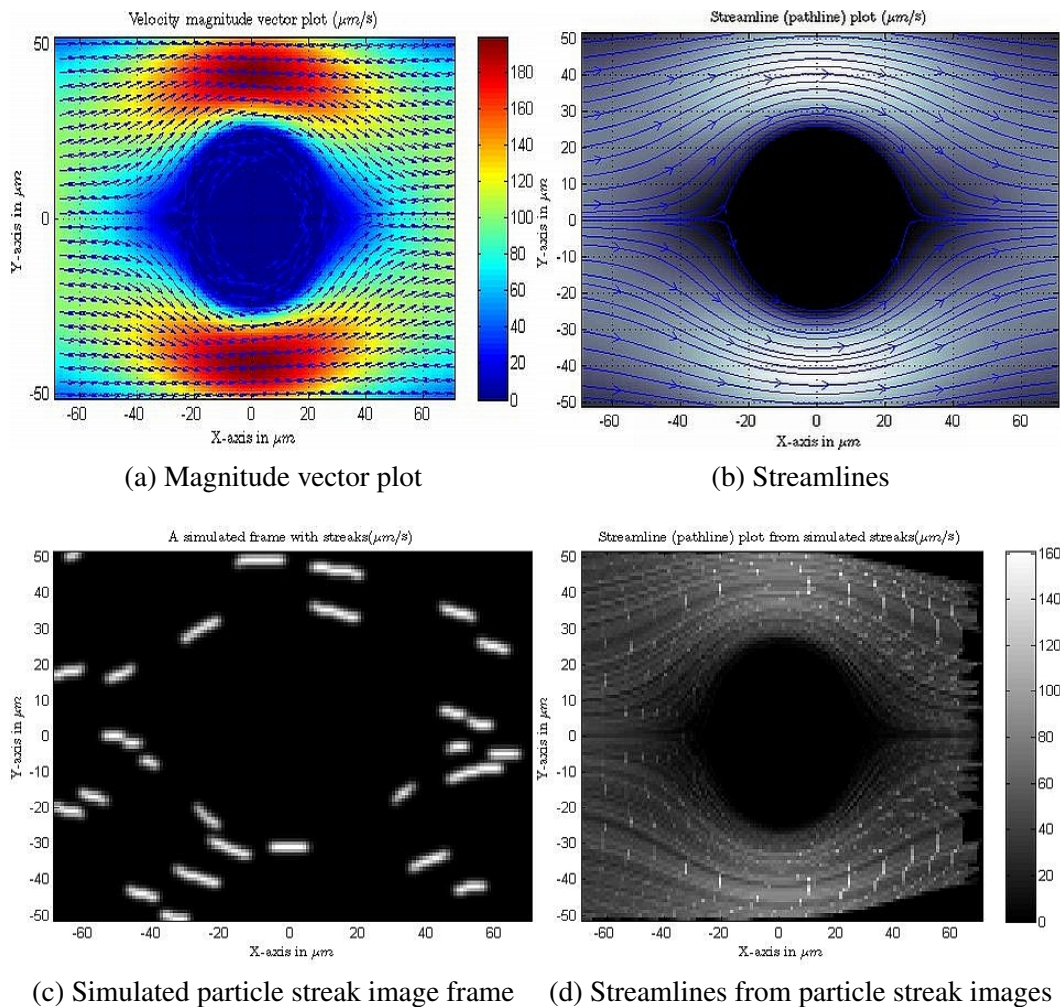
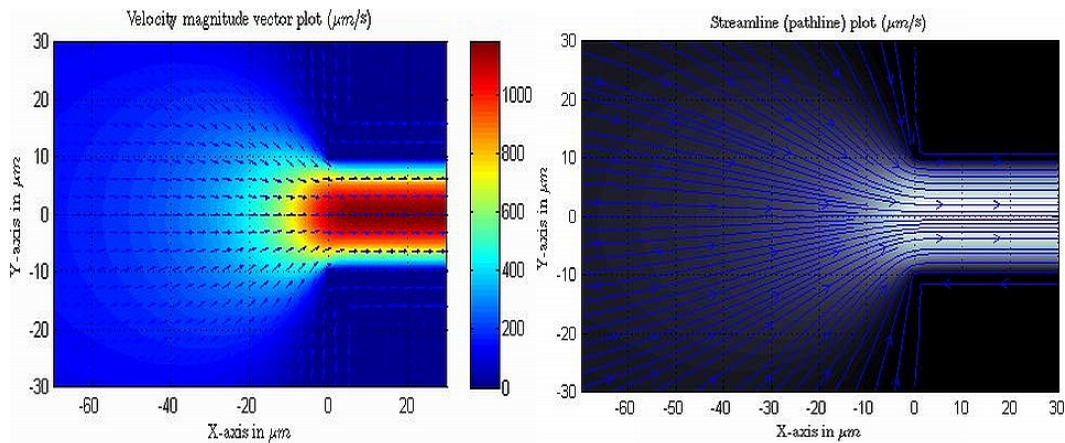


Fig. 7.14: Particle streak simulation for steady flow around a cylindrical obstacle

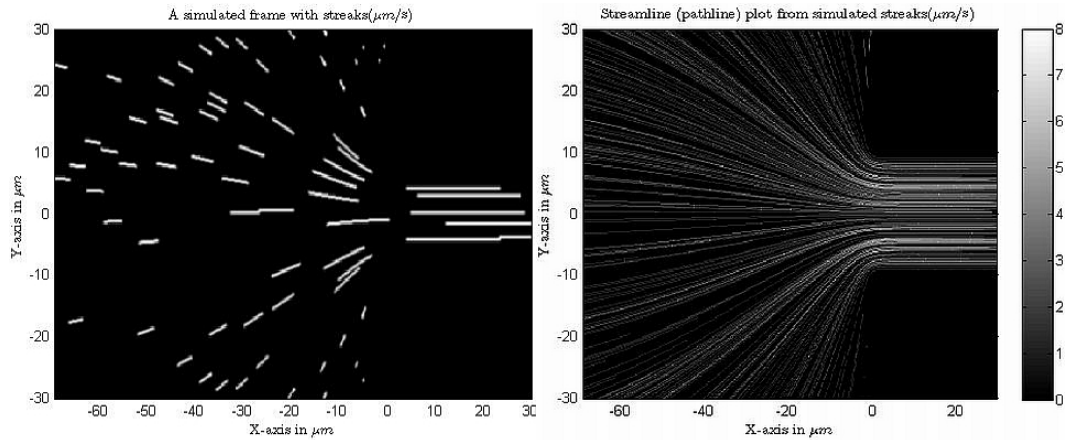
streamline approaching the flow divides and there is flow around both sides of the cylinder. The velocity field was obtained in COMSOL Multiphysics and this was used to simulate the streak image frames. The exposure time was 80 milliseconds for the streak image simulation.

Fig. 7.14 shows the velocity magnitude, streamlines, the particle streaks simulated and the streamlines generated from the particle streaks. It may be noted that the streamlines (pathlines) obtained from the streaks clearly resolves the location of the two stagnation points on either side of the cylindrical obstruction. This is an extremely useful result which



(a) Magnitude vector plot

(b) Streamlines



(c) Simulated particle streak image frame

(d) Streamlines from particle streak images

Fig. 7.15: Particle streak simulation for steady flow at the junction of rectangular channels

can readily be obtained if particle streaks are used (rather than particles).

The particle streaks generated were ideally single pixel thick but were processed through a Gaussian blurring function that resembles a combined point spread function which smears the otherwise sharp particle image. For the simulated frames the particle images were allowed to have an image diameter varying from 1 pixel (just the center) to 5 pixels.

The third velocity field is for a steady hydrodynamic flow that is obtained when two channels of different width meet at a junction and the ends of the two channels are kept at

a pressure difference. This field was selected as such a junction is common in microfluidic systems and also for the reason that the local gradient changes sharply near the entrance of the smaller channel. The velocity field was obtained in COMSOL Multiphysics and this was used for streak image simulation. The exposure time was set at 10 milliseconds since larger exposure times resulted in more overlapping.

Fig. 7.15 shows the vector field magnitude, streamlines, the streaks and the streamline obtained from the streak images. As earlier, the streamlines from the streaks are very similar to the streamlines obtained by computation. The change in local velocity can be observed in the streak image from the streak image lengths and from the colorbar in the figure showing the actual velocity field.

7.4 PERFORMANCE OF SPATIO-TEMPORAL AVERAGING

The estimation of velocity field by spatio-temporal averaging has been discussed earlier in Chapter 3. In this section we show the performance of this averaging method for some velocity fields for which the expressions for streak length can be calculated (for 1-D fields). We also show the performance of the method for 2-D estimation problems where the 2-D streak images are obtained for known velocity fields by the streak image simulation framework described in Chapter 6. The measurement noise performance of the spatio-temporal averaging method is studied later, comparatively with the local linear approximation method.

7.4.1 *Spatio-temporal averaging for 1-D fields*

The spatio-temporal averaging method works by selecting an observation point on the spatial axis and streak lengths observed at this point are averaged. This mean streak-length on time averaging gives the velocity estimate at that point. The starting positions for increasing velocity fields are given by $x_0 \in [x_p - L_{\min}, x_p]$ and once the starting positions are known, closed form expressions for streak-length can be used to determine streak lengths for x_0 values within the above range. These can then be used to estimate the velocity as described earlier. The previously described velocity fields are used to study the performance

of spatio-temporal averaging in 1-D. For the first three velocity fields, we can express the track length as closed form expressions depending only on the velocity field parameters, exposure time and starting point and for these, the maximum and minimum streak-length expressions are tabulated in Fig. 7.9 In order to get the expressions for minimum length, we substitute $x_p - L_{\min}$ for the initial starting position. The minimum length defines the domain within which a streak observed at x_p could have originated and accordingly we can obtain the lengths observed at the position x_p .

$V(x)$	L_{\min}	L_{\max}
$ax + b$	$\left(x_p + \frac{b}{a}\right)(1 - e^{-aT})$	$\left(x_p + \frac{b}{a}\right)(e^{aT} - 1)$
$b e^{ax}$	$\frac{1}{a} \log(1 + abT e^{ax_p})$	$-\frac{1}{a} \log(1 - abT e^{ax_p})$
$\frac{a}{b-x}$	$\sqrt{(b-x_p)^2 + 2aT} - (b-x_p)$	$(b-x_p) - \sqrt{(b-x_p)^2 - 2aT}$

Fig. 7.16: Minimum and maximum streak length expressions for different velocity fields

In Fig. 7.16 the tracking for the linear and exponential velocity field is shown for three different exposure times. As discussed in Chapter 3, the exposure time controls the line integral sampling of the velocity field and with smaller exposure time, better tracking is expected and observed. It may be noted that for the linear and the exponential fields, the magnitude of shift from tracking the true velocity increasingly varies with the exposure time. Also, it can be seen that the error remains almost constant for the parameters chosen and the spatial region chosen. This means that for such a situation the relative error actually decreases for a monotonically increasing velocity field (since the denominator keeps increasing).

For the linear velocity field, it may be noted that the performance completely depends on the aT product. It was shown in Chapter 3. that the expression for velocity for spatial averaging in case of linear velocity field is given by $V(x_p) = V(x_p) \frac{(e^{aT} - e^{-aT})}{2aT}$ where the term $\frac{(e^{aT} - e^{-aT})}{2aT}$ contributes to the overestimation error. The variation of this

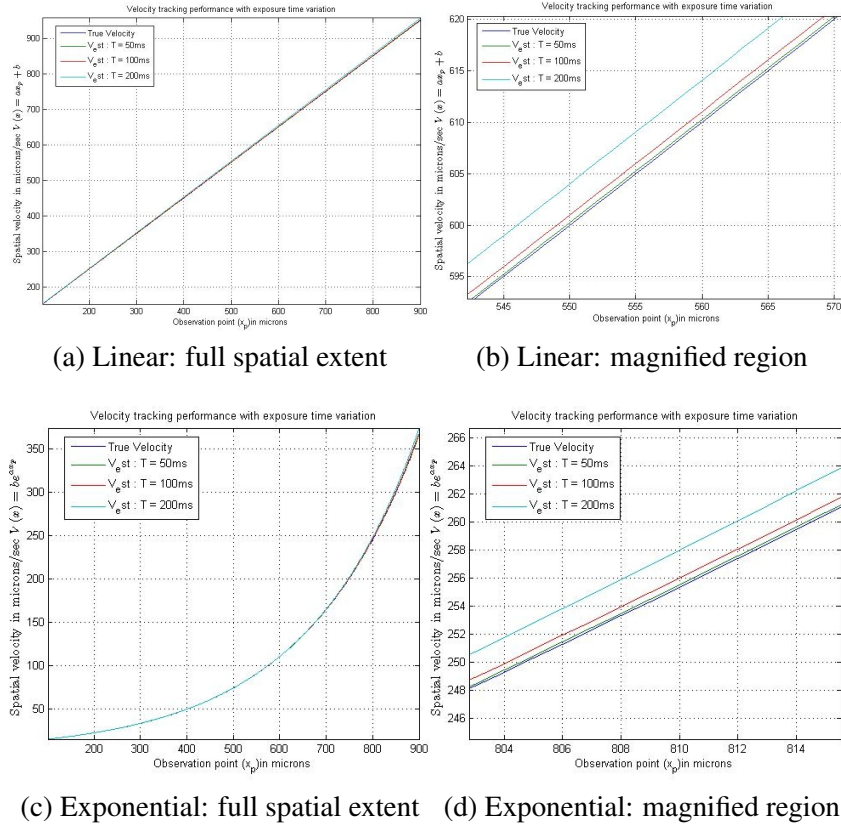


Fig. 7.17: Tracking performance of spatio-temporal averaging for linear and exponential velocity fields.

term is shown in Fig. 7.18. It can be seen that velocity estimation at higher velocity gradients can be successfully done if the exposure time is decreased.

The performance of spatio-temporal averaging for the hyperbolic and sigmoid velocity fields can be seen in Fig. 7.19. It may be observed that the performance of the hyperbolic velocity field is better in the beginning and gradually deteriorates towards the end. The reason for this is because the length expression function sharply varies with the difference $b - x_0$. Earlier, a similar effect was shown for the local linear approximation of a hyperbolic function in an interval at different points in space. The streak-lengths were simulated for the sigmoid velocity field as a closed form expression was not available for L . The trapezoidal rule was used in the GSCI method for streak-length simulation.

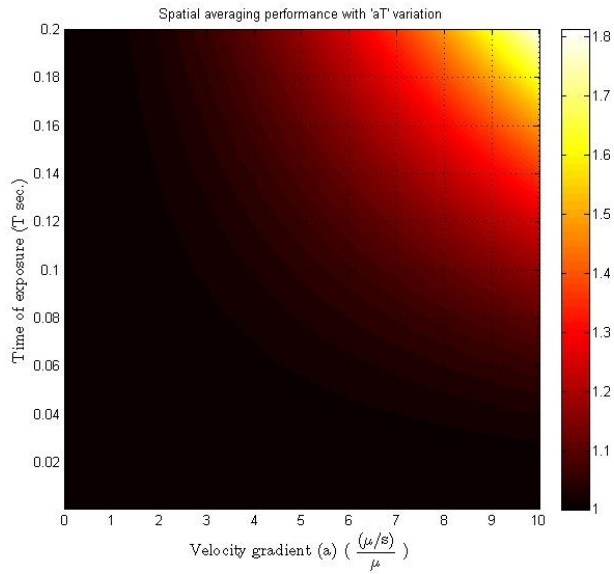


Fig. 7.18: Performance of spatial averaging with variation of the aT product.

7.4.2 Spatio-temporal averaging for 2-D fields

The spatio-temporal averaging for the 2-D fields was done from simulated particle streaks images and the performance. Three velocity fields were chosen and their performances are described below. For each of the fields, about 30 to 50 streaks were observed at each spatial (pixel) position and each pixel was about 0.2 microns. 2-D moving average filter post-processing was done on the estimated vector field components to fill the missing pixels, although the number of such pixels were small (about 1%). The post-processing also imparts some smoothness to the estimated velocity fields.

The first velocity field is the simple case of Poiseuille flow in a channel, where the velocity field is obtained at a horizontal cross-section. This gives the well known parabolic variation of velocity, with the center of the channel at the highest velocity. Apart from its frequent occurrence and being one of the most well studied velocity fields, this flow field has been extensively used for microfluidic velocimetry studies. The results of spatio-temporal averaging are shown in Fig. 7.20. It can be seen that the velocity estimation performance is really good and the relative estimation error is less than 5%. The vertical component is zero

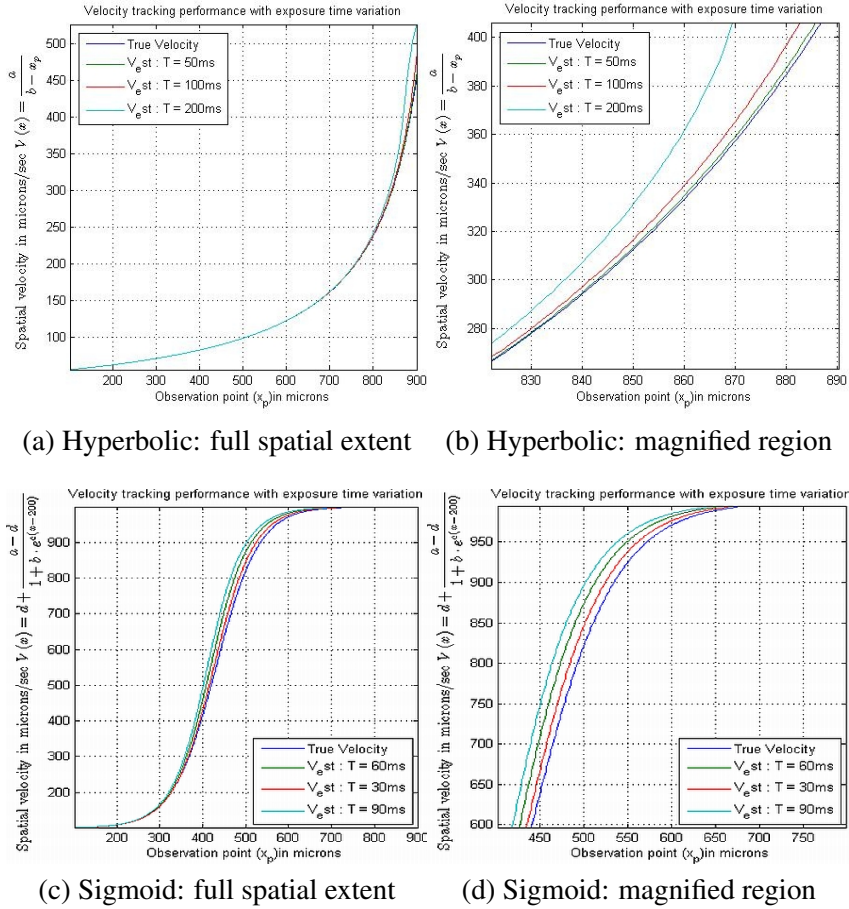


Fig. 7.19: Tracking performance of spatio-temporal averaging for hyperbolic and sigmoidal velocity field

and hence estimation of the horizontal component suffices for this velocity field. Moreover, at every vertical position the velocity is fixed; i.e. uniform across the x direction at that fixed y position. This fact is of particular importance as for our streak-based velocimetry, it means that a streak image would not change in length, or a statistical mean (or median) operation on streak lengths at fixed y positions would yield the velocity. However, this would only be true in ideal cases. When we consider the averaging over the entire spatial extent, streaks would overlap and incorporate incorrect streak lengths to the statistics and bias it toward overestimation. Fig. 7.21 shows the true and estimated vector field components. For the vertical component, the velocity field obtained was actually a constant equal to the

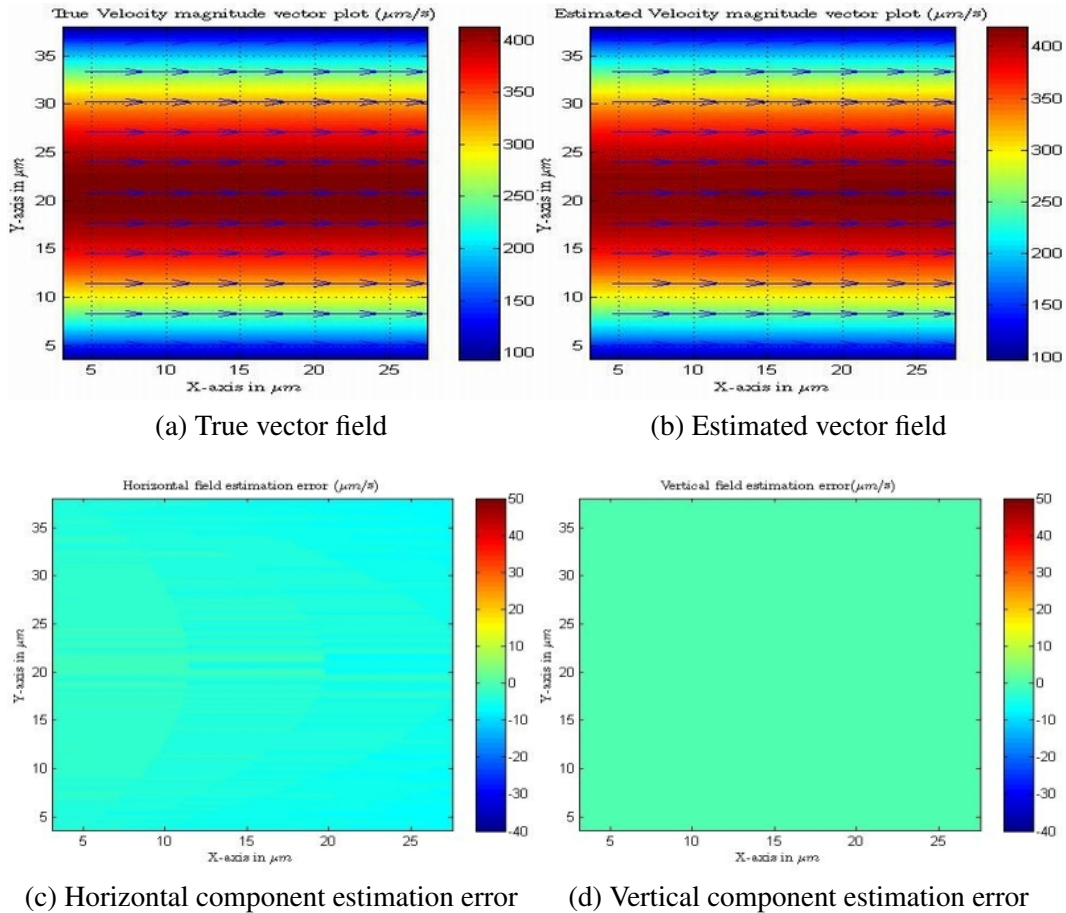


Fig. 7.20: True vector field and component estimation error for Poiseuille flow

width of the bounding box that tightly encloses the particle streak. This width is actually the diameter of the particle and was subtracted out spatially to obtain the zero velocity field. The second velocity field used is the well studied phenomena of the flow of fluid in a rectangular channel with a circular obstruction in the center. The circular obstruction causes the Poiseuille flow to break and separate into two similar flows where the local velocity gradient suddenly changes spatially causing a dip in the local velocity and an increase in the local velocity within regions in close proximity. Note that, the velocity at walls was set at zero while obtaining the velocity field from the CFD tool (COMSOL). Fig. 7.22 shows the vector magnitude plot for the true and the estimated fields. Also, the estimation errors

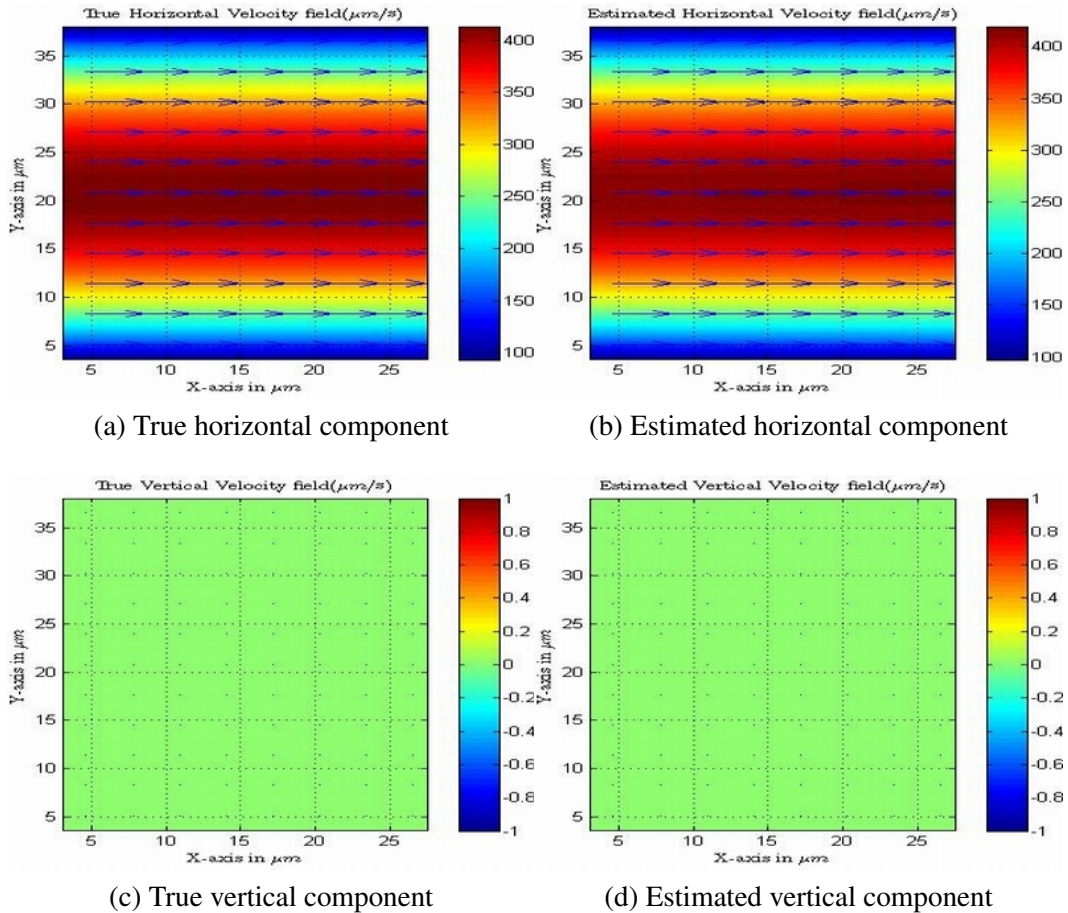


Fig. 7.21: True vector field components and estimated components for Poiseuille flow

for the horizontal and vertical components are shown. Estimation errors are visible for both the field components, but the error magnitude is well within $20 \mu\text{m}/\text{s}$. The relative error can be seen to be larger in the region where the flow separates (and the local gradient is higher) as in this region the velocity magnitude is more comparable to the error magnitude. Fig. 7.23 shows the true and estimated horizontal and vertical components of the second velocity field chosen. The effect of spatio-temporal averaging can be seen in both the components and is more discernible for the horizontal component. Also note that with even larger number of streaks and more efficient post-processing, even better velocity fields can be obtained. The third velocity field was obtained in COMSOL by simulating the physics

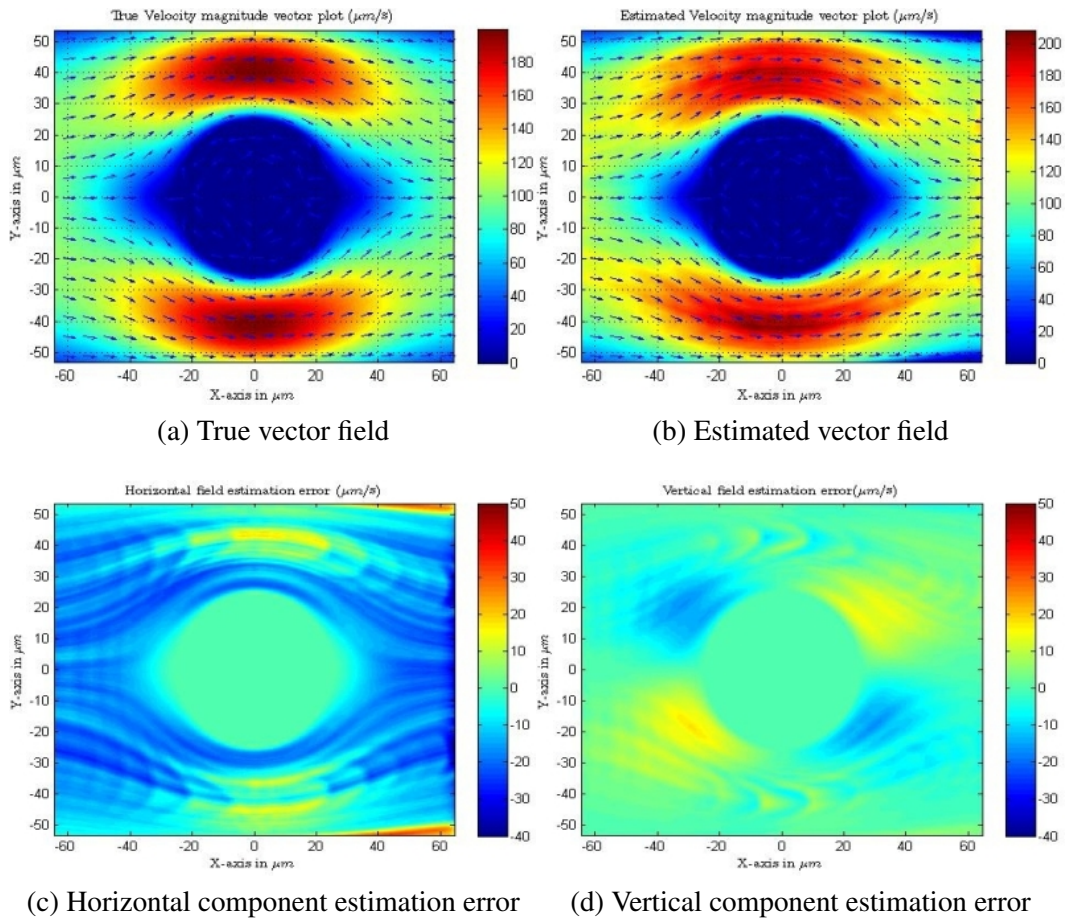


Fig. 7.22: True vector field and component estimation error for steady flow around a cylindrical obstacle

of hydrodynamic flow when a larger channel joins a smaller channel and the ends of the channel are kept at different pressures. Fig. 7.24 shows the velocity magnitude vector plot for the true and the estimated velocity fields. As with our previous velocity field the effect of the spatial averaging can be seen and the velocity contours are not as sharply defined in the estimated field as in the true velocity field. The estimation errors are also shown in the same figure. For some pathlines of the streaks, there appears to be more biasing error (overestimation) due to the streak lengths. Accordingly, features resembling the particle streak pathlines can be seen in the error plots. The magnitude of the relative estimation error is however small and about 10%. The absolute error is higher after the junction of the

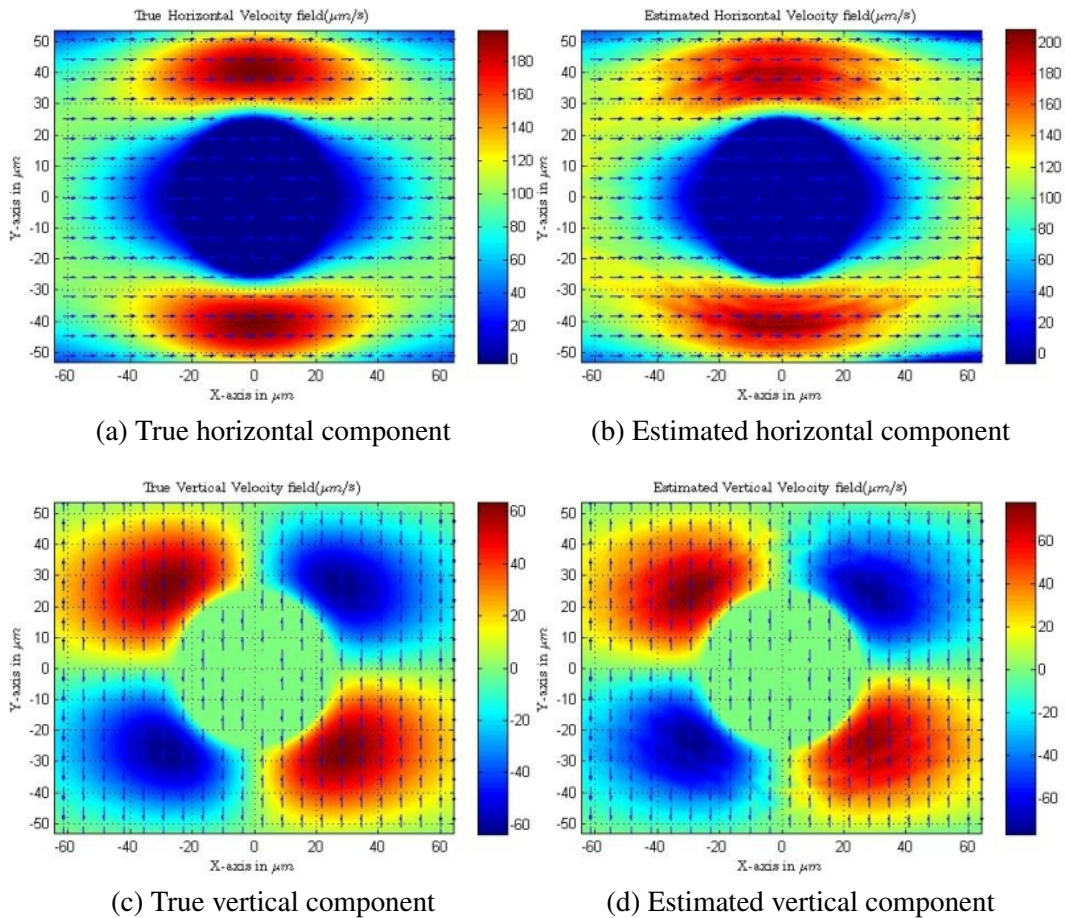


Fig. 7.23: True vector field components and estimated components for steady flow around a cylindrical obstacle

two channels but the channel velocity in the smaller channel is also small. The separation of the two channels is at $x = 0$ and while the true field is extremely symmetrical around the vicinity of this point, the estimated field is not as regular. This can be seen more clearly in the components shown in Fig. 7.25.

7.5 PERFORMANCE OF VELOCITY ESTIMATION BY LOCAL LINEAR APPROXIMATION

The method for the local linear approximation was discussed in Chapter 3 and in Chapter 5. Briefly, for the particle streaks observed at a point in space, the starting position and the length of each streak is recorded, for both the horizontal and vertical directions. Then the

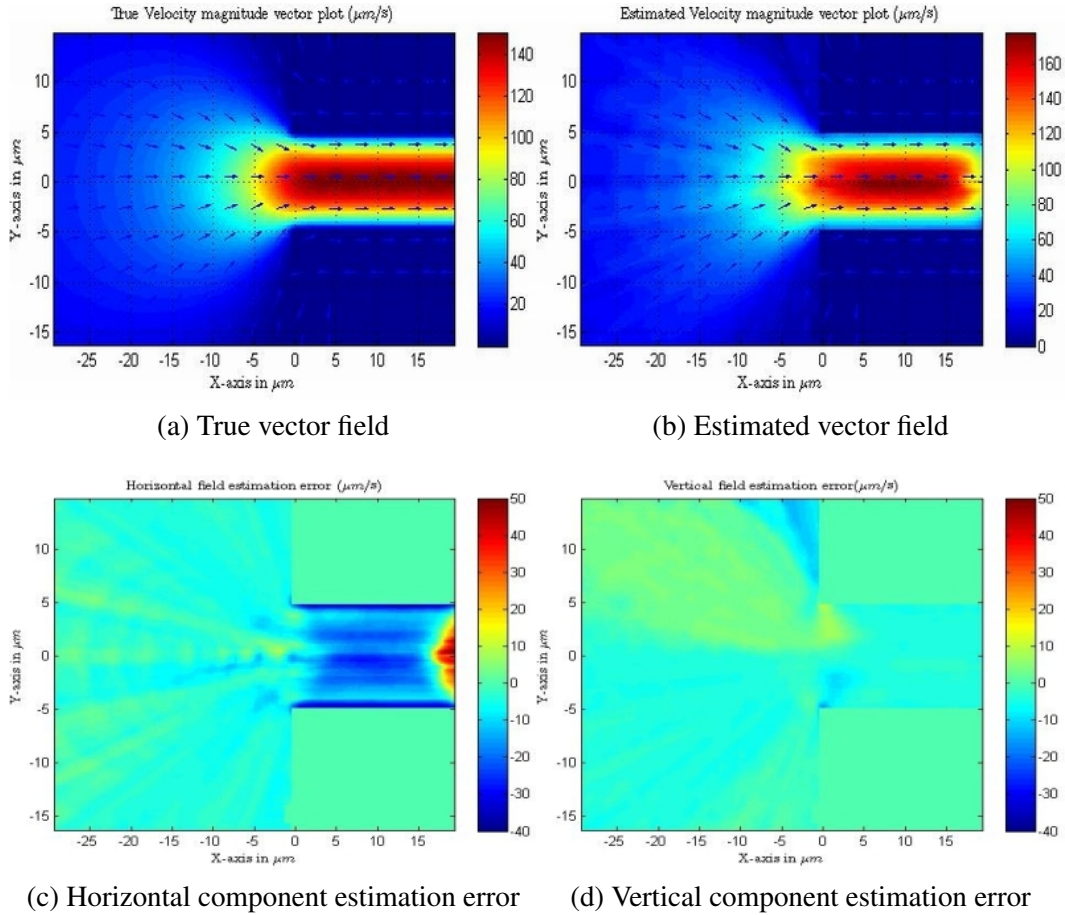


Fig. 7.24: True vector field and component estimation error for steady flow at the junction of two rectangular channels

lengths are corrected for the particle image diameter. The signs on the lengths are obtained by local orientation of the streaks and by knowing the sign on the horizontal component at that pixel. After this the horizontal and vertical descriptor sets (of x_0 and L) are used in a robust linear fitting algorithm to obtain the local linear field parameters. The spatial velocity at a point is then obtained by using these parameters.

7.5.1 Velocity estimation for 1-D fields

For the 1-D field, streak lengths are generated by using either closed form expressions (for linear, exponential and hyperbolic fields) or by the GSCI method (for the sigmoid

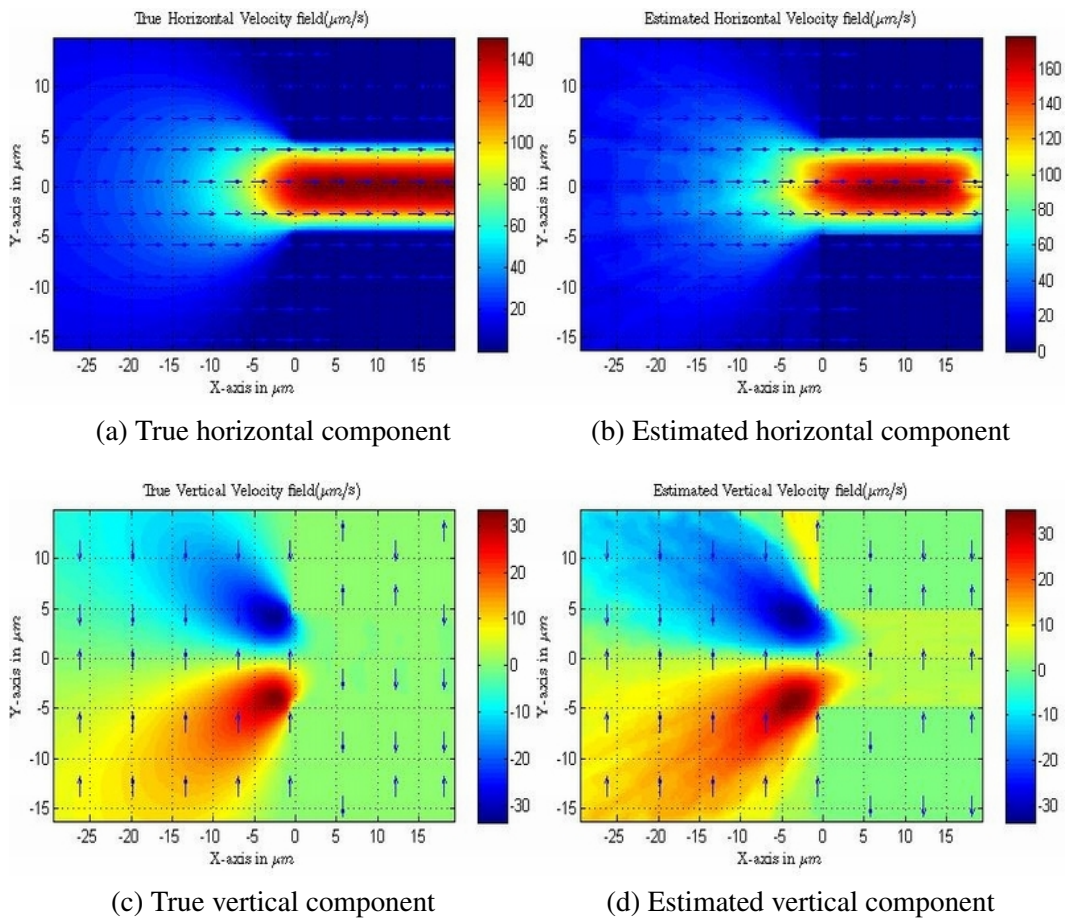


Fig. 7.25: True vector field components and estimated components for steady flow at the junction of two rectangular channels

field). The obtained 1-D descriptors are corrupted by uniform measurement noise varying from no noise to an uncertainty of 0.5 microns. Note that the error is introduced in the measurement since for reasonable SNR particle streak images, the segmentation of streaks leads to distinct streaks and our method is not dependent on the image intensity profile of the streaks but rather on the correct localization of the start and endpoints of the particle streak.

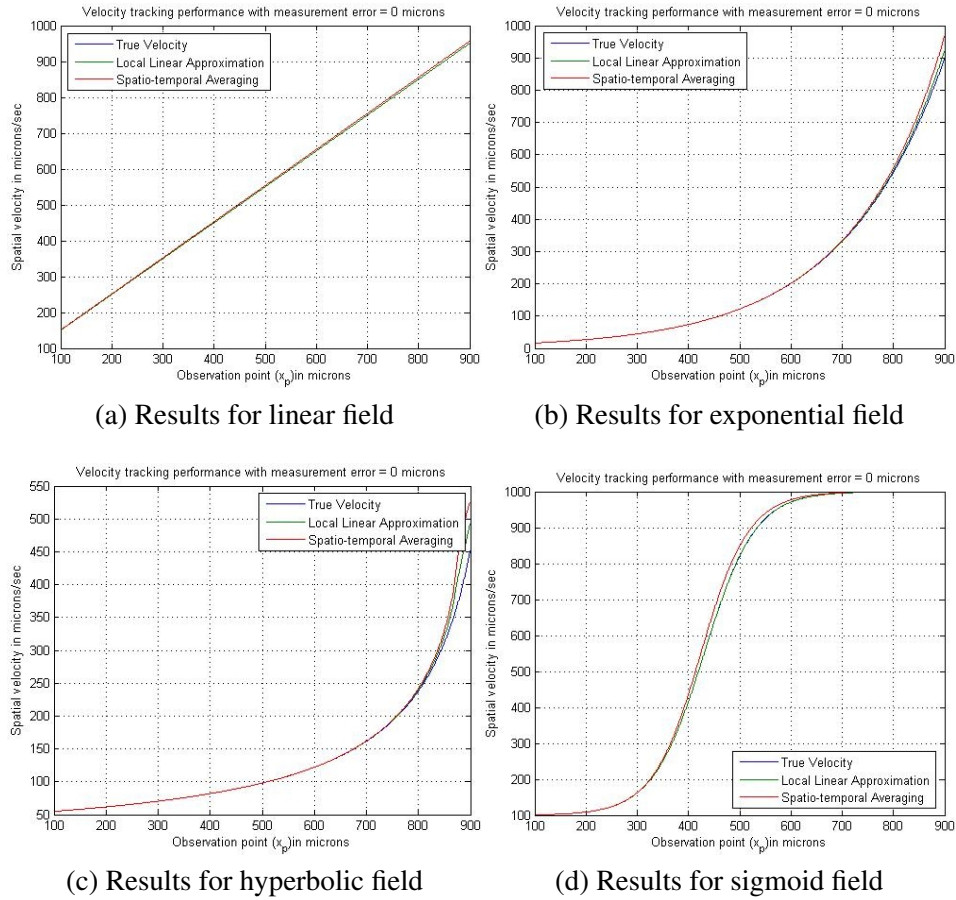


Fig. 7.26: Velocity tracking performance in the absence of measurement error

Qualitative performance in presence of measurement error

The qualitative performance of the local linear approximation based velocity estimation is shown in Fig. 7.26 in the absence of measurement error. To compare the performance of the spatial averaging method, it is also included in the plots. From the plots we find that the spatial averaging method performs well but overestimates the velocity field at higher local gradients, a fact that we have seen earlier. In comparison the local linear approximation method shows excellent tracking performance for all the fields and particularly well for the linear and sigmoid velocity fields. The effect of adding measurement noise of magnitude 0.125 microns is shown in Fig. 7.27. The estimation for the sigmoid velocity field appears

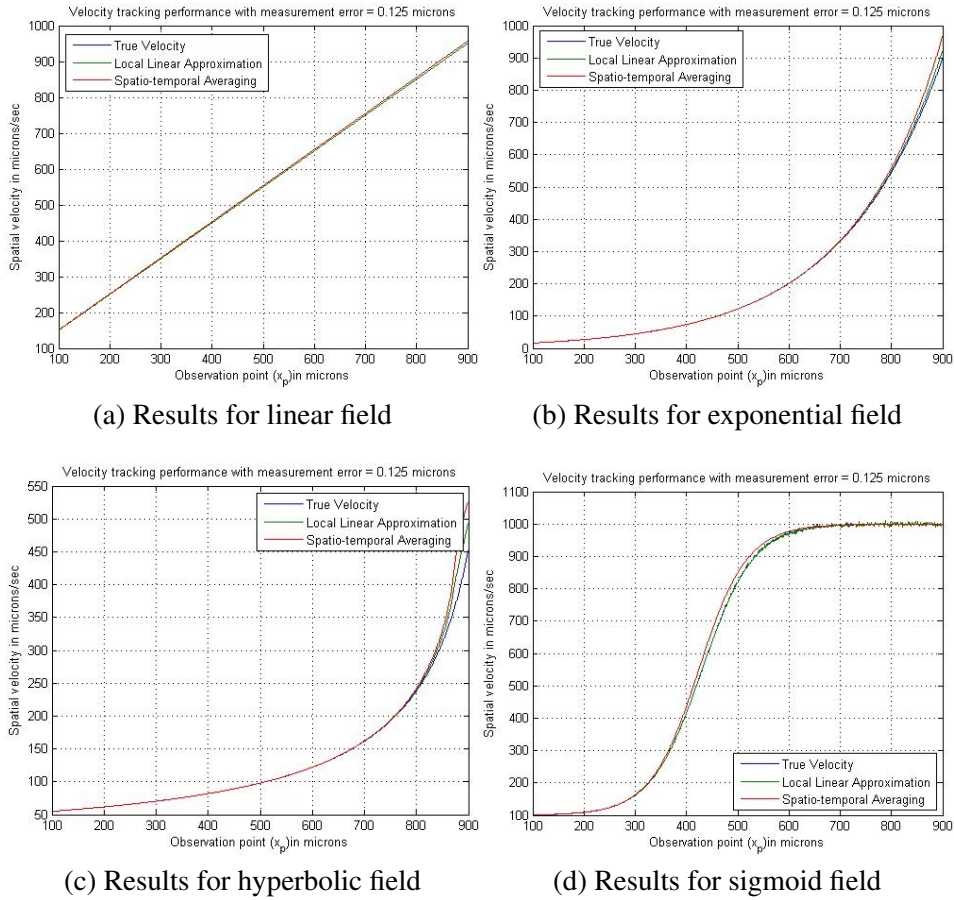


Fig. 7.27: Velocity tracking performance in the presence of a measurement error of 0.125 microns

to be more sensitive to noise than the other velocity fields and this is seen for the other different noise levels also in Fig. 7.28 and Fig. 7.29. Note however that the streak lengths simulated for the sigmoid field were much smaller than those for the other velocity field. This was done to show the importance of having longer streaks. For the linear, exponential and hyperbolic velocity fields, the streak lengths are too large to be adversely affected by noise. The effect of noise is seen to alter the performance of the sigmoid velocity field so much in Fig. 7.29 that the spatial averaging performs equally well in comparison. Thus the presence of measurement noise would deteriorate the performance of the velocity estimation and more so if the amount of measurement error is considerable compared to the length

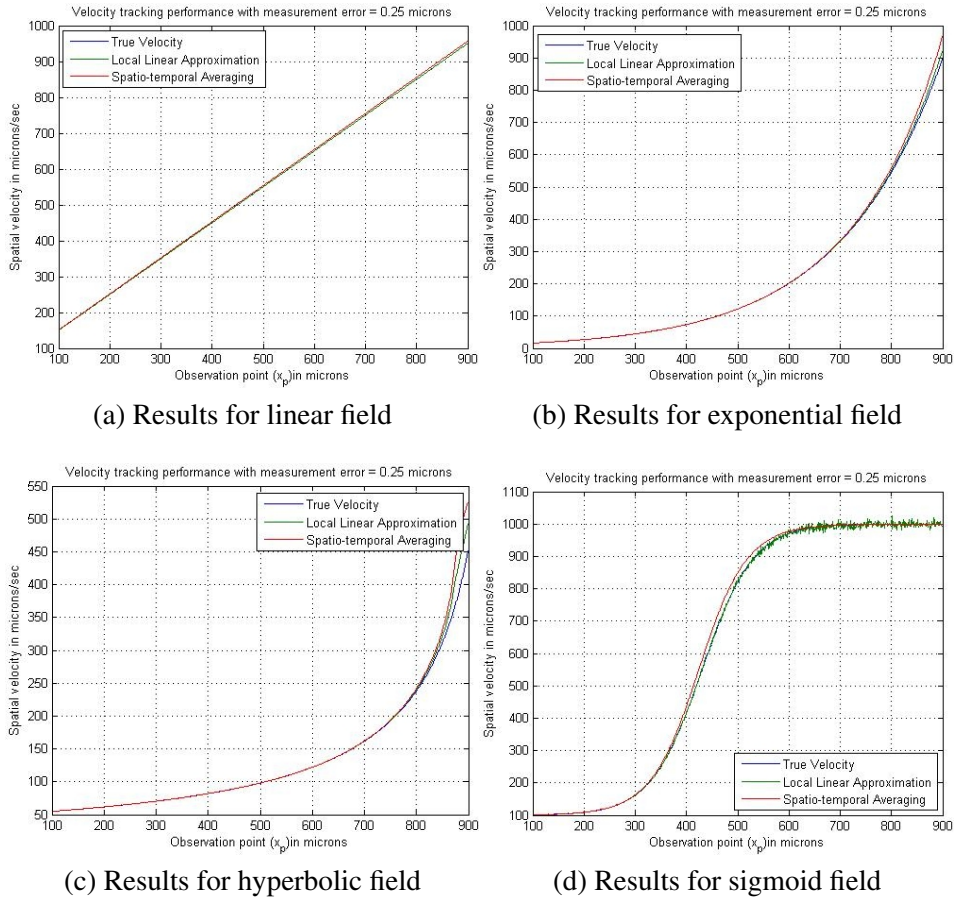


Fig. 7.28: Velocity tracking performance in the presence of a measurement error of 0.25 microns

of the shortest streak length for the system. This in turn is dependent on the exposure time and the local velocity field.

Estimation error performance in presence of measurement error

A quantitative study on the estimation error performance is done for different levels of measurement noise. As noted earlier the effect of the measurement error is stronger if error is significant compared to the least possible particle streak length. Now if we consider a vector field that is monotonically increasing, the particle streak lengths would also increase monotonically. Hence the effect of measurement error would reduce at larger local veloc-

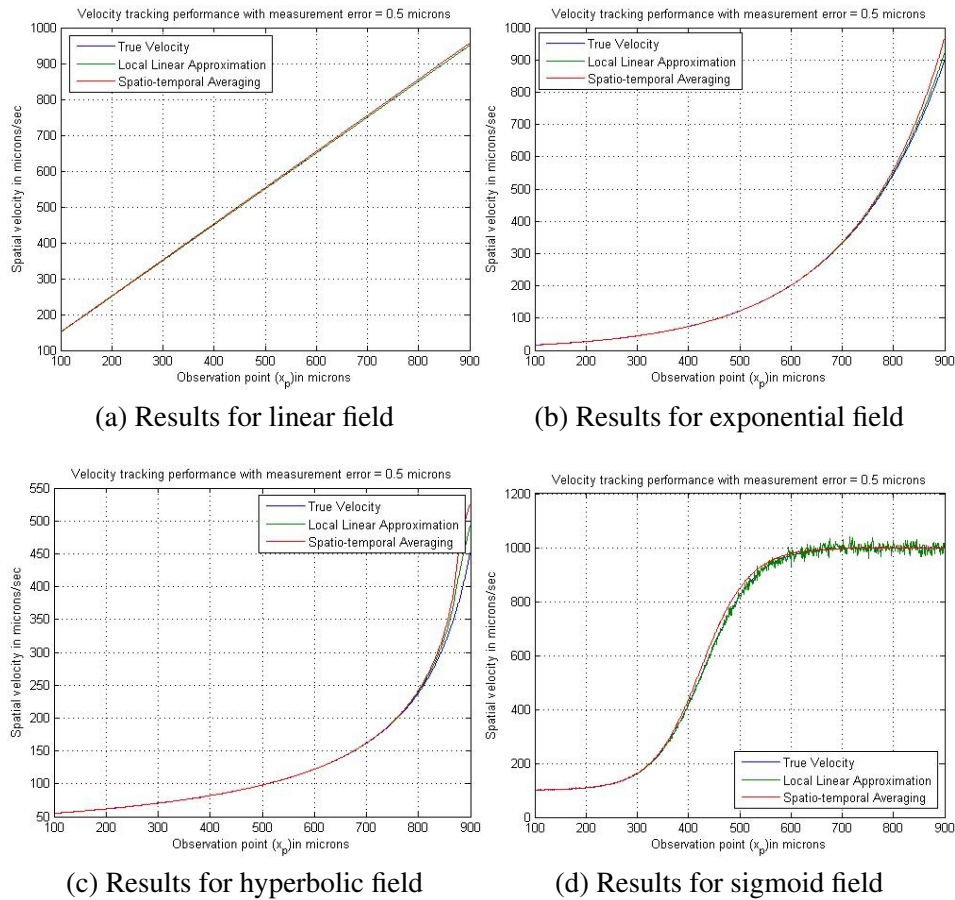


Fig. 7.29: Velocity tracking performance in the presence of a measurement error of 0.5 microns

ities. The relative error performance is shown for no measurement error in Fig. 7.30. As expected the local linear approximation gives zero relative error for the linear field while for the spatio-temporal averaging method, there appears to be a finite, spatially constant relative error. The error is however not constant for the other 3 fields and varies with the spatial position. In the case of the exponential and hyperbolic fields, the error increases with the increase in the local velocity. It can be seen, that while the relative error for the exponential field is less than 10% for both the local linear approximation and averaging methods, the error is much larger for the hyperbolic velocity field. The increase in the relative error is caused by the increase in the streak lengths over a region which cannot be modelled at that

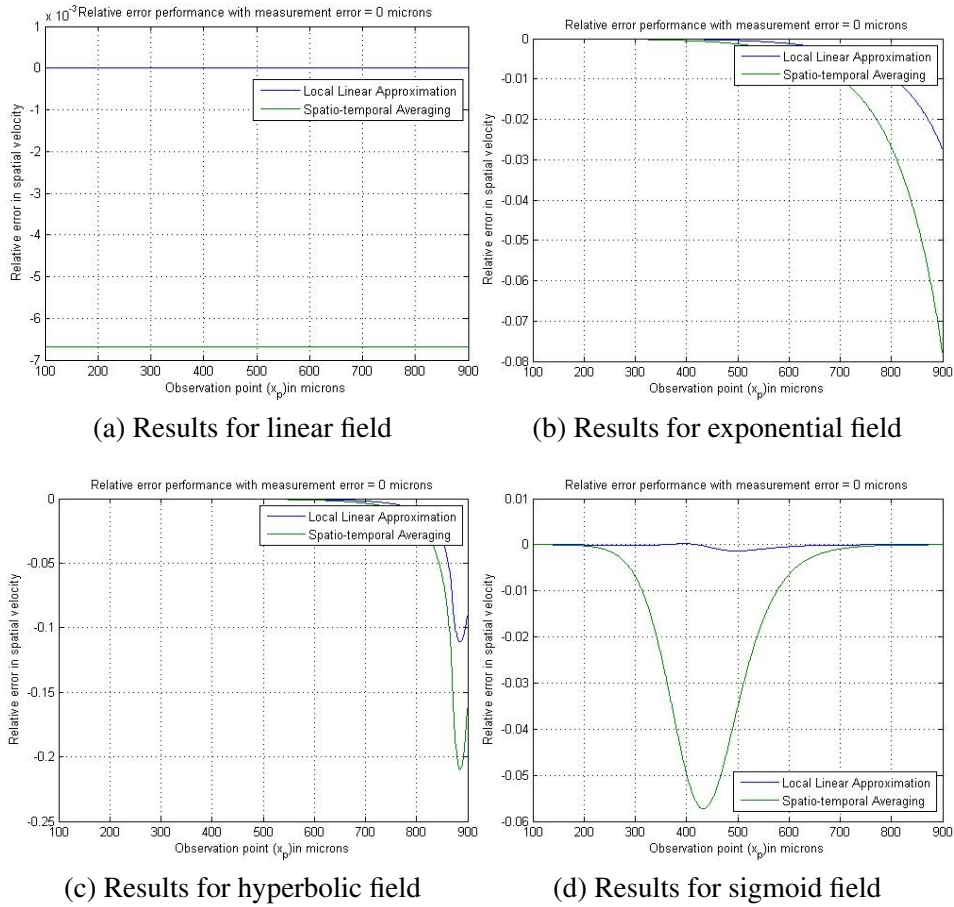


Fig. 7.30: Relative error performance in the absence of measurement error

due to a linear velocity field. Hence it is essentially a model mismatch error which eventually leads to overestimation error. In case of the sigmoidal velocity field first the streak lengths keep increasing and the model mismatch error increases and then at the inflection point the model mismatch error starts to decrease. However the effect of model mismatch is minimal compared to the overestimation error observed for spatio-temporal averaging. The effect of measurement error is added over the model mismatch error and the effect of noise can be seen in Figs. 7.31 to 7.33. The measurement error performance is consistent across different levels of noise. For the linear field, the noise is more significant in the beginning part when the particle streak lengths are shorter. As the velocity increases, the particle track length also increases, thus making the measurement error insignificant compared to

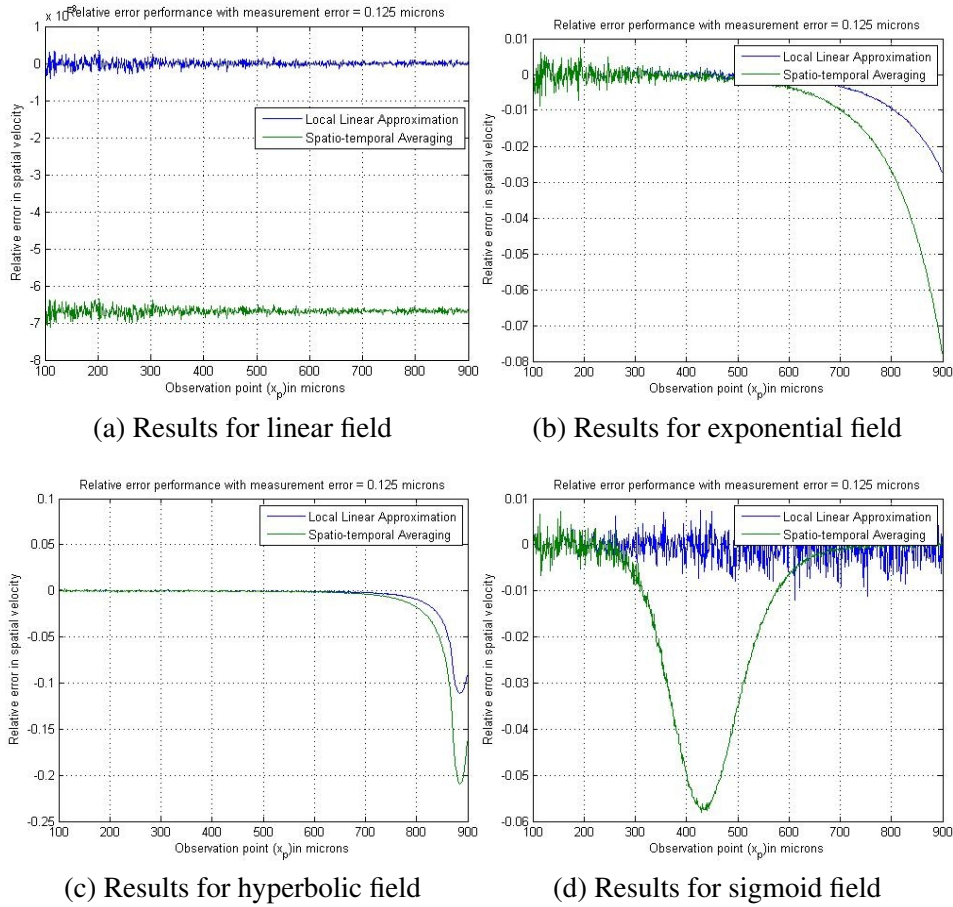


Fig. 7.31: Relative error performance in the presence of a measurement error of 0.125 microns

the streak length. The exponential velocity field shows this effect even more prominently, as towards the end of x-axis, it appears as if there is no noise in the measurements. It may be noted that the variation of the noise is small compared to the error introduced due to model mismatch. The sigmoid velocity field shows contrasting performance for the local linear approximation method and the spatio-temporal averaging. For the former, the effect of measurement noise appears to increase with increasing velocity while for the latter, it decreases. Also, as observed earlier during tracking performance, the sigmoid velocity field is the most affected by noise alone, if we do not consider the model mismatch error. Again it needs to be pointed out that a part of this is because the streak lengths selection was much

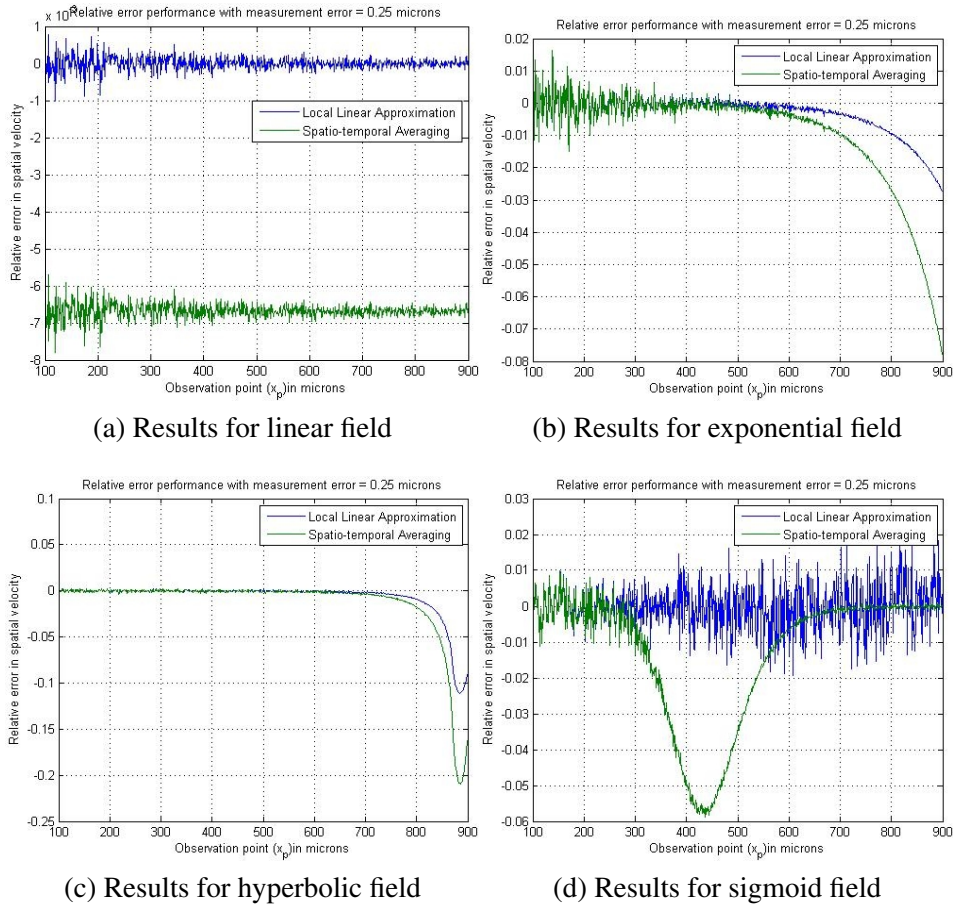


Fig. 7.32: Relative error performance in the presence of a measurement error of 0.25 microns

smaller. The performance of the hyperbolic velocity field appears to be the least affected by the measurement error. For the beginning part of the spatial extent the hyperbolic field resembles a linear field very closely and hence the model mismatch error is minimal. Later, when the model mismatch error is high, so are the streak lengths, thus dominating the insignificant measurement noise. The spatial change in the relative signal to noise also causes the measurement error noise to decrease in the case of spatio-temporal averaging. At lower velocities, the streak lengths are shorter and the noise can be comparable. When averaged, the noise reduces but the signal increases. At higher velocities, the signal increases by even larger amounts during the spatial averaging process, thus reducing the noise even further.

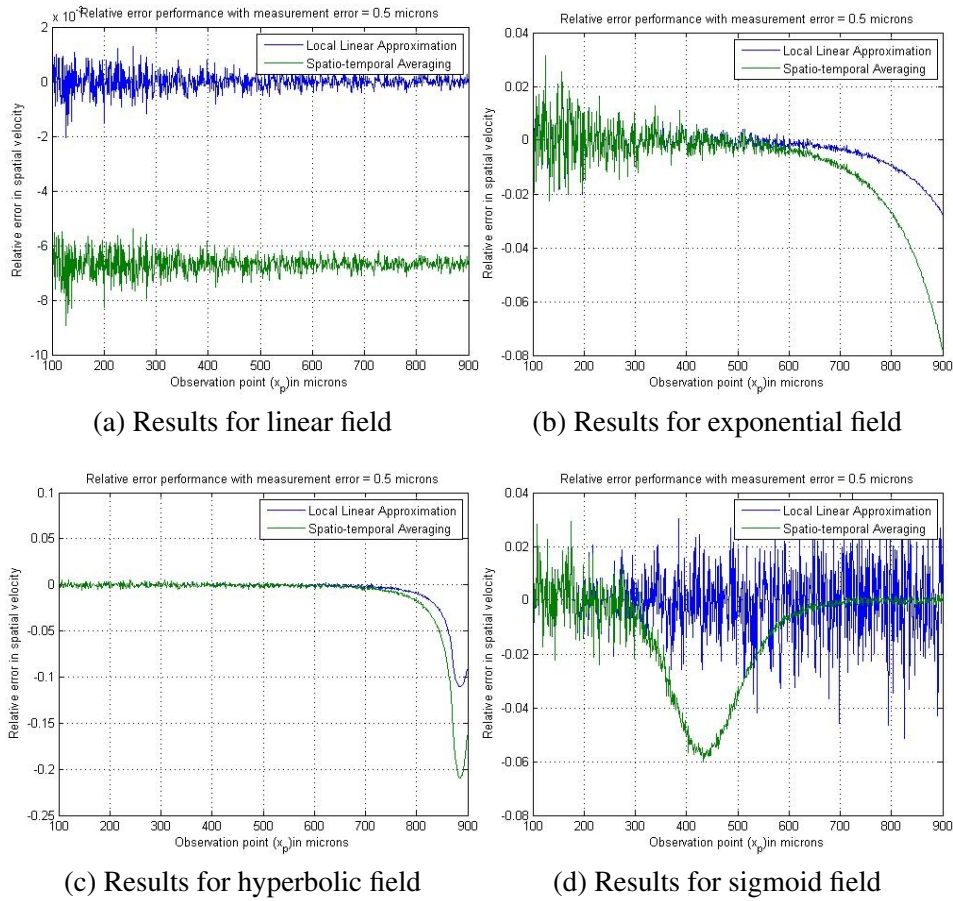


Fig. 7.33: Relative error performance in the presence of a measurement error of 0.5 microns

7.5.2 Velocity estimation for 2-D fields

The performance analysis of the velocity estimation for 2-D fields is done using the same 3 velocity fields that were discussed earlier. These are the Poiseuille flow, the steady flow around a cylinder and the flow at the junction of 2 rectangular channels. In all three cases, a pressure difference between the inlet and outlets creates the flow. COMSOL Multiphysics is used to first compute the flow fields and then this is used in the streak image generation framework. The simulated images are then used to obtain the velocity field back from the images. The first step is the image processing step, where the streak images are segmented and the streak descriptors (start position and length) are recorded. The next step is the

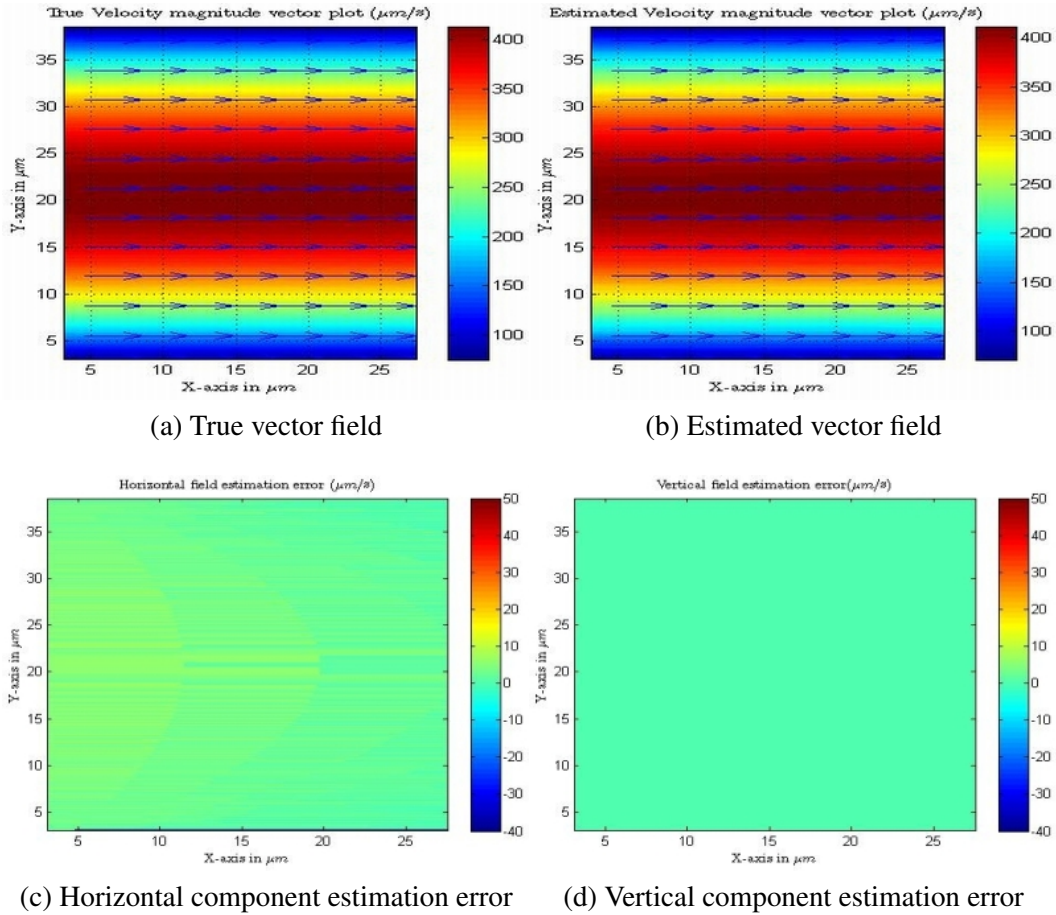


Fig. 7.34: True vector field and component estimation error for Poiseuille flow

local linear approximation step where the streak descriptors at a spatial position are used to obtain the local parameters.

During the estimation process, 2000 frames were used and about 30 to 50 streaks were observed for each spatial location. The actual number of usable streaks varied between 20 to 30 approximately for each spatial position. The reduction in the number of streaks was from overlapping streaks that were eliminated. Note that some number of overlapping streaks are expected in the actual experiments also and the algorithm processing the corresponding streak lengths removes such overlaps as outliers during the robust fit. In some extreme cases, the outlier reduction reduces the statistical strength considerably and

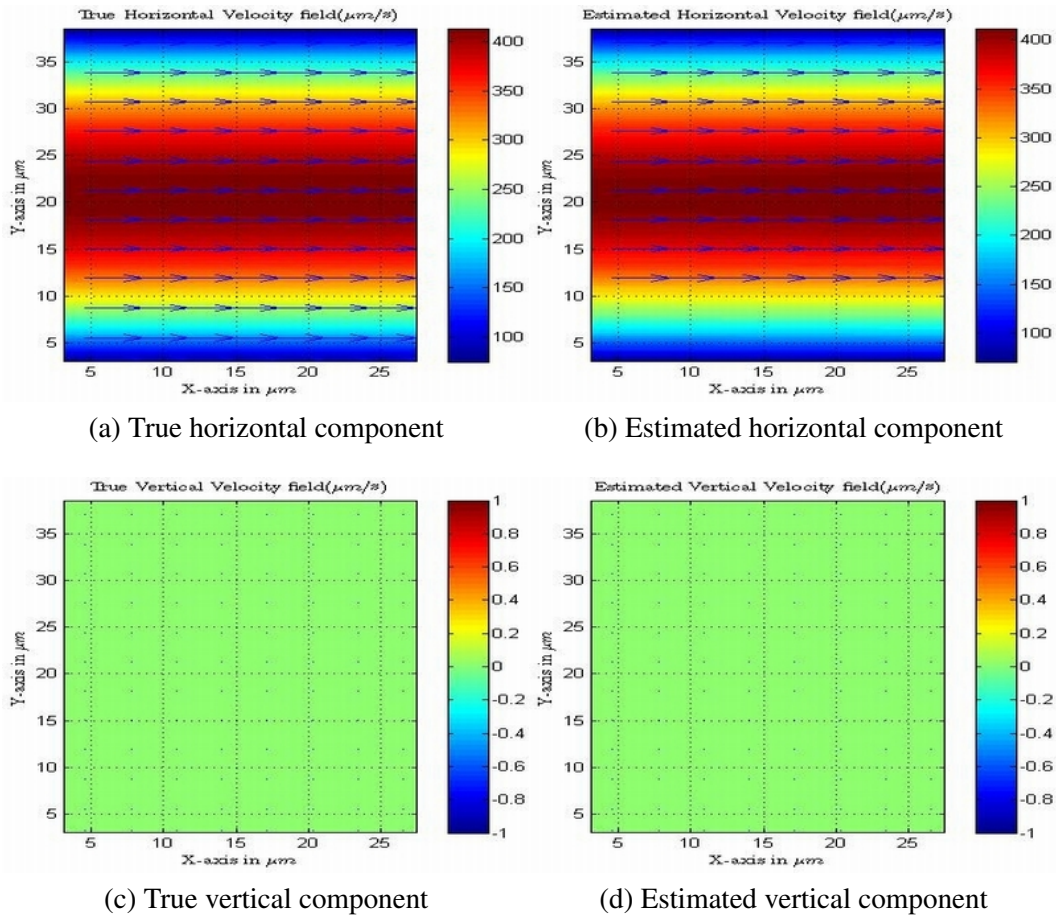


Fig. 7.35: True vector field components and estimated components for Poiseuille flow

in these cases, the spatio-temporal mean is used for that position. In the end the primary velocity field component so obtained is smoothed by a local moving average filter (averaging region is a square, with 7 pixel sides) to get the final velocity estimate.

The results for the local linear approximation method is shown for the Poiseuille flow in Fig. 7.34 and Fig. 7.35. The estimation performance is very good and this is expected for a simple velocity field with zero vertical component. Note that the performance of the spatial averaging method and the local approximation method are very similar for this velocity field, as the local approximation method reduces to finding the local spatial mean, since there is no gradient and the flow is uniform in the horizontal direction if we

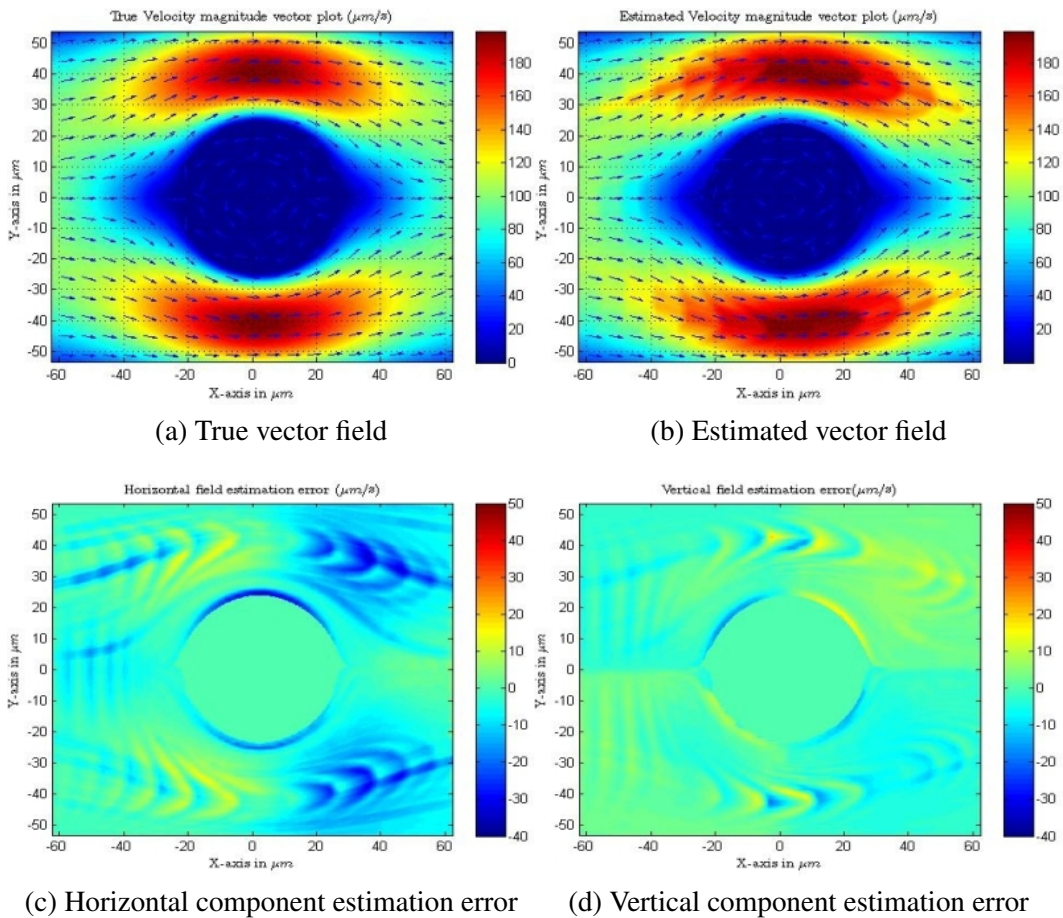


Fig. 7.36: True vector field and component estimation error for steady flow around a cylindrical obstacle

consider a fixed point in the vertical axis.

The performance for the flow around a cylindrical obstruction is shown in Fig. 7.36 and Fig. 7.37. In the first figure, for the magnitude vector field plot, it can be seen that the field estimated resembles the true field closely. However it differs from the true field by the presence of slightly bolder demarcation contours at points where the velocity changes. This can be attributed to the absence of a sophisticated smoothing or fitting post-processing step. The particle streak lengths change discretely while the actual velocity transitions occur more smoothly. This gives rise to more pronounced velocity zone demarcations. While smoother velocity field components can be obtained by better smoothing and (or) surface

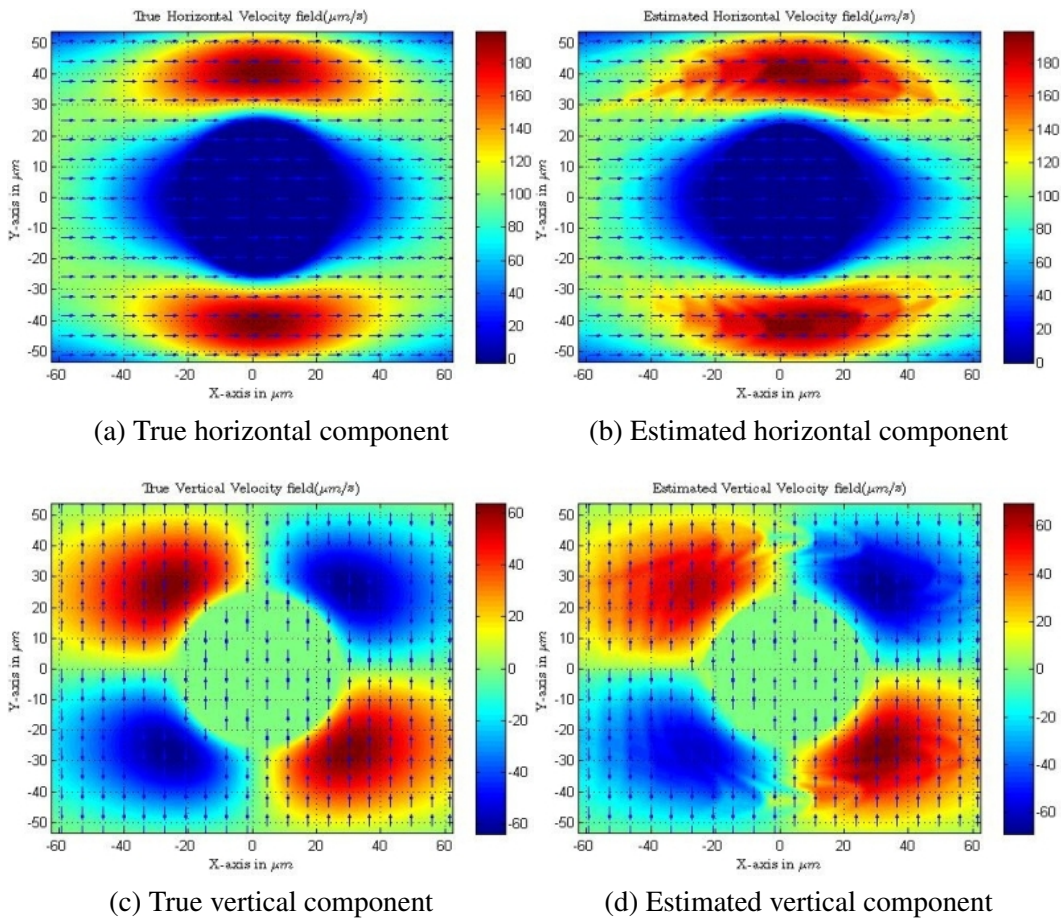


Fig. 7.37: True vector field components and estimated components for steady flow around a cylindrical obstacle

fitting methods, this is left as future work.

An interesting observation from Fig. 7.36 is the presence of contours which shows the group movement of the particle streaks and some streamlines. These are artefacts of the current implementation of the algorithm, which is extremely local and does not incorporate any smoothing during the local velocity estimation. Another observation is the change in the nature of the errors on the inlet and outlet side. While the magnitude of the error is same the signs are different and this is due to the nature of the velocity gradient experienced by the streaks and the corresponding effects on their lengths. Note however the relative error is small as the local velocities are considerably higher than the error magnitudes.

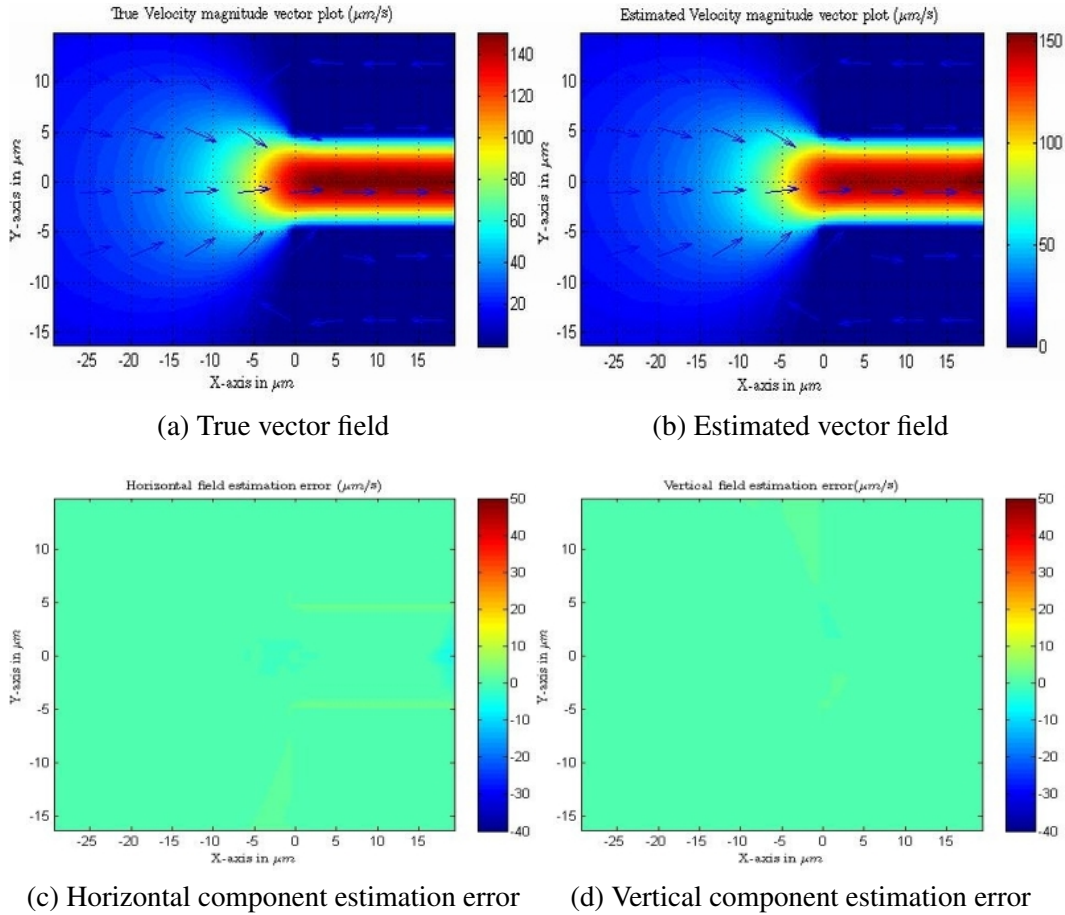


Fig. 7.38: True vector field and component estimation error for steady flow at the junction of two rectangular channels

The performance for the third velocity field is shown in Fig. 7.38 and Fig. 7.39. The estimated vertical and horizontal components are seen to be very similar to the true components. The relative error magnitude is also small for both the components and less than 10% on average. Consequently, the magnitude vector plot for the estimated field appears to be almost identical to the true velocity field.

Compared to the spatio-temporal velocity estimation method the local linear approximation based method has lesser overestimation and underestimation errors. The results for both methods are almost identical for the Poiseuille flow, while for the last velocity field, the performance of the local linear approximation is better. For the flow with cylin-

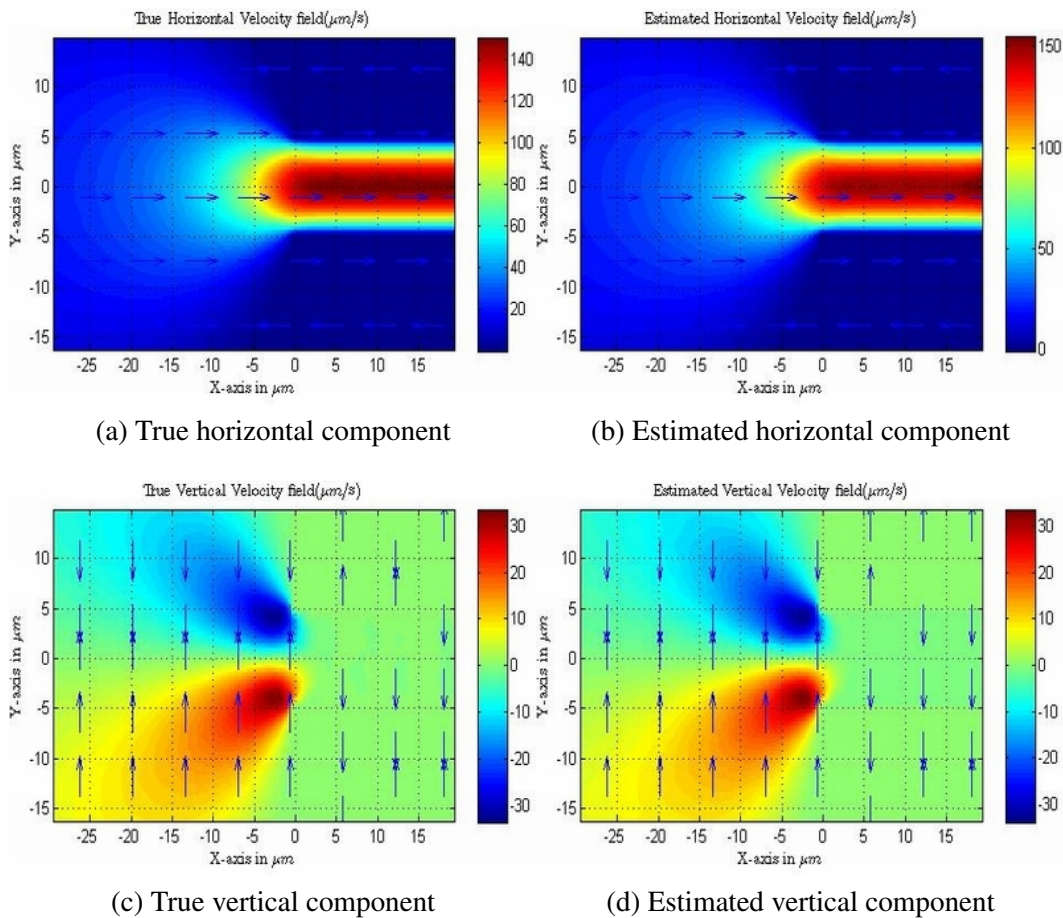


Fig. 7.39: True vector field components and estimated components for steady flow at the junction of two rectangular channels

drical obstruction, both methods show some degree of error.

When we consider the three test velocity fields that were used, it may be noted that the first represented a case of uniform velocity, the last a case of increasing velocity gradient and the second, a case which had both positive and negative velocity gradient, and the proposed methods resulted in high quality velocity estimates for all the methods. Our target was to show that particle streaks could be used to determine velocity fields and we have shown that both the spatio-temporal and the local linear approximation based methods can be used to characterize and estimate the velocity field. The velocity estimates are quite accurate and the local fields can be as resolved as the dimensions of the particle images. The

main advantage of our method is the use of low speed imaging devices, consequently the exposure times for our method are in the order of tens of milliseconds which is way higher than that used for PIV. Further improvement of the accuracy by smoothing and surface fitting and measurement error reduction will be the topic of our future work.

CHAPTER 8

MERITS AND LIMITATIONS OF THE PROPOSED METHODS

Image based velocimetry for microfluidics is a research area that has been widely popular over the last decade and a vast array of methods have been proposed. Each of these methods have their own merits and limitations of their applicability. The analysis methods that have been proposed here are no exception and in this chapter we list some of the major merits and limitations of the methods. Moreover we also discuss the advantages and drawbacks of the simulation framework that was also proposed in this dissertation.

8.1 MERITS OF THE μPSV METHOD

Some of the merits associated with the μPSV method originate from the fact that it falls in the PTV class of image based velocimetry methods. The other advantages arise from the analysis strategies, correction methods and due to the directional nature of a particle streak.

8.1.1 The PTV connection

In spite of being related, the proposed μPSV method has some major differences with common PTV implementations. However being related to PTV automatically provides our method with two distinct advantages. First is the resolution aspect of the estimated velocity field. The resolution for the standard μPIV is essentially limited by the 2D cross-correlation block size. Note that this has to be considerably larger than the dimension of a particle, since groups of particles need to be analyzed. For PTV and the proposed method the velocity can be localized within the particle streak extent naturally leading to highly resolved velocity estimates. Secondly, 3D velocity estimation over a microchannel volume is possible with the use of multiple cameras. Since it is much easier to track a single particle and even simpler to track a particle streak (compared to a group of particle as in PIV), the proposed method is well suited for 3D velocimetry.

8.1.2 Improvisations over PTV

It was mentioned earlier that the proposed μPSV method does not incorporate the tracking aspect (a major difference from PTV). Thus the particle association problem linked with PTV does not manifest, and we simply work with the particle streak endpoint locations.

By avoiding the association problem the processing time is reduced, and false association errors are also avoided. However, the incorporation of tracking would definitely help the estimation, and intuitively, it is much easier to associate streaks than particles. This fact has been utilized in most of the work where streaks were used for tracking.

Another aspect of PTV which is improved in the proposed μPSV method is that the required post-processing interpolation is minimized considerably since every point on the spatial extent of the streak is utilized. Usually the dimension of streaks is large compared to a solitary particle image. Hence a streak covers more spatial area than particles and with a sufficiently large number of streaks, no additional interpolation would be required after spatial velocity estimates are obtained.

8.1.3 Improvised point estimates

A corrective strategy was suggested in Chapter 3 to improve point assignment. For small scale (irregular) use of particle image based velocimetry, manual tracking is often the method of choice. Even if we assume that the degree of error contributed by the human error aspect and the software used to locate endpoints or centers is minimal, the typical method of center-point based velocity assignment adds error which increases with the local gradient of the velocity field. The corrective method can improve the velocity estimates for manual tracking.

8.1.4 Quick 2D2C velocity estimation by spatio-temporal averaging

The collection of streak lengths can be used efficiently for a quick 2D2C velocity estimation simply by assigning the streak length over the spatial extent of the streak in a frame and then performing a temporal average at each spatial location. We have shown earlier that for uniform and piecewise uniform fields this would give very accurate estimates and for fields with small local gradients, the errors would still be minimal. Moreover, with a sufficient number of streaks (spatial coverage) there would be no immediate need for spatial interpolation. It may be noted that neither PIV or PTV can have an analogous method owing to their dataset of point particles.

8.1.5 *The local linear velocity model*

The local linear assumption results in two major advantages for the proposed method. Firstly, it brings in a model-fitting perspective to the velocity estimation process. The closed form expressions that are obtained by this assumption result in a more disciplined and structured use of the acquired data (spatio-temporal streak descriptor table). Secondly, the local linear assumption incorporates the gradient aspect of the underlying Eulerian field within the estimation strategy. Hence it is well suited for fields with gradients. It may be noted that in the case of a velocity field ROI which is almost linear, the method would be extremely accurate.

8.1.6 *Implicit visualization of pathlines*

Particle streaks are themselves images of the tracer particle pathlines. There is no need to join particle centroid locations as in the case of PTV. Moreover streaks convey direction and makes it easier to join streaks of the same particle. For a time-invariant velocity field, the pathlines represent streamlines. Thus a projection of pathlines (obtained over time) would distinctly show the streamlines for the velocity field which is very useful information. Time lapse videos of streamlines can reveal if a velocity field is actually time invariant.

8.2 MERITS OF THE PARTICLE STREAK SIMULATION FRAMEWORK

The method for generation of particle streaks videos from CFD data is a new technique that generalizes the use of CFD data for visualization and baseline data generation. By changing the simulation parameters (e.g., exposure time) we can generate ideal experimental data under a wide range of experimental conditions for a velocity field that is user designed. Coupling this with CFD tools like COMSOL, that allow the user to design and simulate multi-physics experiments and obtain idealized estimates of resulting velocity fields, the experimenter can actually perform a virtual experiment. The generated simulation images would not only help provide baseline data for algorithm development, but also aid in making decisions about key experimental parameters like seeding density without doing the actual experiments, thus decreasing the time for a successful data acquisition.

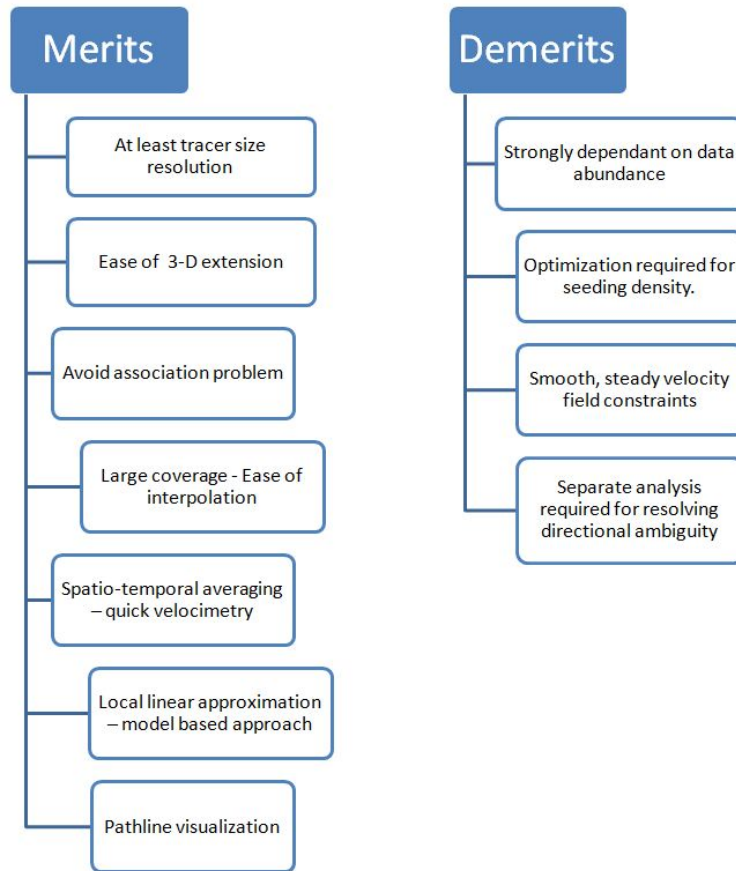


Fig. 8.1: Merits and demerits of the proposed method

8.3 LIMITATIONS OF THE μPSV METHOD

The main limitations of the proposed method in its current form of implementation arise due to the requirement of a large number of sharp distinct streaks. The other limitations arise due to the constraints on the validity of the local linear assumption and due to the nature of the particle streak.

8.3.1 Performance dependence on data abundance

Evaluation of the local gradient parameter is based on robust least-squares fitting, the accuracy of which improves with more data. Moreover, a larger dataset implies a larger coverage of the ROI. Hence the accuracy and the spatial extent of velocity estimation for our method

is highly dependent on the spatial data density; i.e., how many streaks a point ‘observes’ over time. Hence a large number of image frames are normally required which can increase processing time and storage space requirements. However, obtaining faster processors and a relatively large secondary memory is not difficult and cheap compared to faster image capture hardware.

8.3.2 Selecting the right seeding density

The trial and error involved with the selection of correct particle density is a limitation associated with PTV and by virtue of its relationship, the proposed method. There is no direct quantitative formulation that can compute an optimal seeding density. However, one can use the particle streak simulation framework to obtain a closer estimate of the seeding density before venturing into an actual experiment to identify an acceptable seeding density. It may be noted that an optimal seeding density that does not cause considerable overlapping would also lead to a smaller number of frames that would be required.

8.3.3 Resolving directional ambiguity

While a particle streak is inherently directional, it is impossible to discern the actual direction from a single image frame due to a 180 degree directional ambiguity. The proposed method does not inherently deal with directional ambiguity and this is resolved as a separate step in the image processing part. In comparison, the cross-correlation method of μPIV gives the displacement direction along with the magnitude.

8.3.4 Smooth, time-invariant velocity field constraints

In this work, the proposed methods are all based on smoothness and time-invariance assumptions about the velocity vector field. The streak length modelling is based on a local linear field approximation which is only possible for a smooth velocity field. Hence the applicability of the proposed methods is limited to smooth velocity fields only. However, if we use the methods only for microfluidic studies, then the assumptions are often favorably satisfied (with small errors), owing to the small Reynolds numbers associated with small device dimensions in microfluidics.

8.4 LIMITATIONS OF THE PARTICLE STREAK SIMULATION FRAMEWORK

The particle streak simulation framework still suffers from large computational time problems with the increase of resolution. While this is completely natural, code vectorization as well as a multi-processor targeted programming could hugely affect the speed of image sequence generation. Secondly, the inclusion of detailed physics and non-ideal structure for the particles would make the simulations much more realistic while still maintaining the gold-standard.

CHAPTER 9

APPLICATIONS

The work in this dissertation was a result of investigating the possibility of using particle streaks to measure velocities for an electrokinetic experiment in a microchannel. In general however, the velocimetry method proposed is quite generic and can be used for many applications where μPIV can be used, the main constraint being the ability to control the exposure time of imaging. Many of the recent applications of μPIV have been discussed in the reviews by Lindken et al. [3], Williams et al. [12] and Wereley et al. [11]. In this chapter, we discuss how micro particle streak velocimetry can be advantageous in cases of known velocity field types and then discuss experimental results obtained for some experiments conducted in glass and polymer based microfluidic devices.

9.1 ESTIMATION OF KNOWN VELOCITY FIELDS

In Chapter 3, a local linear model of velocity field was used to obtain the length of the particle streaks in the velocity field. The same method could be used for cases whenever the velocity field is known beforehand and the particle length can be independently expressed as a function of the other parameters. This is however not always true, even for simple velocity fields. For example, the sigmoid function finds use in many situations where there is a gradual (damped) non-linear, smooth change from one distinct constant level to another. Similar situations can arise in microfluidic velocity fields; e.g., where channels connect and pressure differences occur. However, the sigmoid function leads to an expression for the streak length L , which is non-linear in L and is not very useful. In such cases often the local-linear approach with good control on exposure time may outperform a strategy of parameter estimation by curve fitting methods. With this caveat on the attempt to mathematically model streak lengths for any known (closed-form) velocity field, such an activity can often be extremely useful.

Consider the case of a linear velocity field. Such a velocity field may be obtained in electrokinetic experiments by controlling the electric field [85]. Also a velocity field can be piecewise linear. In such cases, we need not actually estimate the velocity field for all points

within the set spatial limits, but only estimate two parameters based on two or more than two particle streaks. So we do not need uniform seeding of tracers and a small collection of clear distinct streaks is sufficient. The method of estimation of the local gradient parameter is the same as described in Chapter 3.

Consider another case where we would like to estimate the spatial variation of velocity in a simple hydrodynamic (Poiseuille) flow. For a radial cross-section in a circular channel of radius a we know that under a no-slip condition at the walls, the velocity in cylindrical coordinates [60] is given by

$$V_x(r, \phi) = \frac{\Delta p}{4\eta L}(a^2 - r^2) \quad (9.1)$$

or for the case of rectangular coordinates

$$V_x(y, z) = \frac{\Delta p}{4\eta L}(a^2 - y^2 - z^2)$$

where the fluid is moving towards the positive x -axis and the maximum value of y and z is the circular channel inner radius. At the $z = 0$ plane this becomes

$$V_x(y, z) = \frac{\Delta p}{4\eta L}(a^2 - y^2) \quad (9.2)$$

and for the vertical direction we have

$$V_y(y, z) = 0 \quad (9.3)$$

It can be immediately seen that for an exposure time T_{exp} a particle streak length at a given y -value can be expressed as

$$l_x = \frac{\Delta p T_{\text{exp}}}{4\eta L}(a^2 - y^2) \quad (9.4)$$

from which we can express the pressure drop across the channel entrance and exit as

$$\Delta p = \frac{l_x 4\eta L}{T_{\text{exp}}(a^2 - y^2)} \quad (9.5)$$

Note that everything on the RHS of the above equation is known and we can evaluate the pressure drop value in theory, from a single well defined streak. While accurate μPIV

results can be obtained, the spatial resolution of a single particle track cannot be easily reached in μPIV due to a normally larger area requirement for the interrogation region. A similar procedure can be used for Poiseuille flow through a rectangular channel for which the velocity field is given by [60]

$$V_x(y, z) = \frac{4h^2 \Delta p}{\pi^3 \eta L} \sum_{n, \text{odd}} \left[\frac{1}{n^3} \left\{ 1 - \frac{\cosh(n\pi \frac{y}{h})}{\cosh(n\pi \frac{w}{2h})} \right\} \sin(n\pi \frac{z}{h}) \right]$$

where w , h and L are the width, height and the length of the rectangular channel.

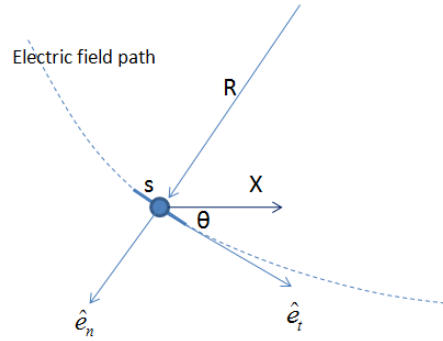


Fig. 9.1: Tangential and normal velocity components on a particle in a PDMS channel under the effects of electro-osmotic and electrophoretic fields

A similar procedure could be used to investigate the electric field in a situation where the electrokinetic velocity can be expressed as a linear function of the electric field. For example, in the case of only the electro-osmotic force being present, a particle velocity is given by [61]

$$u_{eof} = - \left(\frac{\varepsilon \zeta E}{\mu} \right)$$

Here, the streak length would be directly proportional to the RHS of the equation and can be used either to determine the electric field or the other fluid parameters (ε and μ) or the zeta potential of the microchannel wall.

9.2 ESTIMATION OF CENTERLINE VELOCITY FIELD IN VARIABLE GEOMETRY CHANNELS

The performance of the proposed micro particle streak velocimetry is discussed for two cases of centerline velocity field estimation for channels etched on Polydimethylsiloxane

(PDMS). Spatially sampled Eulerian velocities for the two PDMS channels are obtained as below.

Particle motion in a PDMS channel when electro-osmotic and electrophoretic are both present is given as

$$E(\mu_{EO} + \mu_{EM} - \mu_{DEP} \frac{\partial E}{\partial s}) \hat{e}_t + \frac{\mu_{DEP} E^2}{R} \hat{e}_n \quad (9.6)$$

The above equation is described in [86] and assumes that particle inertial effect is negligible. Here \hat{e}_n and \hat{e}_t are the normal and tangential components of the velocity at a point in the channel, E is the electric field, R is the radius of curvature of the field, s is the arc length along the electric field line and the μ variables are constants from the electro-osmotic and electrophoretic fields. The centerline velocity field along x -axis is obtained from the x -components of the tangential and normal fields as shown in Fig. 9.1

The net x -axis component of the particle velocity is then given by

$$V_p(\theta) = E(\mu_{EO} + \mu_{EM} - \mu_{DEP} \frac{\partial E}{\partial s}) \cos(\theta) - \frac{\mu_{DEP} E^2}{R} \sin(\theta) \quad (9.7)$$

where θ is the angle between the tangent on the electric field line and the x -axis. On the center line $s \rightarrow x$ and $\theta \rightarrow 0$, so the centerline Eulerian field is given by

$$V_E(x) = E(\mu_{EO} + \mu_{EM} - \mu_{DEP} \frac{\partial E}{\partial x}) \quad (9.8)$$

For the two different PDMS channels the changing channel width causes the centerline electric field and consequently the velocity field, to vary. In the channel where the width decreases linearly (linear-taper) with distance from particle source reservoir can be shown to be given given by

$$V(x) = \frac{K_1}{B-x} + \frac{K_2}{(B-x)^3} \quad (9.9)$$

and for the other channel where the width tapers inversely with distance (inverse-taper), the x -component of the electric fields can be shown to be given by [85]

$$E(x) = K_3 x + K_4 \quad (9.10)$$

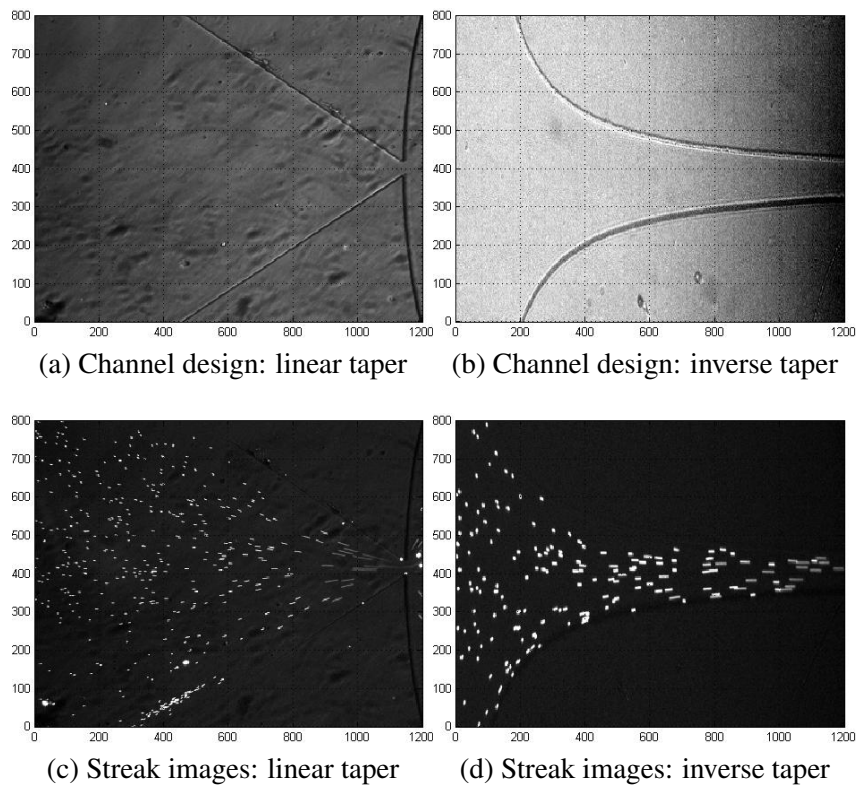


Fig. 9.2: The two different PDMS channels used for an electro-kinetic experiment where μPSV is used for velocity estimation

The constants K_i are experimental parameters, some of which are known. The two channels are shown in Fig. 9.2.

The microfluidic channels (depth 10 microns) were fabricated via standard soft lithography using PDMS. Plasma treatment was used to render the channels hydrophilic and a glass slide was used to cover the channel. Fluorescently-labelled polystyrene particles (1 μm , sulfated) diluted to a concentration of approximately 5×10^6 particles/mL in buffer were used as tracers. At the start of an experiment, the pressure was equilibrated to stop hydrodynamic flow and then a voltage (~ 500 V) was applied using two platinum electrodes dipped into the external reservoirs. Volume illumination from a mercury short-arc light source (OSRAM, H30 103 w/2) was used and the particles were imaged by a standard, simple and affordable combination of inverted microscope (IX70, Olympus), CCD camera

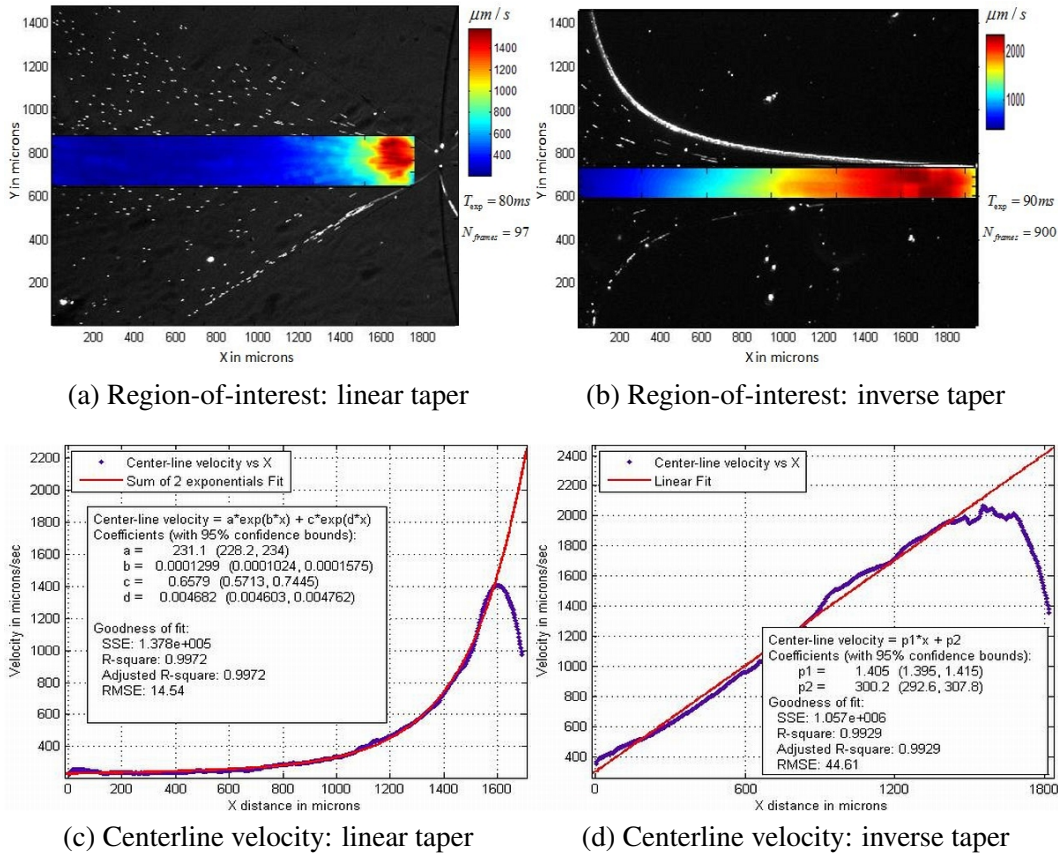


Fig. 9.3: Results for velocity estimation in PDMS channels

(Q Imaging Inc.) and Streampix III software (Norpix). The exposure time was adjusted depending on the experiment (30 ms - 90 ms). The frame rate was approximately 17 frames per second.

Fig. 9.2 also shows the particle streaks obtained for the two channels. The problem of overlapping of particle streaks was seen to be present more for the first (linear-taper) channel for the selected exposure time. The reason for this is the nature of the velocity field, which is approximately hyperbolic and thus strong velocity gradients cannot be directly avoided. Also the correct selection of the exposure time becomes a problem in such a case, as for the slower part, a small exposure time would cause loss in resolution.

The velocity field estimation procedure was conducted for a small strip along the

channel length, at the center of the channel and is shown in Fig. 9.3. along with the results. For the linear-taper channel, the 2-D variation of velocity horizontal component can be seen in Fig. 9.3 (a). The nature of the velocity field is seen to be hyperbolic as expected. Also, the peak of the velocity field is very localized (has sharp boundaries) and this is expected from the channel geometry. Lastly, at regions very close to the channel exit, the overlap of streaks causes loss of data and reduces the estimated velocity magnitude.

For the channel with inverse-taper, the velocity field is linear and this can be also observed from the spread of the horizontal component. Note that the highest velocity for the linear-taper case is less than that for the inverse-taper case, but the sudden change in velocity gradient appears to be largely responsible for the overlapping problem at the channel exit. Also, note that for the linear-taper case, the velocity field estimation was achieved with only 97 frames, a small number compared to the 900 frames used for the inverse-taper channel. This shows that a good collection of sharply defined streaks is sufficient to obtain a velocity estimate by the proposed method. However larger number of frames automatically mean a more robust estimate and better smoothing.

The data from the center-strip is used to obtain the centerline velocity estimate and this is shown in Fig. 9.3(c) and Fig. 9.3(d). During the estimation in the PDMS channels, the streak data at the extreme end is excluded for fitting purposes. This is because towards the destination, detection errors increase as the intensity decreases on the high velocity end of the streak (due to extended spread). Moreover, streaks overlap or get partly eliminated from the stack if they overlap with the effective frame boundary (e.g. when the particle is about to leave the channel). Accordingly, inclusion of this data would provide wrong estimates. The centerline velocity fields obtained are as expected in theory.

9.3 ESTIMATION OF 2-D VELOCITY FIELD AT A CAPILLARY JUNCTION

The experimental data for the 2-D velocity field estimation was obtained from a microfluidic device that comprises of two glass plates between which capillary channel ends are placed. The sides of the rectangular plates is closed with epoxy. The diameter of the capil-

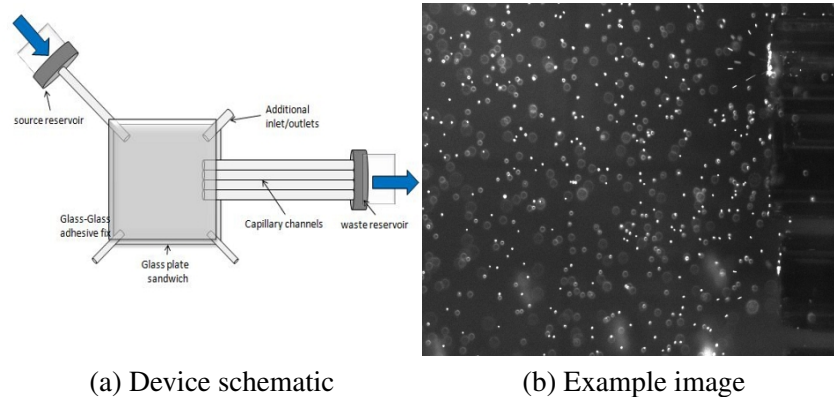


Fig. 9.4: A glass-sandwiched-capillary microfluidic device

larities is $320 \mu m$ and the diameter of the opening is μm . There are 3 additional inlets and outlets which were not used for the experiment. The main inlet connected to the reservoir and the outlet comprising of 4 capillary channels were maintained at constant pressure difference. No electric field was used for this experiment. The tracer particles, and imaging apparatus set up were same as that discussed for the PDMS channel experiments discussed earlier. The schematic of the experimental design and an example image frame is shown in Fig. 9.4.

The results of spatio-temporal averaging based velocity estimation procedure is shown in Fig. 9.5. The centerline is also shown in the 3-D surface plot for the horizontal component. Note that in the image of the horizontal component the sign of the velocity is negative owing to the direction of the flow and the imaging X-axis. It can be seen in the vertical component image that the flow is not exactly symmetric and this is expected since the inlet reservoir was not symmetrically placed with respect to the outlet reservoir. The hyperbolic nature of the flow can be clearly seen, as this was observed earlier for our simulated experimental results in Chapter 7. Also note, that the loss in streak numbers at the channel entrance (due to overlap and loss in SNR) results in the decrease of the estimated velocity before the $50 \mu m$ point from the channel entrance. This also shows why fewer streaks, more frames and good image preprocessing (or clear, distinct streaks) is important

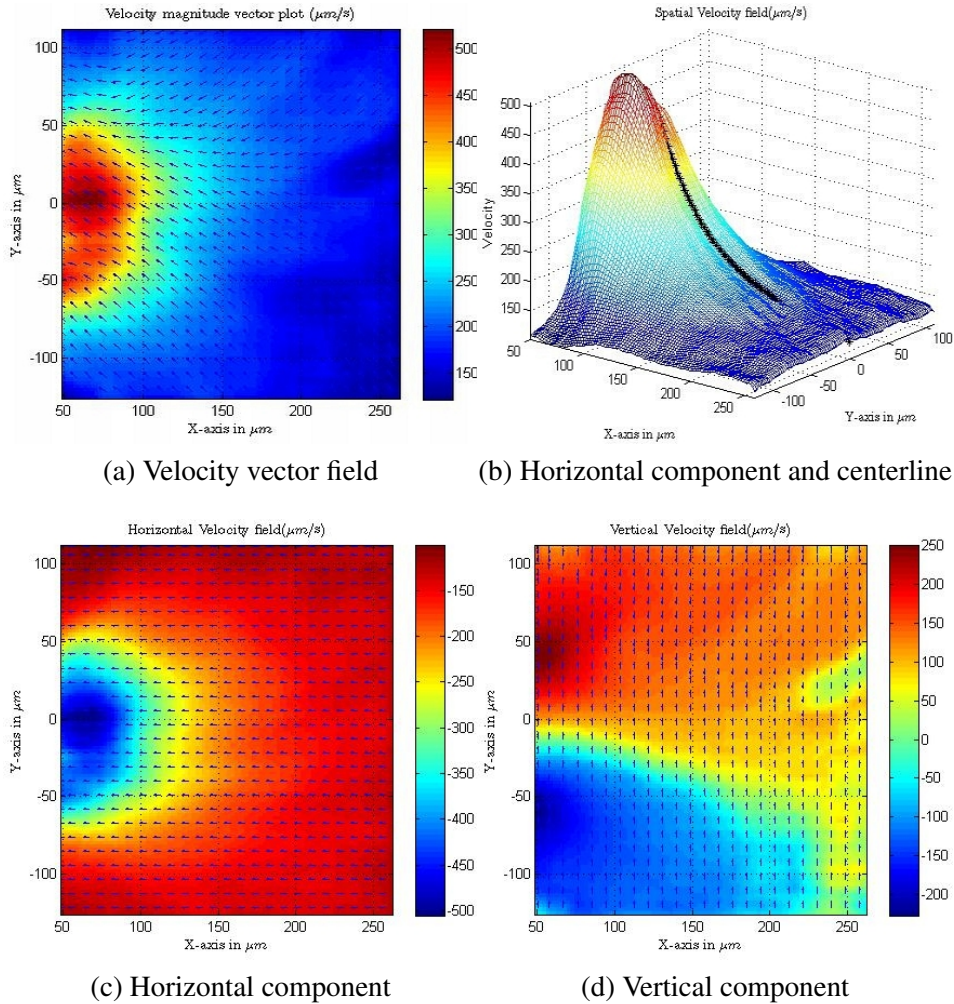


Fig. 9.5: 2-D velocity field results for a glass-sandwiched-capillary device design

for the estimation strategy.

The estimation of velocity fields in experimental microfluidic devices is quite challenging. The construction of the microfluidic device can turn out to be imperfect due to many reasons and this can severely bias and distort expected results. Corrections to device geometry based on the device performance need to be fast to reduce the total time of the experiment. Accordingly a quick velocimetry method is very useful for estimating the device performance. The results discussed above for both glass and PDMS based devices show that particle streaks can be effectively used for microfluidic velocity estimation. The

spatio-temporal statistics based methods discussed in this dissertation can be used for fast and cheap velocimetry techniques, extremely well suited for routine experiments.

Simulation techniques discussed in this dissertation can also help reduce experimentation time, allowing the researcher to spend more time in analysis. The particle flow simulation framework for arbitrary user defined velocity field can generate complete image sequence stacks, ready for analysis towards a better device and (or) quantitative algorithm design.

CHAPTER 10

FUTURE WORK

The proposed method is being further developed and improved and this dissertation attempts to build a strong foundation of ideas for future work. This holds true for both the novel simulation framework for gold standard particle flow data generation and the mathematical approach taken to use velocity smearing (streak formation) in a productive manner for micro-channel velocity estimation.

10.1 SYNTHESIS OF PDMS BASED CHANNELS AND PERFORMANCE EVALUATION

In this dissertation, a method for simulation of particle streaks from known velocity fields as well as a method for estimation of velocity fields from particle streak length observations is established. The comparison of particle streaks formed in simulation and particle streaks obtained in actual PDMS channels would help evaluate the performance of our particle track simulation method and improve on its deficiencies. Microfluidic channels and channel networks need to be developed to validate using our method, well known microfluidic principles; e.g., dependence of channel fluid resistance on channel dimension.

10.2 IMPROVEMENTS IN ESTIMATION STRATEGIES

While the first-order local velocity field approximation proved efficient for a variety of test cases, there could be multiple methods for the proper integration of the local gradient and initial velocity information. For example, smooth surfaces could be fit to regions based on the 2-D gradient information. Another procedure might be to exploit the smoothness criterion and model the local 2-D field in a transform domain. The problem of fitting of a smooth surface (velocity vector field) given local gradient values needs to be solved on a case-by-case basis; e.g., for experiments involving di-electrophoresis and experiments for only electro-osmosis can be studied as separate cases, based on the complexity of force interactions and the smoothness of the velocity field. On the other hand, an exhaustive study can be done comparing existing methods.

Better resolution (sub-pixel) could be obtained when the image of a particle spans multiple pixels by fitting a 2-D Gaussian. While for a well resolved sub-micron particle the

effect would be very small for larger velocities, this could boost the accuracy for regions with small velocities.

10.3 CHANGES IN EXPERIMENTAL STRATEGIES

The effect of using a smaller bead (sub-micron) was directly related to the resolution of the measurements. Effectively this calls for a higher numerical aperture for the microscope, and (or) smaller beads. The effects of modulating these parameters needs to be studied. Also, Brownian motion needs to be analyzed in the context of streak formation.

10.4 FUTURE WORK FOR PARTICLE FLOW SIMULATION

The mathematical modelling of streaks based on CFD velocity fields could be further enhanced by including more physics in their simulation. For example, particles could be assigned mass and volume to make the images even more realistic. Additionally, we could add interacting physical laws from theory as well as from empirical rules. The simulations could easily be extended in three dimensions and then combined for a 3-D visualization of the particle flow.

10.5 APPLICATIONS OF THE MICRO-PSV

The knowledge of local velocities could lead to the non-intrusive measurement of local pressure drops across the experimental region under analysis. Moreover, the spatial resolution that would be available would be far higher than pressure transducers can provide. The continuous particle path provided by the particle streak can prove advantageous to PIV in this context, leading to better measurement.

Particles move parallel to streamlines while forming streaks or follow field lines when moving under electrical fields. Temporally connected particle streaks can easily be used to visualize field-lines and streamlines. The knowledge of the velocity field aids this procedure.

REFERENCES

- [1] C. Meinhart, S. Wereley, and J. Santiago, "Micron-resolution velocimetry techniques," in *Laser Techniques Applied to Fluid Mechanics, Selected Papers from the Ninth International Symposium, Lisbon, Portugal, July. , 1998*, pp. 57–70.
- [2] J. Santiago, S. Wereley, C. Meinhart, D. Beebe, and R. Adrian, "A particle image velocimetry system for microfluidics," *Experiments in Fluids*, vol. 25, no. 4, pp. 316–319, 1998.
- [3] R. Lindken, M. Rossi, S. Große, and J. Westerweel, "Micro-particle image velocimetry (μ PIV): Recent developments, applications, and guidelines," *Lab on a Chip*, vol. 9, no. 17, pp. 2551–2567, 2009.
- [4] R. Adrian, "Scattering particle characteristics and their effect on pulsed laser measurements of fluid flow- speckle velocimetry vs particle image velocimetry," *Applied optics*, vol. 23, p. 1690, 1984.
- [5] C. Pickering and N. Halliwell, "Speckle photography in fluid flows- signal recovery with two-step processing," *Applied optics*, vol. 23, no. 8, pp. 1128–1129, 1984.
- [6] R. Adrian, "Particle-imaging techniques for experimental fluid mechanics," *Annual Review of Fluid Mechanics*, vol. 23, no. 1, pp. 261–304, 1991.
- [7] R. Adrian, "Twenty years of particle image velocimetry," *Experiments in Fluids*, vol. 39, no. 2, pp. 159–169, 2005.
- [8] I. Grant, "Particle image velocimetry: A review," *Proceedings of the Institution of Mechanical Engineers, Part C: Journal of Mechanical Engineering Science*, vol. 211, no. 1, pp. 55–76, 1997.
- [9] M. Raffel, C. Willert, and J. Kompenhans, *Particle image velocimetry: A practical guide*. Springer Verlag, 1998.
- [10] J. Westerweel, "Fundamentals of digital particle image velocimetry," *Measurement Science and Technology*, vol. 8, p. 1379, 1997.
- [11] S. Wereley and C. Meinhart, "Recent advances in micro-particle image velocimetry," *Annual Review of Fluid Mechanics*, vol. 42, pp. 557–576, 2010.
- [12] S. Williams, C. Park, and S. Wereley, "Advances and applications on microfluidic velocimetry techniques," *Microfluidics and Nanofluidics*, vol. 8, no. 6, pp. 709–726, 2010.
- [13] M. Olsen and R. Adrian, "Out-of-focus effects on particle image visibility and correlation in microscopic particle image velocimetry," *Experiments in Fluids*, vol. 29, pp. 166–174, 2000.

- [14] C. Bourdon, M. Olsen, and A. Gorby, "Validation of an analytical solution for depth of correlation in microscopic particle image velocimetry," *Measurement Science and Technology*, vol. 15, p. 318, 2004.
- [15] K. Sharp and R. Adrian, "On flow-blocking particle structures in microtubes," *Microfluidics and Nanofluidics*, vol. 1, no. 4, pp. 376–380, 2005.
- [16] C. Meinhart, S. Wereley, and J. Santiago, "A PIV algorithm for estimating time-averaged velocity fields," *Transactions-American Society of Mechanical Engineers Journal of Fluids Engineering*, vol. 122, no. 2, pp. 285–289, 2000.
- [17] J. Westerweel, "Theoretical analysis of the measurement precision in particle image velocimetry," *Experiments in Fluids*, vol. 29, pp. 3–12, 2000.
- [18] J. Westerweel, "On velocity gradients in PIV interrogation," *Experiments in Fluids*, vol. 44, no. 5, pp. 831–842, 2008.
- [19] P. Meunier and T. Leweke, "Analysis and treatment of errors due to high velocity gradients in particle image velocimetry," *Experiments in Fluids*, vol. 35, no. 5, pp. 408–421, 2003.
- [20] J. Nogueira, A. Lecuona, and P. Rodriguez, "Local field correction piv: on the increase of accuracy of digital PIV systems," *Experiments in Fluids*, vol. 27, no. 2, pp. 107–116, 1999.
- [21] J. Nogueira, A. Lecuona, and P. Rodriguez, "Local field correction PIV, implemented by means of simple algorithms, and multigrid versions," *Measurement Science and Technology*, vol. 12, p. 1911, 2001.
- [22] K. Takehara, R. Adrian, G. Etoh, and K. Christensen, "A Kalman tracker for super-resolution PIV," *Experiments in Fluids*, vol. 29, pp. 34–41, 2000.
- [23] S. Wereley and C. Meinhart, "Second-order accurate particle image velocimetry," *Experiments in Fluids*, vol. 31, no. 3, pp. 258–268, 2001.
- [24] D. Hart, "PIV error correction," *Experiments in Fluids*, vol. 29, no. 1, pp. 13–22, 2000.
- [25] J. Sveen and E. Cowen, "Quantitative imaging techniques and their application to wavy flows," *Advances in Coastal and Ocean Engineering*, vol. 9, p. 1, 2004.
- [26] M. Cheezum, W. Walker, and W. Guilford, "Quantitative comparison of algorithms for tracking single fluorescent particles," *Biophysical Journal*, vol. 81, no. 4, pp. 2378–2388, 2001.

- [27] B. Carter, G. Shubeita, and S. Gross, "Tracking single particles: A user-friendly quantitative evaluation," *Physical Biology*, vol. 2, p. 60, 2005.
- [28] K. Ohmi and H. Li, "Particle-tracking velocimetry with new algorithms," *Measurement Science and Technology*, vol. 11, p. 603, 2000.
- [29] N. Ouellette, H. Xu, and E. Bodenschatz, "A quantitative study of three-dimensional Lagrangian particle tracking algorithms," *Experiments in Fluids*, vol. 40, no. 2, pp. 301–313, 2006.
- [30] F. Hering, D. Wierzymok, and B. Jahne, "Particle tracking in space time sequences," in *Computer Analysis of Images and Patterns*. Springer, 1995, pp. 294–301.
- [31] F. Hering, M. Merle, D. Wierzymok, and B. Jahne, "A robust technique for tracking particles over long image sequences," in *Proc. of ISPRS Intercommission Workshop - From Pixels to Sequences, Zurich, March*. Citeseer, 1995, pp. 22–24.
- [32] M. Bown, J. MacInnes, R. Allen, and W. Zimmerman, "Three-dimensional, three-component velocity measurements using stereoscopic micro-PIV and PTV," *Measurement Science and Technology*, vol. 17, p. 2175, 2006.
- [33] A. Kumar, C. Cierpka, S. Williams, C. Kahler, and S. Wereley, "3D3C velocimetry measurements of an electrothermal microvortex using wavefront deformation PTV and a single camera," *Microfluidics and Nanofluidics*, pp. 1–11, 2010.
- [34] Y. Feng, J. Goree, and B. Liu, "Errors in particle tracking velocimetry with high-speed cameras," *Review of Scientific Instruments*, vol. 82, p. 053707, 2011.
- [35] J. Agui and J. Jimenez, "On the performance of particle tracking," *Journal of Fluid Mechanics*, vol. 185, no. 1, pp. 447–468, 1987.
- [36] M. Rosenstiel and R. Grigat, "Segmentation and classification of streaks in a large-scale particle streak tracking system," *Flow Measurement and Instrumentation*, 2009.
- [37] P. Dimotakis, F. Debussy, and M. Koochesfahani, "Particle streak velocity field measurements in a two-dimensional mixing layer," *Physics of fluids*, vol. 24, p. 995, 1981.
- [38] T. Dickey, B. Hartman, E. Hurst, and S. Isenogle, "Measurement of fluid flow using streak photography," *American Journal of Physics*, vol. 52, p. 216, 1984.
- [39] B. Khalighi and Y. Lee, "Particle tracking velocimetry: An automatic image processing algorithm," *Applied Optics*, vol. 28, no. 20, pp. 4328–4332, 1989.
- [40] D. Jeng, "Planar measurement of three-component velocity by streaked-particle-imaging velocimetry," *Applied Optics*, vol. 34, pp. 2301–2304, 1995.

- [41] D. Altman, “Statistics of optimal particle streak photography,” *Physics of Fluids A: Fluid Dynamics*, vol. 3, p. 2132, 1991.
- [42] J. Brody, P. Yager, R. Goldstein, and R. Austin, “Biotechnology at low Reynolds numbers,” *Biophysical Journal*, vol. 71, no. 6, pp. 3430–3441, 1996.
- [43] S. Chao, M. Holl, J. Koschwanetz, R. Carlson, L. Jang, and D. Meldrum, “Velocity measurement in microchannels with a laser confocal microscope and particle linear image velocimetry,” *Microfluidics and Nanofluidics*, vol. 1, no. 2, pp. 155–160, 2005.
- [44] H. Davies, D. Chapman, T. Vine, and W. Proud, “Development of an optical system for high-speed, small-scale velocity measurements,” *Bulletin of the American Physical Society*, vol. 54, 2009.
- [45] L. Zhao, Y. Zhang, X. Wang, G. Riskowski, and L. Christianson, “Development of PIV techniques to measure airflow patterns in ventilated airspaces.” in *ASHRAE Annual Meeting, Seattle, WA (US), 06/18/1999–06/23/1999*, 1999.
- [46] N. Tani, H. Kondo, M. Mori, K. Hishida, and M. Maeda, “Development of fiberscope PIV system by controlling diode laser illumination,” *Experiments in Fluids*, vol. 33, no. 6, pp. 752–758, 2002.
- [47] D. Muller, B. Muller, and U. Renz, “Three-dimensional particle-streak tracking (PST) velocity measurements of a heat exchanger inlet flow: A new method to measure all three air-flow velocity components in a plane is applied to a steady-state three-dimensional flow,” *Experiments in Fluids*, vol. 30, no. 6, pp. 645–656, 2001.
- [48] F. Kato and I. Shimizu, “Optical processing of particle tracking velocimetry under deformed double exposure,” *Measurement Science and Technology*, vol. 11, p. 646, 2000.
- [49] J. Bergthorson, D. Goodwin, and P. Dimotakis, “Experiments and modeling of impinging jets and premixed stagnation flames,” in *Proceedings of the Fifteenth Australasian Fluid Mechanics Conference*, 2004.
- [50] J. Bergthorson, D. Goodwin, and P. Dimotakis, “Particle streak velocimetry and CH laser-induced fluorescence diagnostics in strained, premixed, methane-air flames,” *Proceedings of the Combustion Institute*, vol. 30, no. 1, pp. 1637–1644, 2005.
- [51] J. Bergthorson and P. Dimotakis, “Particle velocimetry in high-gradient/high-curvature flows,” *Experiments in Fluids*, vol. 41, no. 2, pp. 255–263, 2006.
- [52] F. Hering, C. Leue, D. Wierzimok, and B. Jahne, “Particle tracking velocimetry beneath water waves. Part I: Visualization and tracking algorithms,” *Experiments in Fluids*, vol. 23, no. 6, pp. 472–482, 1997.

- [53] J. Price, “Lagrangian and eulerian representations of fluid flow: Kinematics and the equations of motion.”
- [54] J. Helman and L. Hesselink, “Representation and display of vector field topology in fluid flow data sets,” *Computer*, vol. 22, no. 8, pp. 27–36, 1989.
- [55] T. Weinkauff and H. Theisel, “Streak lines as tangent curves of a derived vector field,” *IEEE Transactions on Visualization and Computer Graphics*, vol. 16, no. 6, pp. 1225–1234, 2010.
- [56] T. Squires and S. Quake, “Microfluidics: Fluid physics at the nanoliter scale,” *Reviews of Modern Physics*, vol. 77, no. 3, p. 977, 2005.
- [57] J. Berthier and P. Silberzan, *Microfluidics for Biotechnology*. Artech House Publishers, 2009.
- [58] E. Lauga, M. Brenner, and H. Stone, “Microfluidics: The no-slip boundary condition,” *Arxiv preprint cond-mat/0501557*, 2005.
- [59] M. Schindler, P. Talkner, and P. Hanggi, “Computing stationary free-surface shapes in microfluidics,” *Physics of Fluids*, vol. 18, p. 103303, 2006.
- [60] H. Bruus, *Theoretical Microfluidics*. Oxford University Press, USA, 2008, vol. 18.
- [61] S. Devasenathipathy, J. Santiago, and K. Takehara, “Particle tracking techniques for electrokinetic microchannel flows,” *Anal. Chem*, vol. 74, no. 15, pp. 3704–3713, 2002.
- [62] B. Jahne, *Digital Image Processing: Concepts, Algorithms, and Scientific Applications*. Springer-Verlag New York, Inc., 1993.
- [63] K. Nordberg and G. Farneback, “A framework for estimation of orientation and velocity,” in *Proceedings of the International Conference on Image Processing*, vol. 3. IEEE, 2003, pp. III–57.
- [64] S. Deans, *The Radon Transform and Some of Its Applications*. Wiley New York:, 1983.
- [65] A. Poularikas, *Transforms and Applications Handbook*. CRC, 2009, vol. 43.
- [66] R. Gonzalez and R. Woods, “Digital image processing,” 2002.
- [67] J. Parker, K. Terzidis, and I. Books, *Algorithms for image processing and computer vision*. Wiley, 1997.

- [68] N. Pal and S. Pal, "A review on image segmentation techniques," *Pattern Recognition*, vol. 26, no. 9, pp. 1277–1294, 1993.
- [69] A. Barjatya, "Block matching algorithms for motion estimation," *IEEE Transactions on Evolution Computation*, vol. 8, no. 3, pp. 225–239, 2004.
- [70] E. Chan and S. Panchanathan, "Review of block matching based motion estimation algorithms for video compression," in *Canadian Conference on Electrical and Computer Engineering, 1993*. IEEE, 1993, pp. 151–154.
- [71] R. Adrian, "Image shifting technique to resolve directional ambiguity in double-pulsed velocimetry," *Applied Optics*, vol. 25, no. 21, pp. 3855–3858, 1986.
- [72] I. Grant and A. Liu, "Directional ambiguity resolution in particle image velocimetry by pulse tagging," *Experiments in Fluids*, vol. 10, no. 2, pp. 71–76, 1990.
- [73] K. Okamoto, S. Nishio, T. Saga, and T. Kobayashi, "Standard images for particle-image velocimetry," *Measurement Science and Technology*, vol. 11, p. 685, 2000.
- [74] B. Lecordier and J. Westerweel, "The europiv synthetic image generator (sig)," *Particle image velocimetry: recent improvements. EUROPIV*, vol. 2, pp. 145–162, 2003.
- [75] R. Keane, R. Adrian, and Y. Zhang, "Super-resolution particle imaging velocimetry," *Measurement Science and Technology*, vol. 6, p. 754, 1995.
- [76] G. Quenot, J. Pakleza, and T. Kowalewski, "Particle image velocimetry with optical flow," *Experiments in Fluids*, vol. 25, no. 3, pp. 177–189, 1998.
- [77] J. Bell, M. Day, I. Shepherd, M. Johnson, R. Cheng, J. Grcar, V. Beckner, and M. Lijewski, "Numerical simulation of a laboratory-scale turbulent v-flame," *Proceedings of the National Academy of Sciences of the United States of America*, vol. 102, no. 29, p. 10006, 2005.
- [78] S. M. and Cameron, "PIV algorithms for open-channel turbulence research: Accuracy, resolution and limitations," *Journal of Hydro-environment Research*, 2011. [Online]. Available: <http://www.sciencedirect.com/science/article/pii/S1570644311000050>
- [79] G. Elsinga, F. Scarano, B. Wieneke, and B. Van Oudheusden, "Tomographic particle image velocimetry," *Experiments in Fluids*, vol. 41, no. 6, pp. 933–947, 2006.
- [80] N. Nguyen and R. White, "Acoustic streaming in micromachined flexural plate wave devices: Numerical simulation and experimental verification," *IEEE Transactions on Ultrasonics, Ferroelectrics and Frequency Control*, vol. 47, no. 6, pp. 1463–1471, 2000.

- [81] A. COMSOL, “Comsol multiphysics users guide,” *Version: September, 2005*.
- [82] U. Ascher and L. Petzold, *Computer methods for ordinary differential equations and differential-algebraic equations*. Society for Industrial Mathematics, 1998, vol. 61.
- [83] C. Kelley, *Solving nonlinear equations with Newton’s method*. Society for Industrial Mathematics, 2003, vol. 1.
- [84] J. Bresenham, “Algorithm for computer control of a digital plotter,” *IBM Systems journal*, vol. 4, no. 1, pp. 25–30, 1965.
- [85] N. Weiss, P. Jones, P. Mahanti, K. Chen, T. Taylor, and M. Hayes, “Dielectrophoretic mobility determination in dc insulator-based dielectrophoresis,” *Electrophoresis*.
- [86] K. Chen, J. Pacheco, M. Hayes, and S. Staton, “Insulator-based dielectrophoretic separation of small particles in a sawtooth channel,” *Electrophoresis*, vol. 30, no. 9, pp. 1441–1448, 2009.